Spring 2013

URANS And DES for Delft catamaran for static drift conditions in deep water

Timur Kent Dogan
University of Iowa

Recommended Citation

Dogan, Timur Kent. "URANS And DES for Delft catamaran for static drift conditions in deep water." MS (Master of Science) thesis, University of Iowa, 2013.
https://doi.org/10.17077/etd.ceayk0vt

URANS AND DES FOR DELFT CATAMARAN FOR STATIC DRIFT CONDITIONS IN DEEP WATER

by

Timur Kent Dogan

A thesis submitted in partial fulfillment of the
requirements for the Master of Science
degree in Mechanical Engineering
in the Graduate College of
The University of Iowa

May 2013

Thesis Supervisor: Professor Frederick Stern

Graduate College
The University of Iowa
Iowa City, Iowa

CERTIFICATE OF APPROVAL

MASTER'S THESIS

This is to certify that the Master's thesis of

Timur Kent Dogan

has been approved by the Examining Committee for the thesis requirement for the Master of Science degree in Mechanical Engineering at the May 2013 graduation.

Thesis committee: ______________________________
Frederick Stern, Thesis Supervisor

____
Ching-Long Lin

____
H.S. Udaykumar

ACKNOWLEDGEMENTS

I would like to thank my advisor, Dr. Fred Stern. His guidance and encouragement throughout my graduate career has been instrumental. I would also like to thank my other committee members, Dr. H.S. Udaykumar and Dr. Ching-Long Lin, for taking time out of their schedules to assist me in this process.

This research was sponsored by the US Office of Naval Research, grants N00014-10-1-0017 and N000140-91-09-5-4 under administration Dr. Patrick Purtell. The computations were performed at DoD Navy HPC systems.

TABLE OF CONTENTS

LIST OF TABLES iv

LIST OF FIGURES v

CHAPTER

1 INTRODUCTION 1

2 EXPERIMENTAL AND SIMULATION CONDITIONS 4

  2.1 Geometry 4
  2.2 Experimental Data and Conditions 4
  2.3 Simulation Conditions 5

3 COMPUTATIONAL METHOD 10

  3.1 Overview 10
  3.2 Governing Equations 10
  3.3 Turbulence Modeling 11
  3.4 Analysis Methods 15

4 URANS RESULTS USING GR GRID 17

  4.1 Validation of Integral Variables 17
  4.2 Integral Variable Patterns, Vortical Structures and Wave Patterns 18

5 URANS AND DES RESULTS USING G2,G3,G4, AND G5 GRIDS . 72

  5.1 Verification of Integral Variables 72
  5.2 Validation of Integral and Local Variables 73
  5.3 Onset and Vortex Progression Analysis 74

6 CONCLUSIONS 128

REFERENCES 129

LIST OF TABLES

Table

2.1 The main particlulars of Delft catamran 6

2.2 Simulation matrix 6

2.3 Dimensions of the grids 9

4.1 CFD error for X, σ, τ at $\beta = 0^0$ using GR 28

4.2 CFD error for X,Y, N, σ, and τ at $\beta \geq 0^0$ using GR 29

5.1 Verification study at even keel, $\beta = 6^0$ and $Fr = 0.5$ using DES 85

5.2 Verification study at $\beta = 24^0$ and $Fr = 0.3$ using URANS 85

5.3 Error comparison for URANS and DES at $\beta = 24^0$ and $Fr = 0.3$ 86

5.4 Mean of local velocity error 94

LIST OF FIGURES

Figure

2.1 Geometry and coordinate system for the Delft catamaran 6

2.2 Boundary conditions and grid design for GR 7

2.3 Boundary conditions and grid design for G5 8

4.1 Time history for $Fr = 0.3$ and $0 \leq \beta \leq 30$ using GR 20

4.2 FFT for $Fr = 0.3$ and $0 \leq \beta \leq 30$ using GR 21

4.3 Time history for $Fr = 0.45$ and $0 \leq \beta \leq 30$ using GR 22

4.4 FFT for $Fr = 0.45$ and $0 \leq \beta \leq 30$ using GR 23

4.5 Time history for $Fr = 0.61$ and $0 \leq \beta \leq 30$ using GR 24

4.6 FFT for $Fr = 0.61$ and $0 \leq \beta \leq 30$ using GR 25

4.7 Time history for $Fr = 0.77$ and $0 \leq \beta \leq 30$ using GR 26

4.8 FFT for $Fr = 0.77$ and $0 \leq \beta \leq 30$ using GR 27

4.9 EFD-CFD comparison of X, σ, τ at $\beta = 0^0$ using GR 30

4.10 Comparison of X,Y, N, σ, and τ for EFD at $0.15 \leq Fr \leq 0.4$ and CFD at $Fr = 0.3$ with $0^0 \leq \beta \leq 30^0$ using GR 31

4.11 Comparison of X,Y, N, σ, and τ for EFD at $0.37 \leq Fr \leq 0.475$ and CFD at $Fr = 0.45$ with $0^0 \leq \beta \leq 30^0$ using GR 32

4.12 Comparison of X,Y, N, σ, and τ for EFD at $0.59 \leq Fr \leq 0.65$ and CFD at $Fr = 0.61$ with $0^0 \leq \beta \leq 30^0$ using GR 33

4.13 Comparison of X,Y, N, σ, and τ for EFD at $0.65 \leq Fr \leq 0.7$ and CFD at $Fr = 0.77$ with $0^0 \leq \beta \leq 30^0$ using GR 34

4.14 Comparison of X,Y, and N for EFD at $0.15 \leq Fr \leq 0.3$ and CFD at $Fr = 0.3$ with $0^0 \leq \beta \leq 30^0$ using GR on demihull 35

4.15 Comparison of X,Y, and N for EFD at $0.37 \leq Fr \leq 0.44$ and CFD at $Fr = 0.45$ with $0^0 \leq \beta \leq 30^0$ using GR on demihull 36

4.16 Comparison of X,Y, and N for EFD at $Fr = 0.6$ and CFD at $Fr = 0.61$ with $0^0 \leq \beta \leq 30^0$ using GR on demihull 37

4.17 Comparison of total, pressure and frictional components of the integral variables using GR for CFD results at $0.3 \leq Fr \leq 0.77$ and $0^0 \leq \beta \leq 30^0$ 38

4.18 Wave patterns at $Fr = 0.3$ and $0^0 \leq \beta \leq 30^0$ using GR 39

4.19 Wave patterns at $Fr = 0.45$ and $0^0 \leq \beta \leq 30^0$ using GR 40

4.20 Wave patterns at $Fr = 0.61$ and $0^0 \leq \beta \leq 30^0$ using GR 41

4.21 Wave patterns at $Fr = 0.77$ and $0^0 \leq \beta \leq 30^0$ using GR 42

4.22 Vortex structures and boundary layer at $Fr = 0.3$ and $0^0 \leq \beta \leq 30^0$ using GR 43

4.23 Vortex structures and boundary layer at $Fr = 0.45$ and $0^0 \leq \beta \leq 30^0$ using GR 44

4.24 Vortex structures and boundary layer at $Fr = 0.61$ and $0^0 \leq \beta \leq 30^0$ using GR 45

4.25 Vortex structures and boundary layer at $Fr = 0.77$ and $0^0 \leq \beta \leq 30^0$ using GR 46

4.26 Vorticity plot at $Fr = 0.3$ and $0^0 \leq \beta \leq 30^0$ using GR 47

4.27 Vorticity plot at $Fr = 0.45$ and $0^0 \leq \beta \leq 30^0$ using GR 48

4.28 Vorticity plot at $Fr = 0.61$ and $0^0 \leq \beta \leq 30^0$ using GR 49

4.29 Vorticity plot at $Fr = 0.77$ and $0^0 \leq \beta \leq 30^0$ using GR 50

4.30 Comparison of vortex core trajectories at $0 \leq Frle0.77$ and $0^0 \leq \beta \leq 30^0$ using GR 51

4.31 Q plots at $Fr = 0.3$ and $\beta = 6^0$ for GR 52

4.32 Q plots at $Fr = 0.3$ and $\beta = 10^0$ for GR 53
4.33 Q plots at $Fr = 0.3$ and $\beta = 15^0$ for GR 54
4.34 Q plots at $Fr = 0.3$ and $\beta = 20^0$ for GR 55
4.35 Q plots at $Fr = 0.3$ and $\beta = 30^0$ for GR 56
4.36 Q plots at $Fr = 0.45$ and $\beta = 6^0$ for GR 57
4.37 Q plots at $Fr = 0.45$ and $\beta = 10^0$ for GR 58
4.38 Q plots at $Fr = 0.45$ and $\beta = 15^0$ for GR 59
4.39 Q plots at $Fr = 0.45$ and $\beta = 20^0$ for GR 60
4.40 Q plots at $Fr = 0.45$ and $\beta = 30^0$ for GR 61
4.41 Q plots at $Fr = 0.61$ and $\beta = 6^0$ for GR 62
4.42 Q plots at $Fr = 0.61$ and $\beta = 10^0$ for GR 63
4.43 Q plots at $Fr = 0.61$ and $\beta = 15^0$ for GR 64
4.44 Q plots at $Fr = 0.61$ and $\beta = 20^0$ for GR 65
4.45 Q plots at $Fr = 0.61$ and $\beta = 30^0$ for GR 66
4.46 Q plots at $Fr = 0.77$ and $\beta = 6^0$ for GR 67
4.47 Q plots at $Fr = 0.77$ and $\beta = 10^0$ for GR 68
4.48 Q plots at $Fr = 0.77$ and $\beta = 15^0$ for GR 69
4.49 Q plots at $Fr = 0.77$ and $\beta = 20^0$ for GR 70
4.50 Q plots at $Fr = 0.77$ and $\beta = 30^0$ for GR 71
5.1 Q plot and LES activation (indicated by pink outline) at $\beta = 6^0$ and $Fr = 0.5$ for G3 at even keel condition 75
5.2 Q plot and LES activation (indicated by pink outline) at $\beta = 6^0$ and $Fr = 0.5$ for G4 at even keel condition 76

5.3 Q plot and LES activation (indicated by pink outline) at $\beta = 6^0$ and $Fr = 0.5$ for G5 at even keel condition 77

5.4 Percentage of resolved turbulence in the LES activated Region at $\beta = 24^0$, and $Fr = 0.3$ 78

5.5 Time history for $Fr = 0.4, 0.5$ and $\beta = 6^0, 9^0$ fixed at dynamic sink and trim using G3 79

5.6 FFT for $Fr = 0.4, 0.5$ and $\beta = 6^0, 9^0$ fixed at dynamic sink and trim using G3 80

5.7 Time history for 0.5 and $\beta = 6^0$ fixed at even keel condition using G2-G5 81

5.8 FFT for 0.5 and $\beta = 6^0$ fixed at even keel condition using G2-G5 82

5.9 Time history for $Fr = 0.3$ and $\beta = 24^0$ using G3 83

5.10 FFT for $Fr = 0.3$ and $\beta = 24^0$ using G3 84

5.11 Comparison of vortical structures between URANS and DES $\beta = 24^0$, and $Fr = 0.3$ 87

5.12 EFD-CFD comparison at $Fr = 0.4$ and $\beta = 6^0$ for u-velocity 88

5.13 EFD-CFD comparison at $Fr = 0.4$ and $\beta = 6^0$ for vorticity 89

5.14 EFD-CFD comparison at $Fr = 0.5$ and $\beta = 6^0$ for u velocity 90

5.15 EFD-CFD comparison at $Fr = 0.5$ and $\beta = 6^0$ for vorticity 90

5.16 EFD-CFD comparison at even keel, $Fr = 0.5$ and $\beta = 6^0$ for u velocity . 91

5.17 EFD-CFD comparison at even keel, $Fr = 0.5$ and $\beta = 6^0$ for vorticity . . 92

5.18 EFD-CFD comparison, $Fr = 0.4$ and $\beta = 9^0$ for u velocity 93

5.19 EFD-CFD comparison, $Fr = 0.4$ and $\beta = 9^0$ for vorticity 93

5.20 EFD-CFD comparison, $Fr = 0.5$ and $\beta = 9^0$ for u velocity 93

5.21 EFD-CFD comparison, $Fr = 0.5$ and $\beta = 9^0$ for vorticity 93

5.22 Comparison of wave patterns for EFD and CFD at $Fr = 0.3$ and $\beta = 24^0$ 95

5.23 CFD TKE at $Fr = 0.4$ and $\beta = 6^0$ 96

5.24 CFD TKE at $Fr = 0.5$ and $\beta = 6^0$ 97

5.25 CFD TKE at even keel, $Fr = 0.5$ and $\beta = 6^0$ 98

5.26 CFD TKE at $Fr = 0.4$ and $\beta = 9^0$ 99

5.27 CFD TKE at $Fr = 0.5$ and $\beta = 9^0$ 99

5.28 Port hull pressure contour and surface streamlines below free surface at fixed dynamic sink and trim with $\beta = 6^0$, and $Fr = 0.4$ 100

5.29 Starboard hull pressure contour and surface streamlines below free surface at fixed dynamic sink and trim with $\beta = 6^0$, and $Fr = 0.4$ 101

5.30 Vortex structure for CFD fixed at dynamic sink and trim with $\beta = 6^0$, and $Fr = 0.4$ 102

5.31 Port hull pressure contour and surface streamlines below free surface at fixed dynamic sink and trim with $\beta = 6^0$, and $Fr = 0.5$ 103

5.32 Starboard hull pressure contour and surface streamlines below free surface at fixed dynamic sink and trim with $\beta = 6^0$, and $Fr = 0.5$ 104

5.33 Vortex structure for CFD fixed at dynamic sink and trim with $\beta = 6^0$, and $Fr = 0.5$ 105

5.34 Port hull pressure contour and surface streamlines below free surface at even keel with $\beta = 6^0$, and $Fr = 0.5$ 106

5.35 Starboard hull pressure contour and surface streamlines below free surface at even keel with $\beta = 6^0$, and $Fr = 0.5$ 107

5.36 Vortex structure for CFD fixed at even keel with $\beta = 6^0$, and $Fr = 0.5$. 108

5.37 Port hull pressure contour and streamlines below free surface at $Fr = 0.4$ and $\beta = 9^0$ 109

5.38 Starboard hull pressure contour and streamlines below free surface at $Fr = 0.4$ and $\beta = 9^0$ 110

5.39 Vortex structure for CFD fixed at dynamic sink and trim with $\beta = 9^0$, and $Fr = 0.4$ 111

5.40 Port hull pressure contour and streamlines below free surface at $Fr = 0.5$ and $\beta = 9^0$ 112

5.41 Starboard hull pressure contour and streamlines below free surface at $Fr = 0.5$ and $\beta = 9^0$ 113

5.42 Vortex structure for CFD fixed at dynamic sink and trim with $\beta = 9^0$, and $Fr = 0.5$ 114

5.43 Pressure contour, streamlines and $Q = 100$ line (pink colored) at $x/L = 0.005, 0.01, 0.03$ for $Fr = 0.5$, $\beta = 9^0$ (right starboard hull and left port hull) 115

5.44 Pressure contour, streamlines and $Q = 100$ line (pink colored) at $x/L = 0.05, 0.1, 0.2, 0.3$ for $Fr = 0.5$, $\beta = 9^0$ (right starboard hull and left port hull) 116

5.45 Port hull streamlines, $Q = 100$ isosurface, and x-plane streamlines at $Fr = 0.5$, $\beta = 9^0$ 117

5.46 Starboard hull streamlines, $Q = 100$ isosurface, and x-plane streamlines at $Fr = 0.5$, $\beta = 9^0$ 118

5.47 Port hull pressure contour and streamlines below free surface at $Fr = 0.3$ and $\beta = 24^0$ 119

5.48 Starboard hull pressure contour and streamlines below free surface at $Fr = 0.3$ and $\beta = 24^0$ 120

5.49 Vortical structures for CFD using DES at $\beta = 24^0$, and $Fr = 0.3$ 121

5.50 Pressure contour, streamlines and $Q = 100$ line (pink colored) at $x/L = 0.005, 0.01, 0.03$ for $Fr = 0.3$, $\beta = 24^0$ (right starboard hull and left port hull) 122

5.51 Pressure contour, streamlines and $Q = 100$ line (pink colored) at $x/L = 0.05, 0.01, 0.2$ for $Fr = 0.3$, $\beta = 24^0$ (right starboard hull and left port hull) 123

5.52 Pressure contour, streamlines and $Q = 100$ line (pink colored) at $x/L = 0.3, 0.4, 0.5$ for $Fr = 0.3$, $\beta = 24^0$ (right starboard hull and left port hull) 124

5.53 Pressure contour, streamlines and $Q = 100$ line (pink colored) at $x/L = 0.6, 0.7, 0.8$ for $Fr = 0.3$, $\beta = 24^0$ (right starboard hull and left port hull) 125

5.54 Pressure contour, streamlines and $Q = 100$ line (pink colored) at $x/L = 0.9, 1.0, 1.1$ for $Fr = 0.3$, $\beta = 24^0$ (right starboard hull and left port hull) 126

5.55 Pressure contour, streamlines and $Q = 100$ line (pink colored) at $x/L = 1.2, 1.3, 1.4$ for $Fr = 0.3$, $\beta = 24^0$ (right starboard hull and left port hull) 127

CHAPTER 1
INTRODUCTION

The demand for high-speed catamarans has strongly increased during the last decades due to its excellent performance with respect to speed, safety, resistance and transversal stability. As a consequence, a large number of theoretical, experimental and numerical studies were carried out on the Delft-372 catamaran model in recent years. Zlatev and colleagues [1] and Milanov and colleagues [2] studied the maneuvering characteristics and stability at zero course angle and small drift angles ($\beta \leq 10^0$) for both deep and shallow water by means of combined experimental fluid dynamics (EFD) and computational fluid dynamics (CFD) approaches. In general, they have achieved agreement between EFD and CFD results within the experimental accuracy margins. Castiglione and colleagues [3] and Broglia and colleagues [4] analyzed the seakeeping characteristics using the CFD and EFD approach respectively. The interference in calm water was analyzed by He and colleagues [5]. More recently, stereo particle image velocimetry (SPIV) experiments have been conducted by Broglia and colleagues [6] to study the dynamics of the keel vortices generated along the demihulls at static drift with $\beta \leq 9^0$.

Understanding of three-dimensional separation around ships on straight course or under maneuvering is important for developing next generation ships with improved performance in extreme maneuvers. The separation causes vortex-dominated flows in which the vortex breakdowns at sufficiently high drift angles. The accuracy of Detached Eddy simulation (DES) predictions have typically been far superior to that of the steady or unsteady Reynolds-Averaged Navier-Stokes (URANS) method, while avoiding the computational cost of the Large-Eddy Simulation. Thus, recent DES studies have been conducted for large steady drift cases using URANS/DES solver CFDShip-Iowa research code. Recently, Bhushan and colleagues [7] conducted DES for the surface combatant model DTMB 5415 at straight-ahead and 20^0 static drift angle (β). The straight-ahead condition provided a plausible description of the vortical structures and mean flow patterns observed in the experiments. However, the vortex strengths were overpredicted and the turbulence was not resolved. DES for DTMB 5415 at $\beta = 20^0$ significantly improved the forces and moment predictions compared to the coarse grid URANS due to improved resolved turbulence predictions. Grid verification study at $\beta = 20^0$ showed mostly converged solutions for the forces with relatively small grid uncertainties. However, divergence was obtained for the moment due to small grid changes with relatively large iterative errors. Additionally, DES was conducted for a KVLCC2 tanker by Xing and colleagues [8] at a large drift angle ($\beta = 30^0$). This study analyzed the vortical structures, instabilities, and turbulent structures. Although this study certified the good accuracy of numerical simulation, validation could not be achieved due to the lack of experimental results.

The objective of this study is to identify and analyze the vortical structures, turbulent structures and instabilities of the Delft-372 catamaran and validate URANS and DES solver CFDShip-Iowa V4.5 in collaboration with NATO AVT 183 (Reliable Prediction of Separated Flow Onset and Progression for Air and Sea Vehicles). Unlike single hull ship models DTMB and KVCC2, prediction of local flow components, wave patterns, and integral variables could be more difficult to predict with CFD for the Delft catamaran due to wave and vortex interactions. The URANS and DES are performed on the Delft catamaran ship hull model at wide ranges of Froude numbers and drift angels. The CFD results were compared to experimental results on Delft catamaran conducted by the Bulgarian Ship Hydrodynamics Center (BSHC), Italian Ship Model Basin (INSEAN), and TU Delft facilities. Additionally, vortical structures, instabilities and wave patterns have been studied in detail.

CHAPTER 2
EXPERIMENTAL AND SIMULATION CONDITIONS

2.1 Geometry

Delft 372 catamran model (Figure 2.1) was used for the experimental and numerical studies. Main particulars of the geometry of the catamaran is shown in Table 2.1. BSHC facility used a model with different vertical center of gravity than INSEAN and TU Delft facilities. Additionally, all three facilities had different non-dimensional depth and vertical center of gravity.

2.2 Experimental Data and Conditions

The experimental data included the integral variables, motions and wave profile at $0 \leq \beta \leq 24^0$ and $0.17 \leq Fr \leq 0.7$ from BSHC [2]; the integral variables at $\beta = 0^0$ and $0.1 \leq Fr \leq 0.8$, motions and stereo particle image velocimetry (SPIV) measurements at $\beta = 6^0, 9^0$ and $Fr = 0.4, 0.5$ from INSEAN [4, 6]; and the integral variables and motions at $\beta = 0^0$ and $0.18 \leq Fr \leq 0.75$ from TU Delft [9]. The model was free to sink and trim, while the roll was fixed at zero for the integral variable, motion and wave measurements. For the SPIV measurements, the model was either fixed at dynamic sink and trim or even keels condition. The model was towed at one location, center of gravity, for INSEAN and TU Delft facilities, while it was towed at two locations from two locations for BSHC facility.

2.3 Simulation Conditions

Three sets of CFD simulations were performed: (1) hull free to sink and trim with $0.3 \leq Fr \leq 0.77$ and $0^0 \leq \beta \leq 30^0$ with URANS, (2) hull fixed at dynamic sink and trim or even keel conditions with $Fr = 0.4$, 0.5 and $\beta = 6^0, 9^0$ with DES, (3) hull free to sink and trim with $Fr = 0.3$,$\beta = 24^0$ with DES and URANS (Table 2.2). Two different grid topology was used for these simulations shown in Figures 2.2 and 2.3. The dimensions of the designed grids are shown in Table 2.3 where G1 through G5 grids have the same topology with refinement ratio of $\sqrt{2}$. Validation of integral variables were conducted for case (1) using GR. The flow field around the catamaran was analyzed, including detailed study on vortex structures and wave elevations. This information was used to design new set of grids G1-G5 for cases (2) and (3). Verification study was performed for cases (2) and (3) using DES and URANS respectively. The local mean velocity components and x-vorticity for case (2) was validated using SPIV results from INSEAN facility. Although DES was activated in the vortex regions, the turbulence was not resolved for case (2). Validation of integral variables and wave elevation was performed for case (3) and the resolved turbulence (RTKE) was 66%.

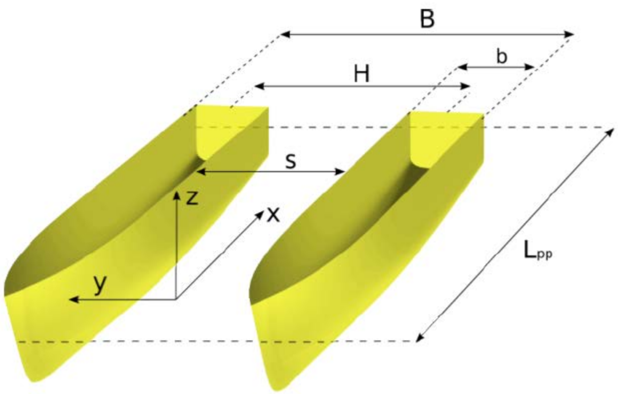

Figure 2.1: Geometry and coordinate system for the Delft catamaran

Table 2.1: The main particlulars of Delft catamran

Non-dimensional Parameters	Symbol	BSHC	INSEAN	TU Delft	CFD
Beam overall	B/L	0.31	0.31	0.31	0.31
Beam demihull	b/L	0.08	0.08	0.08	0.08
Distance between center of hulls	H/L	0.23	0.23	0.23	0.23
Draught	T/L	0.05	0.05	0.05	0.05
Longitudinal center of gravity	LCG/L	0.53	0.53	0.53	0.53
Vertical center of gravity	KG/L	0.04	0.06	0.06	0.04
Depth of towing tank	h/L	0.41	2.17	0.87	0.41
Depth to Draught Ratio	h/T	8.21	43.33	17.33	8.21

Table 2.2: Simulation matrix

Grid	β [deg]	Fr	DOF	Model	Flow	RTKE [%]
GR	0,6,10,15	0.30	Sink, Trim	RANS	Steady	-
GR	20,30	0.30	Sink, Trim	RANS	Unsteady	-
GR	0,6,10,15	0.45	Sink, Trim	RANS	Steady	-
GR	20,30	0.45	Sink, Trim	RANS	Unsteady	-
GR	0,6,10	0.61	Sink, Trim	RANS	Steady	-
GR	15,20,30	0.61	Sink, Trim	RANS	Unsteady	-
GR	0,6,10	0.77	Sink, Trim	RANS	Steady	-
GR	15,20,30	0.77	Sink, Trim	RANS	Unsteady	-
G2, G3, G4, G5	6	0.5	0 (Even Keel)	DES	Steady	0
G3	6, 9	0.40, 0.50	0 (Dynamic)	DES	Steady	0
G3	24	0.3	Sink, Trim	RANS	Unsteady	-
G4, G5	24	0.3	Sink, Trim	RANS	Steady	-
G3	24	0.3	Sink, Trim	DES	Unsteady	66

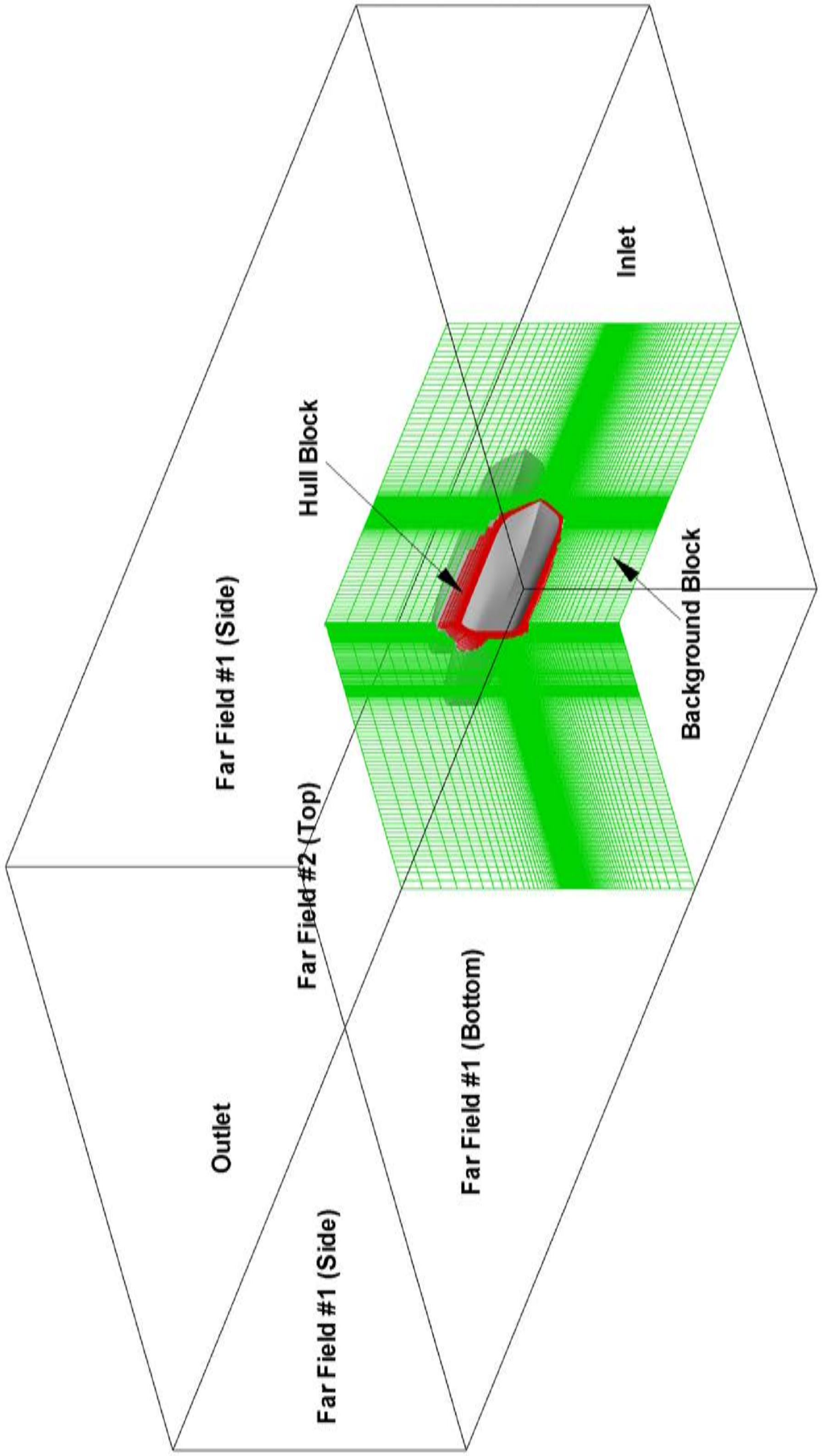

Figure 2.2: Boundary conditions and grid design for GR

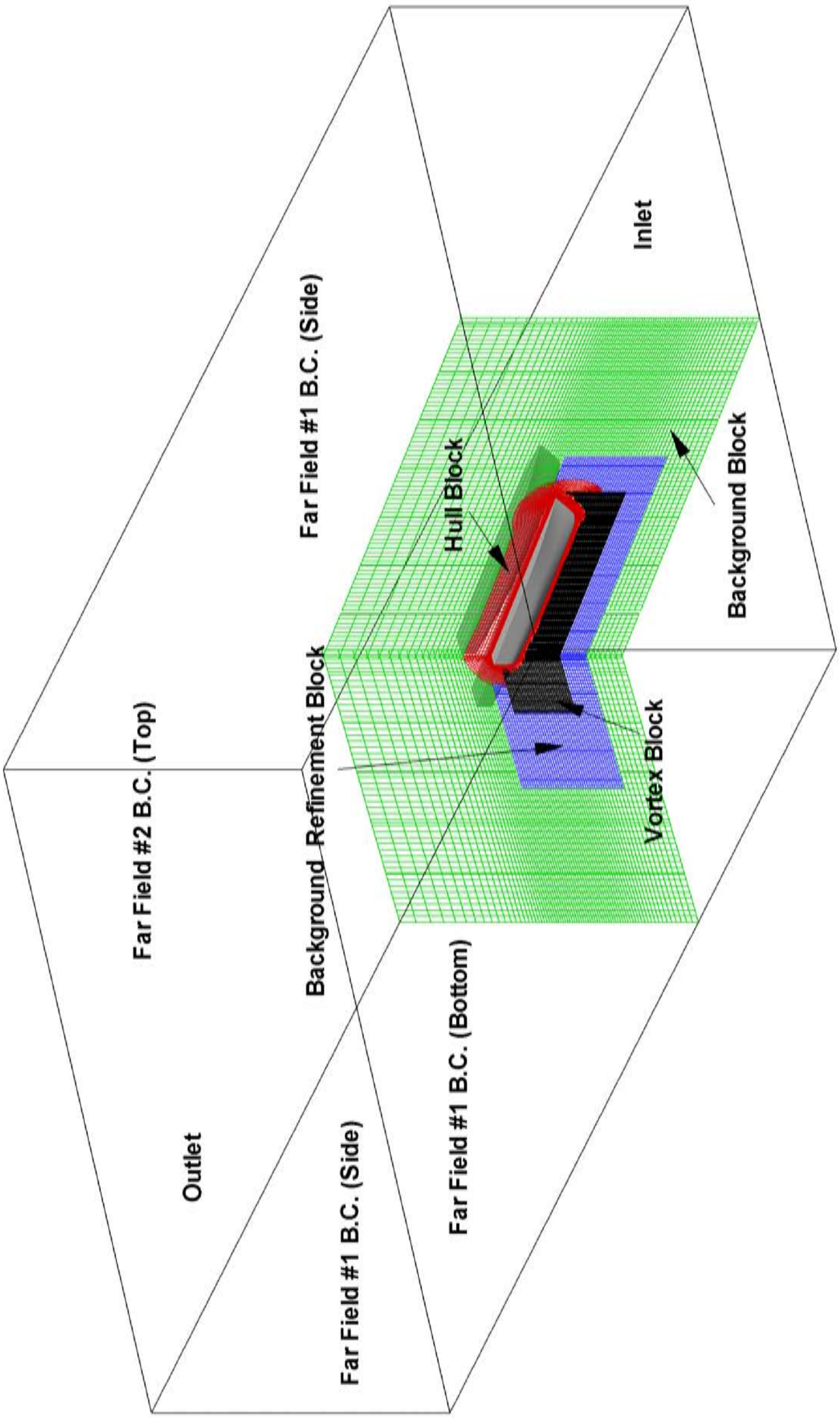

Figure 2.3: Boundary conditions and grid design for G5

Table 2.3: Dimensions of the grids

Grid	Boundary	Background	Background Ref.	Vortex Ref.	Total	y+
GR	278x260x91	329x227x88	-	-	13,149,584	0.30
G5	94x41x55	200x100x75	250x100x50	450x120x35	5,469,926	0.66
G4	133x57x77	283x141x106	354x141x71	636x170x49	15,471,287	0.45
G3	188x81x109	400x200x150	500x200x100	900x240x70	58,879,408	0.30
G2	266x115x154	566x283x212	707x283x141	1273x339x99	123,770,297	0.21
G1	376x162x218	800x400x300	1000x400x200	1800x480x140	350,075,264	0.15

CHAPTER 3
COMPUTATIONAL METHOD

3.1 Overview

The CFD simulations were conducted with URANS/DES solver CFDShip-Iowa V4.5 [10, 11] which uses dynamic overset grids, single-phase level set free surface capturing approach, blended $k - \epsilon/k - \omega$ turbulence modeling, and six degrees of freedom motions predictor. The URANS and DES approaches are based on a blended shear stress transport (SST) turbulence model.

3.2 Governing Equations

The Navier-Stokes equations are non-dimensionalized using the free stream velocity, U_0, water viscosity, v, and ship length, L. The non-dimensional mass and momentum conservation equations are:

$$\frac{\partial U_j}{\partial x_i} = 0 \tag{3.1}$$

$$\frac{\partial U_i}{\partial t} + U_j \frac{\partial U_i}{\partial x_j} = -\frac{\partial \hat{p}}{\partial x_i} + \frac{1}{Re} \frac{\partial^2 U_i}{\partial x_i \partial x_j} - \frac{\partial}{\partial x_j} \overline{u_i u_j} \tag{3.2}$$

where U_i are Reynolds-averaged velocity components, $x_i = (x, y, z)$ are the independent coordinate directions $\hat{p} = \left(\frac{p - p_\infty}{\rho U_0^2} + \frac{z}{Fr^2} \right)$ is the piezometric pressure coefficient, $\overline{u_i u_j}$ are the Reynolds stresses, $Fr = U_0/\sqrt{gL}$ is the Froude number, and $Re = U_0 L/v$.

3.3 Turbulence Modeling

The ARS model [12] used is the modified version of Menter's blended $k-\omega/k-\epsilon$ [13]. Reynolds stresses are:

$$\overline{u_i u_j} = -\upsilon_T \left(\frac{\partial U_i}{\partial x_j} + \frac{\partial U_j}{\partial x_i} \right) + \frac{2}{3} k \delta_{ij} + a_{ij}^{ex} k \tag{3.3}$$

where δ_{ij} is the Kronecker delta, k is the turbulent kinetic energy, $a_{ij}^{ex} k$ is the additional source term to account for the anisotropic turbulence. The anisotropic tensor:

$$\begin{aligned} a_{ij}^{ex} k = {} & \beta_3(\Omega_{ik}\Omega_{kj} - \frac{1}{3} II_\Omega \delta_{ij}) + \beta_4(S_{ik}\Omega_{kj} - \Omega_{ik}S_{kj}) \\ & + \beta_6(S_{ik}\Omega_{kl}\Omega_{lj} - \Omega_{kl}\Omega_{ik}S_{lj} - II_\Omega S_{ij} - \frac{2}{3} IV \delta_{ij}) \\ & + \beta_9(\Omega_{ik}S_{kl}\Omega_{lm}\Omega_{mj} - \Omega_{ik}\Omega_{kl}S_{lm}\Omega_{mj}) \end{aligned} \tag{3.4}$$

The non-dimensional strain rate S_{ij} tensor and corresponding invariants are:

$$S_{ij} = \frac{1}{2} \tau \left(\frac{\partial U_i}{\partial x_j} + \frac{\partial U_j}{\partial x_i} \right) \tag{3.5}$$

$$II_s = S_{kl}S_{lk}, \; III_s = S_{kl}S_{lm}S_{mk} \tag{3.6}$$

The non-dimensonal vorticity Ω_{ij} tensor and corresponding invariants are:

$$\Omega_{ij} = \frac{1}{2} \tau \left(\frac{\partial U_i}{\partial x_j} - \frac{\partial U_j}{\partial x_i} \right) \tag{3.7}$$

$$II_\Omega = \Omega_{kl}\Omega_{lk},\ IV_\Omega = S_{kl}\Omega_{lm}\Omega_{mk} \tag{3.8}$$

The time scale is $\tau = max(1/(\beta^*\omega); C_\tau\sqrt{v/(\beta^* k\omega)}$. The model coefficients are:

$$\beta_3 = \frac{-12IV}{NQ} \tag{3.9}$$

$$\beta_4 = \frac{2(N^2 - 2II_{Omega})}{Q} \tag{3.10}$$

$$\beta_6 = -\frac{6N}{Q} \tag{3.11}$$

$$\beta_9 = \frac{6}{Q} \tag{3.12}$$

$$Q = \frac{5}{6}(N^2 - 2II_\Omega)(2N^2 - II_\Omega) \tag{3.13}$$

$$N = \begin{cases} \dfrac{A_3^{'}}{3} + (P_1 + \sqrt{P_2})^{1/3} + sign(P_1 - \sqrt{P_2})^{1/3}|P_1 - \sqrt{P_2}|^{1/3},\ P_2 \geq 0 \\ \dfrac{A_3^{'}}{3} + 2(P_1 - \sqrt{P_2})^{1/6} cos\left[\dfrac{1}{3} arccos\left(\dfrac{P_1}{\sqrt{p_1^2 - P_2}}\right)\right]\ P_2 < 0 \end{cases} \tag{3.14}$$

$$P1 = (\frac{A_3^{'2}}{27} + \frac{9}{20}II_s - \frac{2}{3}II_\Omega)A_3^{'} \tag{3.15}$$

$$P2 = P_1^2 - \left(\frac{A_3^{'2}}{9} + \frac{9}{10}II_s + \frac{2}{3}II_\Omega\right)^3 \tag{3.16}$$

$$A_3^{'2} = \frac{9}{5} + \frac{9}{4}C_{Diff} max(1 + \beta_1^{(eq)} II_s, 0) \tag{3.17}$$

$$\beta_1^{(eq)} = -\frac{5N^{(eq)}}{6(N^{(eq)})^2 - 12II_\Omega} \tag{3.18}$$

$$N^{(eq)} = A_3 + A_4 = \frac{81}{20} \tag{3.19}$$

$$C_{Diff} = 2.2 \tag{3.20}$$

The governing equations for the eddy viscosity v_T, turbulent kinetic energy k, and the turbulent specific dissipation ω are as follows:

$$v_T = \frac{k}{\omega} \tag{3.21}$$

$$\frac{\partial k}{\partial t} + \left(U_j - \sigma_k \frac{\partial v_i}{\partial x_j}\right) \frac{\partial k}{\partial x_j} - \frac{1}{R_k}\nabla^2 k + s_k = 0 \tag{3.22}$$

$$\frac{\partial \omega}{\partial t} + \left(U_j - \sigma_\omega \frac{\partial v_i}{\partial x_j}\right) \frac{\partial w}{\partial x_j} - \frac{1}{R_\omega}\nabla^2 \omega + s_\omega = 0 \tag{3.23}$$

where the source terms, effective Reynolds numbers, and turbulence production are:

$$s_k = R_k(-G + \beta^* \omega k) \tag{3.24}$$

$$s_\omega = R_\omega \left[-\gamma \frac{\omega}{k} G + \beta \omega^2 + 2(1 - F_1)\sigma_{\omega 2} \frac{1}{w} \frac{\partial k}{\partial x_j} \frac{\partial \omega}{\partial x_j}\right] \tag{3.25}$$

$$R_k = \left(\frac{1}{1/Re + \sigma_k v_T}\right) \tag{3.26}$$

$$R_\omega = \left(\frac{1}{1/Re + \sigma_\omega v_T}\right) \tag{3.27}$$

$$G = \tau_{ij} \frac{\partial U_i}{\partial x_j} \tag{3.28}$$

$$F_1 = tanh\left[\left(min\left[max\left(\frac{\sqrt{k}}{0.09\omega\delta}; \frac{500}{Re\delta^2\omega}\right); \frac{4\sigma_{\omega 2} k}{CD_{k\omega}\delta^2}\right]\right)^4\right] \tag{3.29}$$

$$CD_{k\omega} = max\left(2\sigma_{\omega 2}\frac{1}{\omega}\frac{\partial k}{\partial x_j}\frac{\partial \omega}{\partial x_j}; 10^{-20}\right) \tag{3.30}$$

The blending function F_1 was designed to be 1 in the sublayer and logarithmic regions of boundary layers and gradually switch to zero in the wake region to take advantage of the strength of the $k-\omega$ and $k-\epsilon$.

The SST model is a user specified option that accounts for transport of the principle turbulent stresses and has shown to improve results for flows with adverse pressure gradients. The definition of eddy viscosity for SST model:

$$\upsilon_T = \frac{0.31k}{max(0.31\omega, \Omega F_2)} \tag{3.31}$$

$$F_2 = tanh\left(max\left(\frac{2\sqrt{k}}{0.09\omega y}, \frac{500\upsilon}{y^2\omega}\right)^2\right) \tag{3.32}$$

The ARS model was extended to the DES model. The k-transport equation was modified [14]:

$$D^k_{RANS} = \rho\beta^8 k\omega = \rho k^{3/2}/l_{k-\omega} \tag{3.33}$$

$$D^k_{DES} = k^{1/2}/(\beta^* \omega) \tag{3.34}$$

The length scales are:

$$l_{k-\omega} = k^{1/2}/(\beta^* \omega) \tag{3.35}$$

$$\bar{l} = min(l_{k-\omega}, C_{DES}\Delta) \tag{3.36}$$

where $C_{DES} = 0.65$ and Δ is the local grid spacing. $\bar{l} > 1$ is the LES zone and $\bar{l} \leq 1$ is the URANS zone.

3.4 Analysis Methods

The Q-criterion was used to identify the vortical structures. The Q-criterion is based on the second invariant of velocity gradient tensor ∇u.

$$Q = \frac{1}{2}[||\mathbf{\Omega}||^2 - ||\mathbf{S}||^2] \tag{3.37}$$

where,

$$\mathbf{\Omega} = \frac{1}{2}\left[\frac{\partial u_i}{\partial x_j} - \frac{\partial u_j}{\partial x_i}\right] \tag{3.38}$$

$$\mathbf{S} = \frac{1}{2}\left[\frac{\partial u_i}{\partial x_j} + \frac{\partial u_j}{\partial x_i}\right] \tag{3.39}$$

The normalized helicity provides the direction of the swirl of the vortex relative to the stream-wise velocity component, which is not available in Q-criterion [15]

$$H_n = \frac{\mathbf{V} \cdot \mathbf{\Omega}}{||\mathbf{V}||||\mathbf{\Omega}||} \tag{3.40}$$

Resolved TKE (k_r) is obtained by partitioning the resolved velocity (U_i) into time averaged ($\overline{U_i}$) and fluctuation components u_i as:

$$U_i = \overline{U_i} + u_i : \ i = 1, 2, 3 \tag{3.41}$$

$$k_r = \frac{1}{2}\overline{u_i U_i} \tag{3.42}$$

The total TKE is $k_t = k + k_r$. The resolved turbulence level in the LES region is computed as $\frac{k_r}{k_t} * 100$.

The mean local error e, for the velocity components was calculated using the equation below:

$$e = \frac{1}{N}\left|\sum_R \frac{\overline{u_S} - \overline{u_D}}{max(\overline{u_D}) - min(\overline{u_D})}\right| \tag{3.43}$$

$\overline{u_D}$ is the time average of the velocity components for the experimental data. $\overline{u_S}$ is obtained by time averaging the velocity components for CFD over two flow time then interpolating the time averaged values into the PIV zone. R is the PIV zone below free surface and N is the total number of points. The free surface was found by averaging the CFD level set function over two flow times and interpolating it into PIV zone. The inverse distance algorithm was used to compute the interpolations. The maximum and minimum of the time average values were found over the zone R.

CHAPTER 4
URANS RESULTS USING GR GRID

URANS was conducted at large range of $0.3 \leq Fr \leq 0.77$ and $0^0 \leq \beta \leq 30^0$ using GR. The model was free to sink and trim. The simulations were unsteady for large drift angles. Time history and fast Fourier transformation (FFT) are shown in Figures 4.1-4.8.

4.1 Validation of Integral Variables

Hydrodynamic forces, moments and motions for $\beta = 0^0$ were compared to the experimental results from INSEAN, BSHC, and TU Delft facilities. In general, agreement between experiments conducted at the TU Delft and INSEAN facilities, and CFD were achieved at $\beta = 0^0$ with force (X), sink (σ), and trim (τ) errors less than $13\%D$ (Table 4.1 and Figure 4.9). Although there was a good agreement on the force between CFD and BSHC experiments, the motions showed large error with more than $30\%D$ for sink and trim. The discrepancy in the experimental results could be attributed to the difference in non-dimensional depth of the experiments and vertical center of gravity or experimental setup.

Forces (X and Y) and moment (N) were compared to BSHC experimental results and the motions (σ and τ) were compared to both BSHC and INSEAN experimental results for $0^0 \leq \beta \leq 24^0$ (Table 4.2 and Figures 4.10-4.16). The total forces showed good agreement between EFD and CFD for all Froude numbers and drift angles while total moment had good agreement for all the cases except at very large drift angles. Difference between forces on demihulls were underpredicted, especially for large drift cases, which could explain the discrepancy between EFD and CFD for the moment at large drift angles. CFD motions showed better agreement with INSEAN experiments compared to BSHC experiments, similar to what was observed for straight ahead condition. Large scatter was observed for the motion measurements which could indicate large experimental uncertainty. Overall, EFD and CFD exhibited good agreement validating the CFD-Ship Iowa V4.5 research code for predicting the integral variables of the catamaran at a large range of Froude numbers and drift angles.

4.2 Integral Variable Patterns, Vortical Structures and Wave Patterns

Total forces (X_t, Y_t), moments (N_t), pressure (X_p, Y_p, N_p) and frictional (X_f, Y_f, N_f) components, and the motions were compared between CFD results for all cases(Figures 4.17). For large drift angles ($\beta \geq 15^0$) and Froude numbers (Fr=0.61, 0.77), the total X_t and Y_t showed small difference compared to lower Froude numbers. An increase in β resulted in the pressure component of the forces being larger than the frictional component. This was expected because the flow is vortex dominated at large drift angles. Wave patterns displayed wave breaking at sufficiently high drift angles (Figures 4.18-4.21). Wave elevation exceeded the deck height at $Fr = 0.77$ and $\beta = 30^0$. The GR grid did not include the ship deck, hence inappropriate for cases where wave elevations exceed deck height. The boundary layer grid for G1-G5 included a deck to resolve this problem. Vortical structures have been identified and named for all cases (Figures 4.22-4.29). Two counter rotating at each hull is observed for straight ahead conditions. Large vortex from the fore-body, two counter rotating keel and stern vorticies were observed for most static drift cases. Additionally, wave induced vorticies were observed at sufficiently large drift angle. Very different vortical structures were observe for extreme cases of $Fr = 0.61, 0.77$ and $\beta = 30^0$. Vortex core of the large fore-body vorticies, PF and SF, have been identified using the Q-criterion and marked with black dots on Figures 4.30-4.50. The vortex structures and wave elevations were used to design the grids G1-G5.

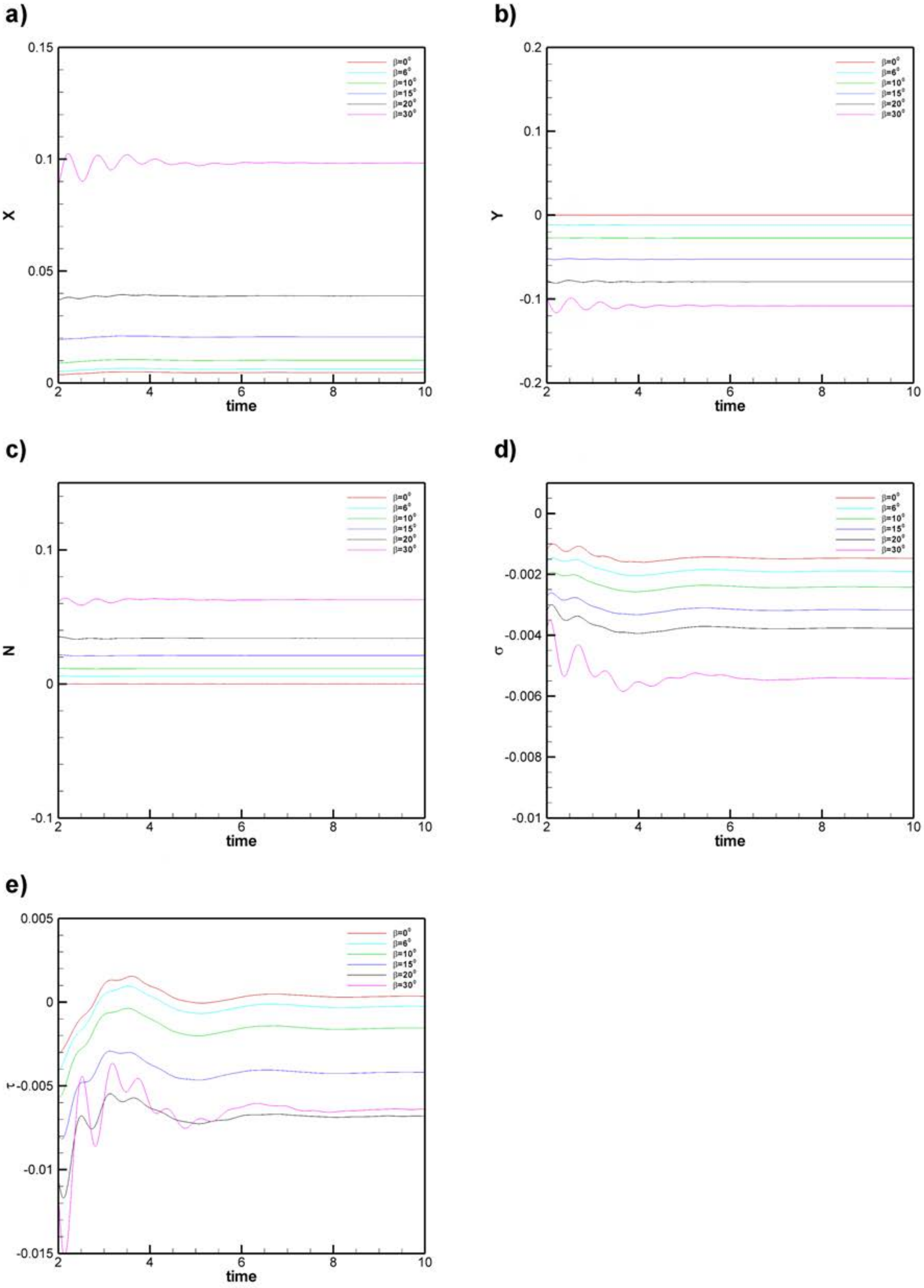

Figure 4.1: Time history for $Fr = 0.3$ and $0 \leq \beta \leq 30$ using GR

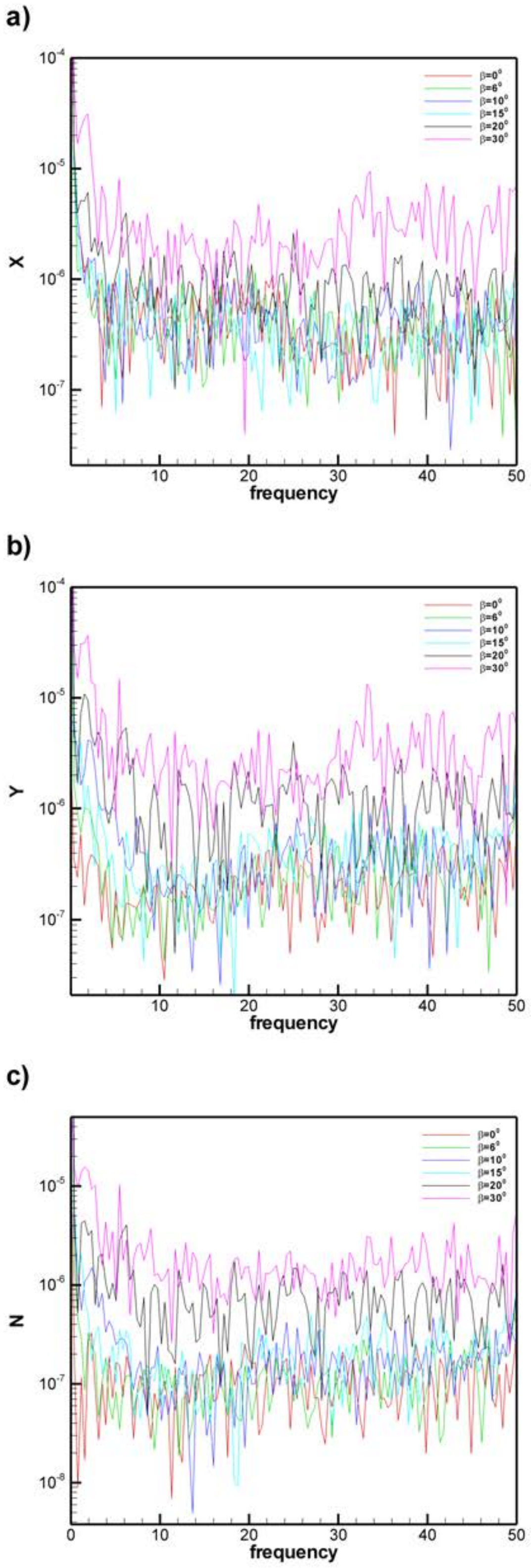

Figure 4.2: FFT for $Fr = 0.3$ and $0 \leq \beta \leq 30$ using GR

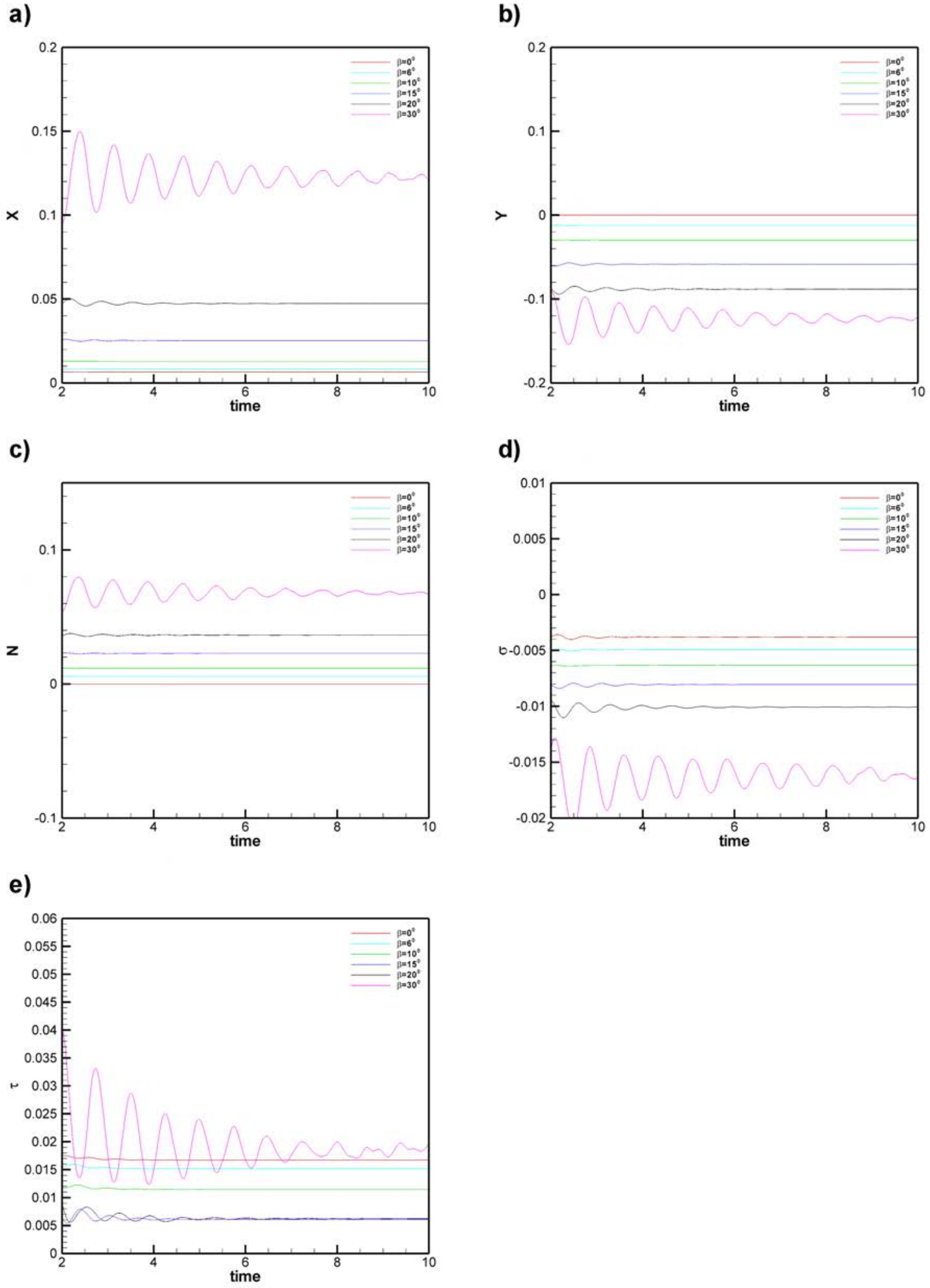

Figure 4.3: Time history for $Fr = 0.45$ and $0 \leq \beta \leq 30$ using GR

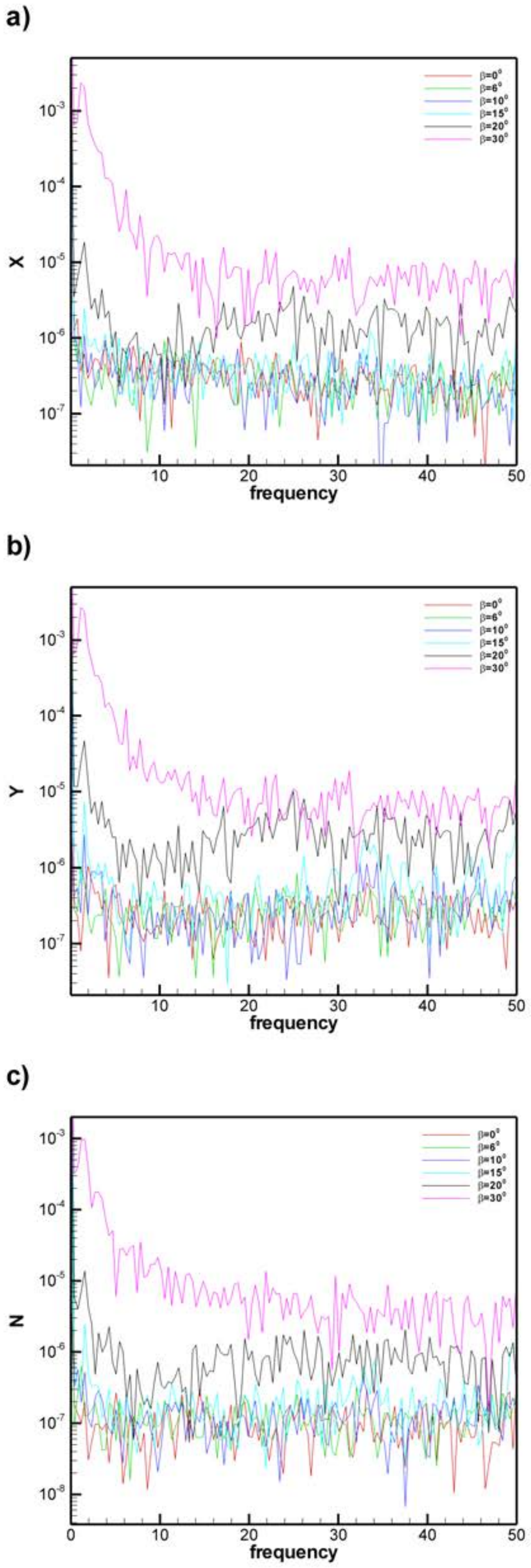

Figure 4.4: FFT for $Fr = 0.45$ and $0 \leq \beta \leq 30$ using GR

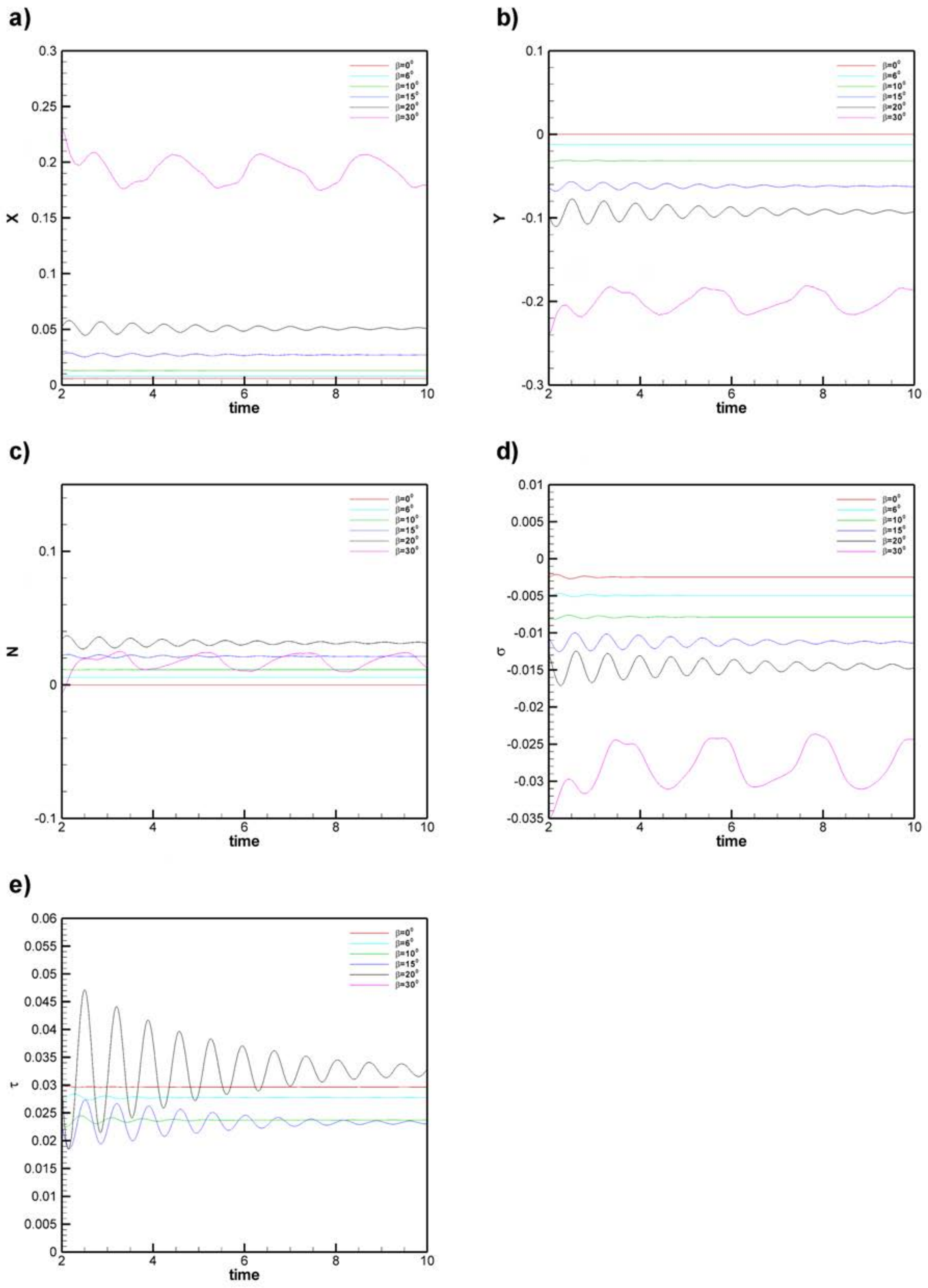

Figure 4.5: Time history for $Fr = 0.61$ and $0 \leq \beta \leq 30$ using GR

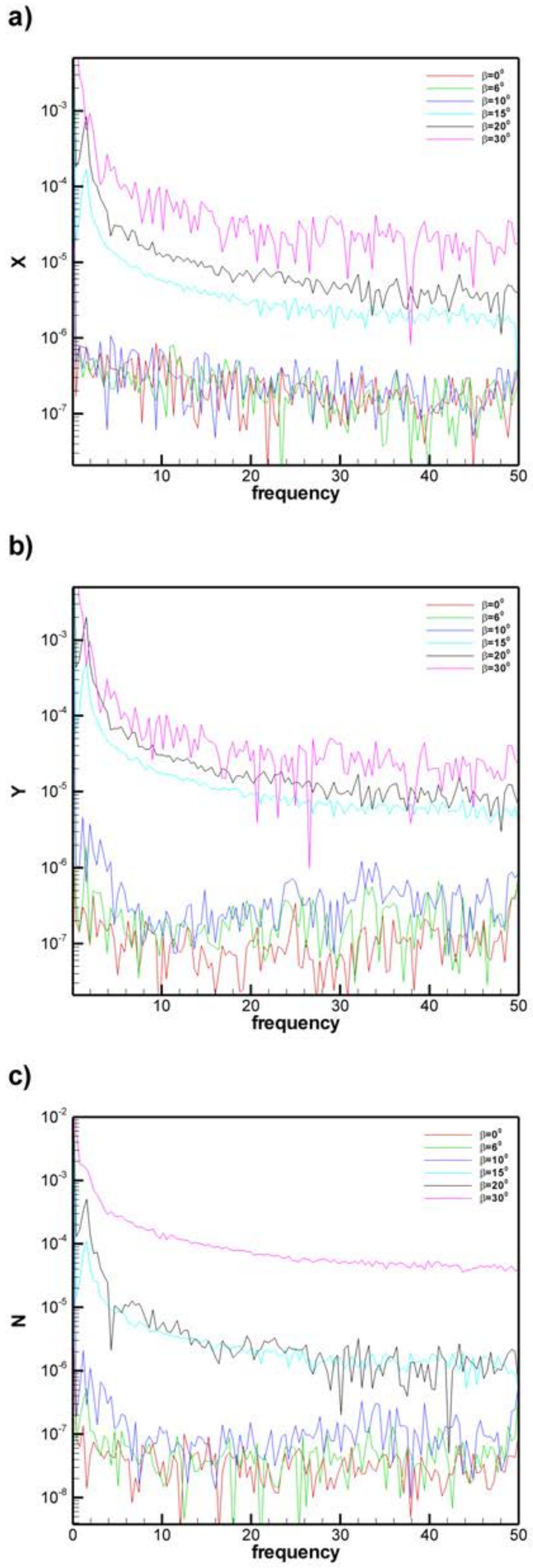

Figure 4.6: FFT for $Fr = 0.61$ and $0 \leq \beta \leq 30$ using GR

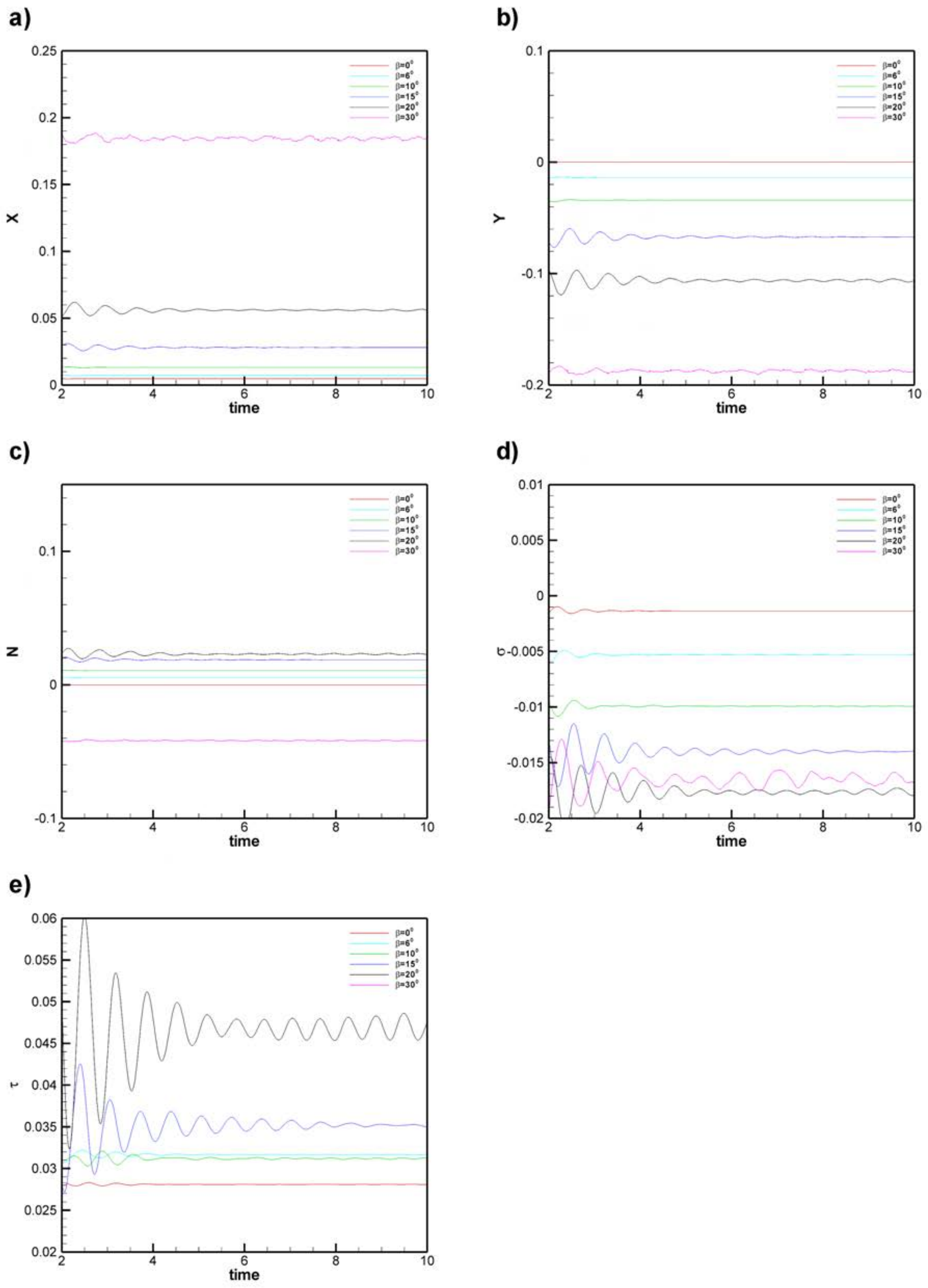

Figure 4.7: Time history for $Fr = 0.77$ and $0 \leq \beta \leq 30$ using GR

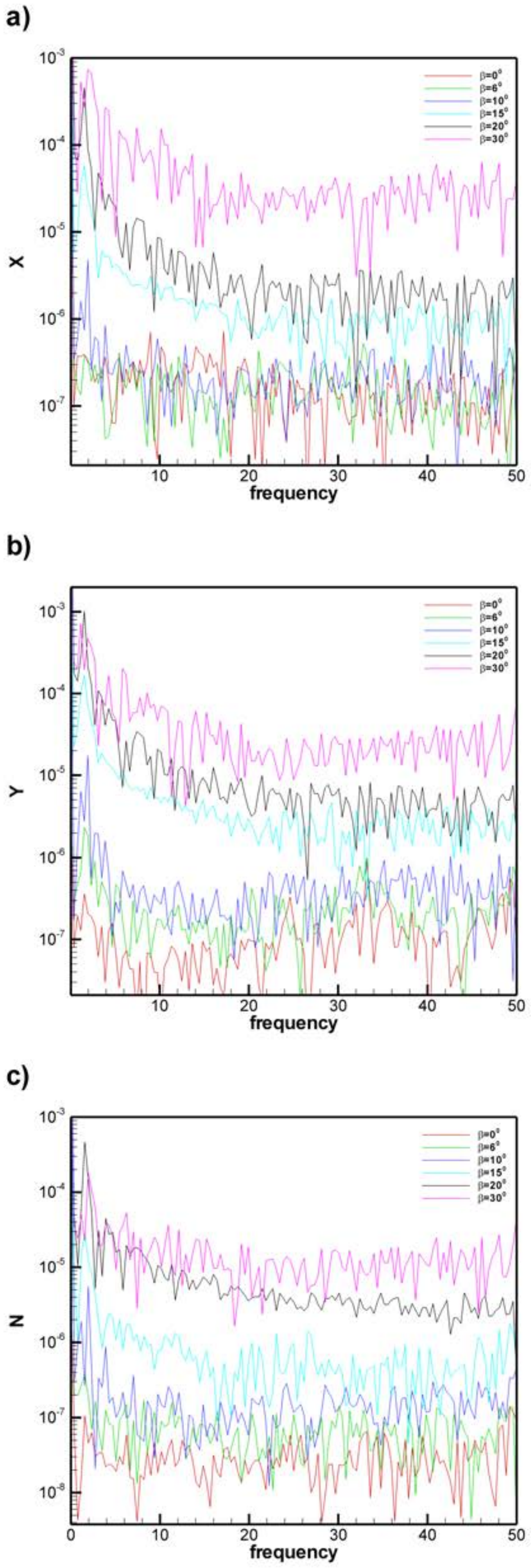

Figure 4.8: FFT for $Fr = 0.77$ and $0 \leq \beta \leq 30$ using GR

Table 4.1: CFD error for X, σ, τ at $\beta = 0^0$ using GR

	BSHC			INSEAN			TU Delft		
Fr	X	σ	τ	X	σ	τ	X	σ	τ
0.3	-1.82	-	-	11.22	-0.05	2.12	4.56	0.48	7.62
0.45	8.59	30.19	33.93	14.74	0.07	23.64	8.45	-0.06	-5.01
Avg.	5.2	30.19	33.93	12.98	0.06	12.88	6.5	0.27	6.31

Table 4.2: CFD error for X,Y, N, σ, and τ at $\beta \geq 0^0$ using GR

	BSHC					INSEAN				
β	X	Y	N	σ	τ	X	Y	N	σ	τ
0	10.6	-	-	31.0	29.0	-	-	-	29.1	26.1
6	11.1	5.9	13.3	33.8	29.9	-	-	-	26.8	26.2
10	2.6	12.8	3.2	21.0	49.5	-	-	-	-	-
Avg.	8.1	9.4	8.2	28.6	36.2	-	-	-	27.9	26.2

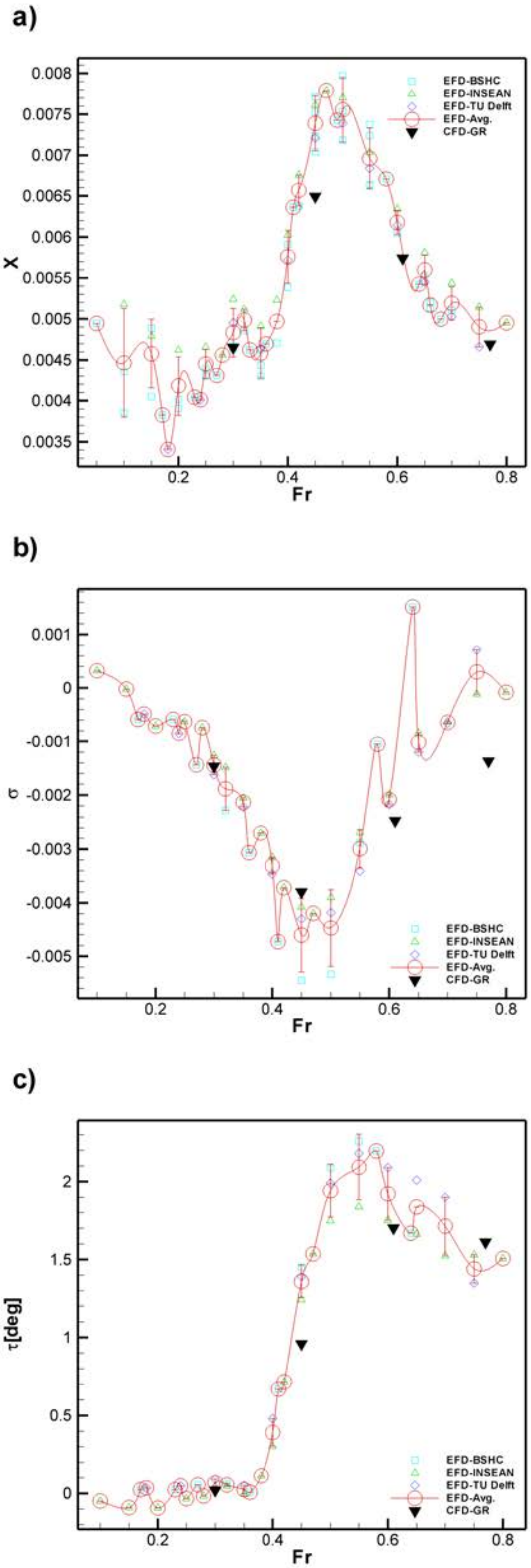

Figure 4.9: EFD-CFD comparison of X, σ, τ at $\beta = 0^0$ using GR

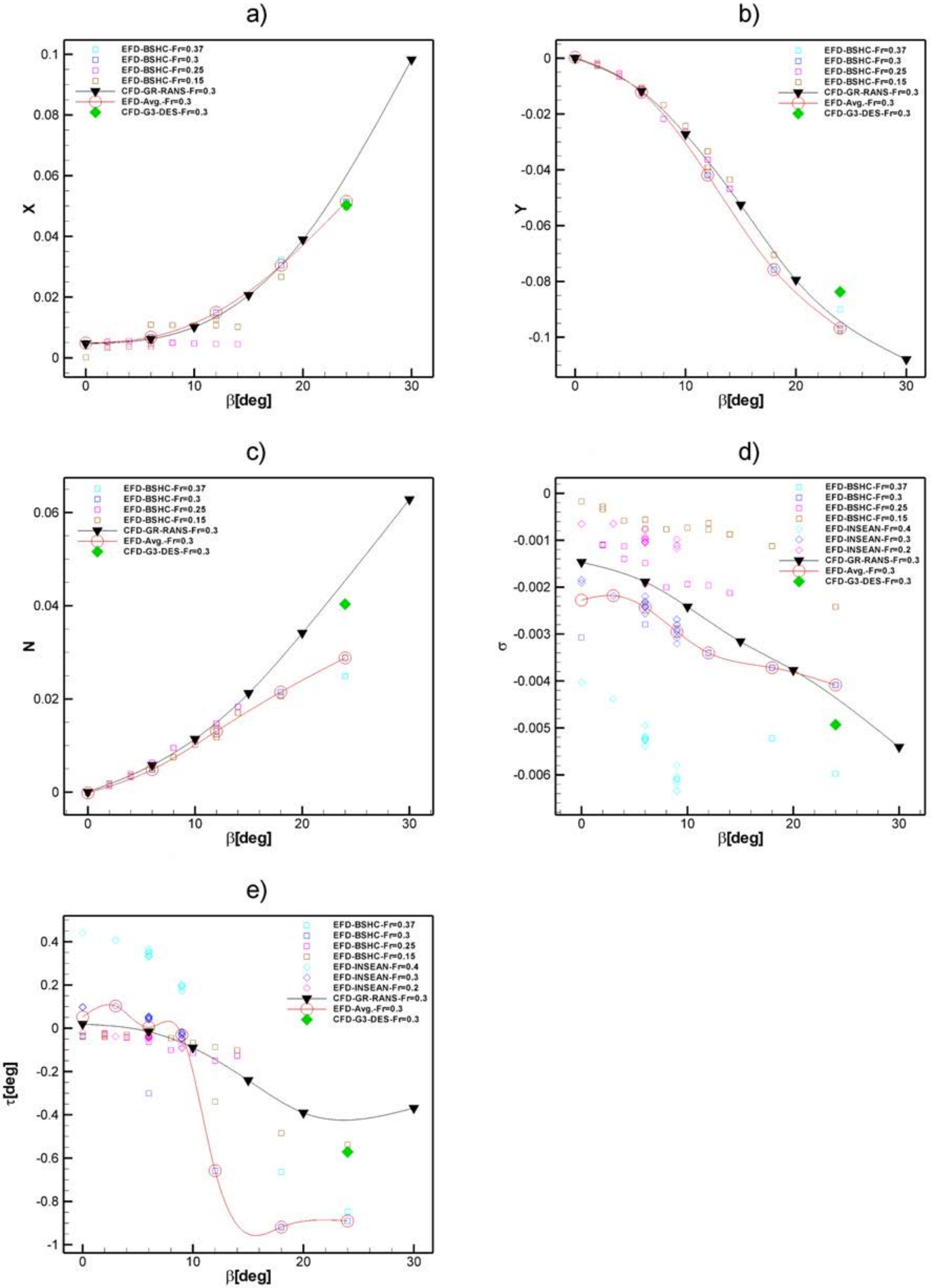

Figure 4.10: Comparison of X,Y, N, σ, and τ for EFD at $0.15 \leq Fr \leq 0.4$ and CFD at $Fr = 0.3$ with $0^0 \leq \beta \leq 30^0$ using GR

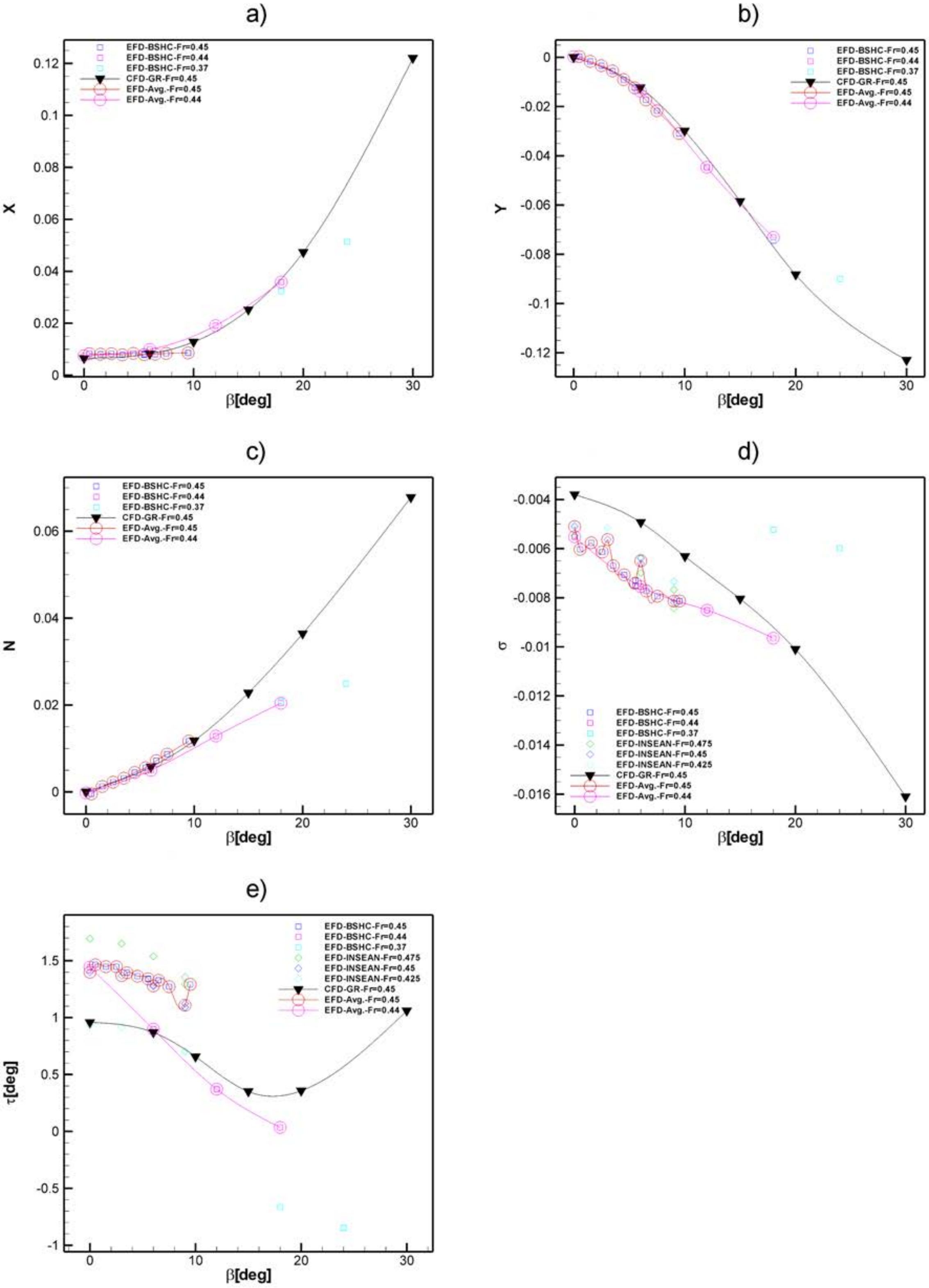

Figure 4.11: Comparison of X,Y, N, σ, and τ for EFD at $0.37 \leq Fr \leq 0.475$ and CFD at $Fr = 0.45$ with $0^0 \leq \beta \leq 30^0$ using GR

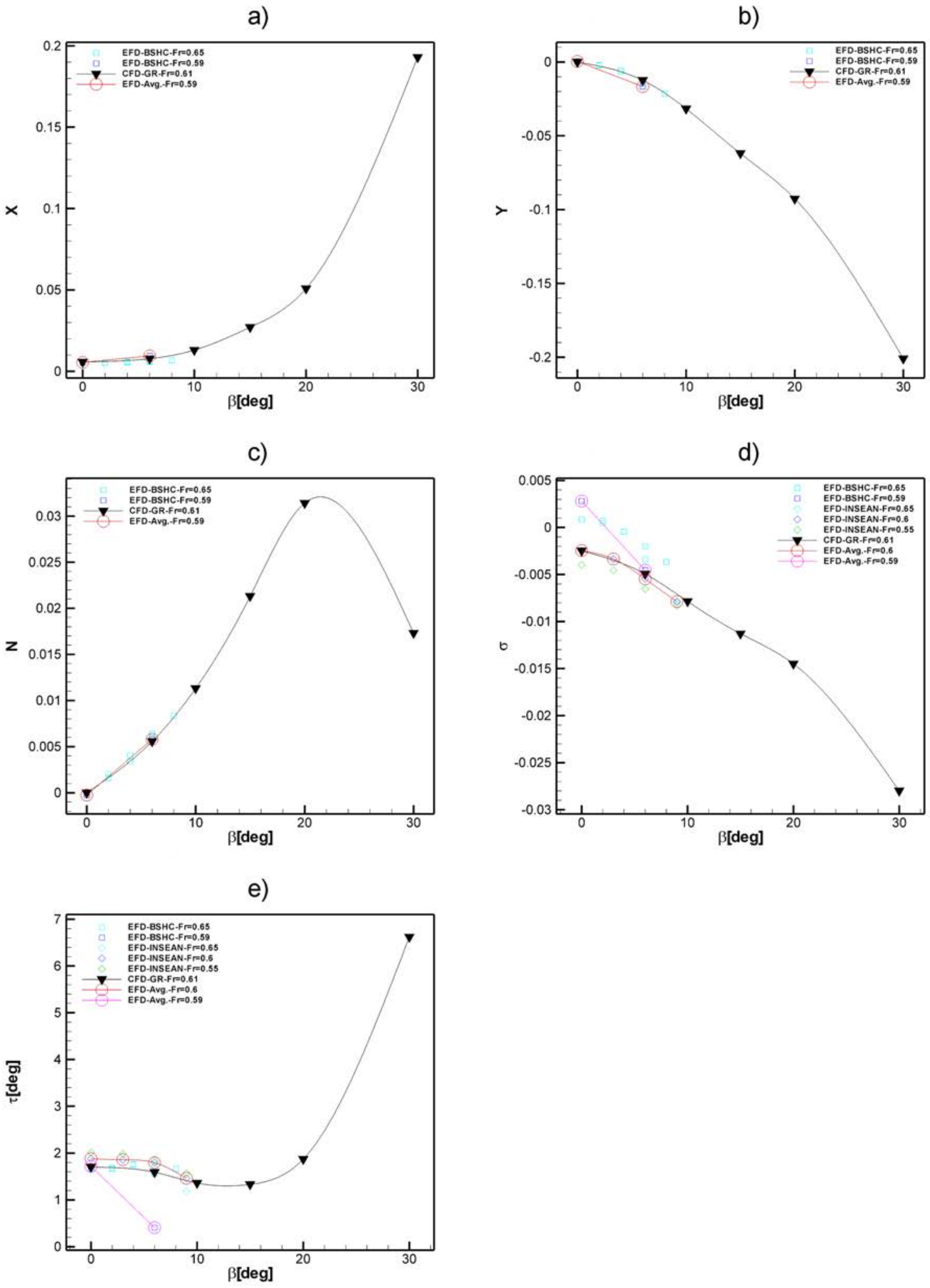

Figure 4.12: Comparison of X,Y, N, σ, and τ for EFD at $0.59 \leq Fr \leq 0.65$ and CFD at $Fr = 0.61$ with $0^0 \leq \beta \leq 30^0$ using GR

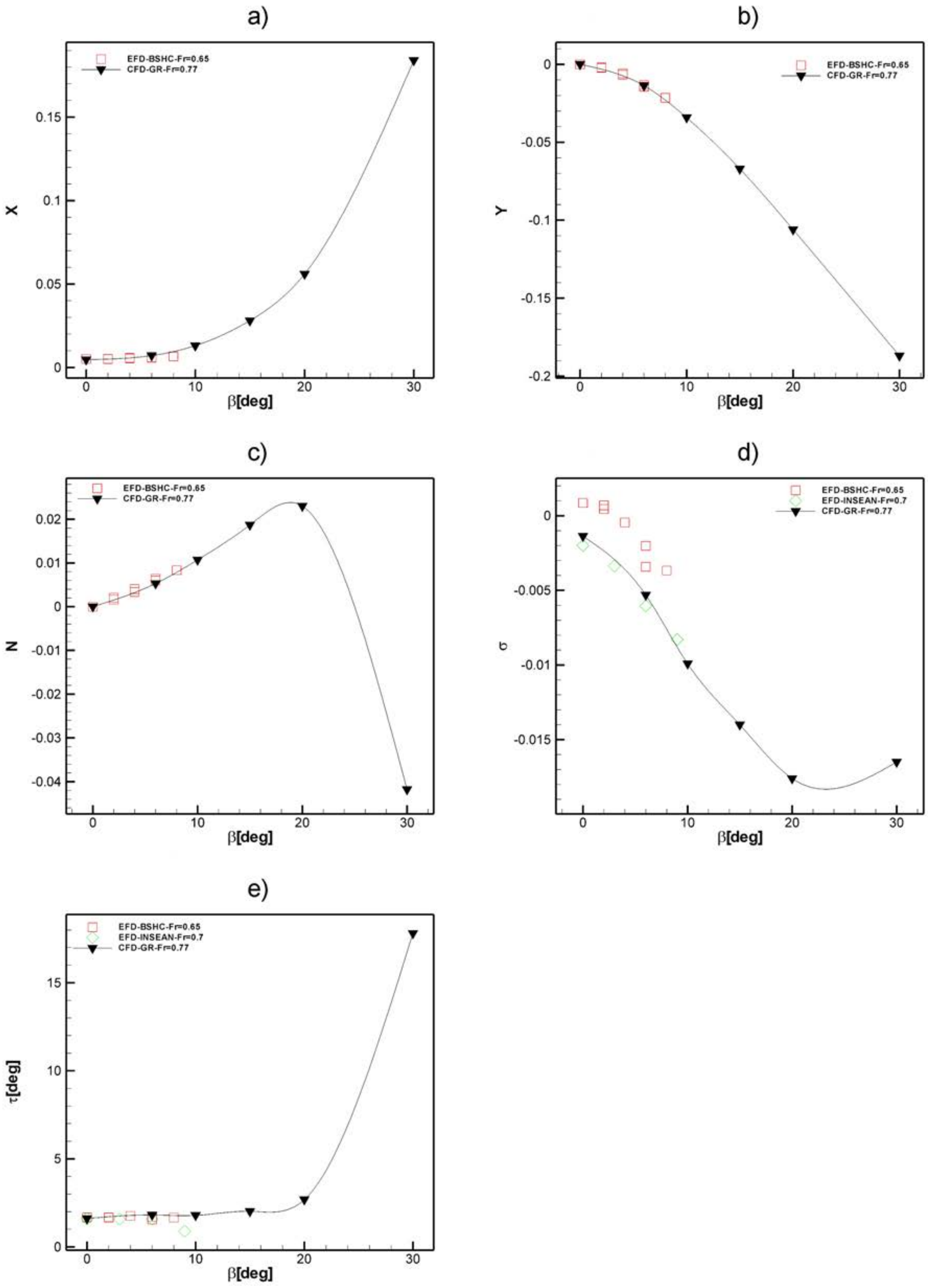

Figure 4.13: Comparison of X,Y, N, σ, and τ for EFD at $0.65 \leq Fr \leq 0.7$ and CFD at $Fr = 0.77$ with $0^0 \leq \beta \leq 30^0$ using GR

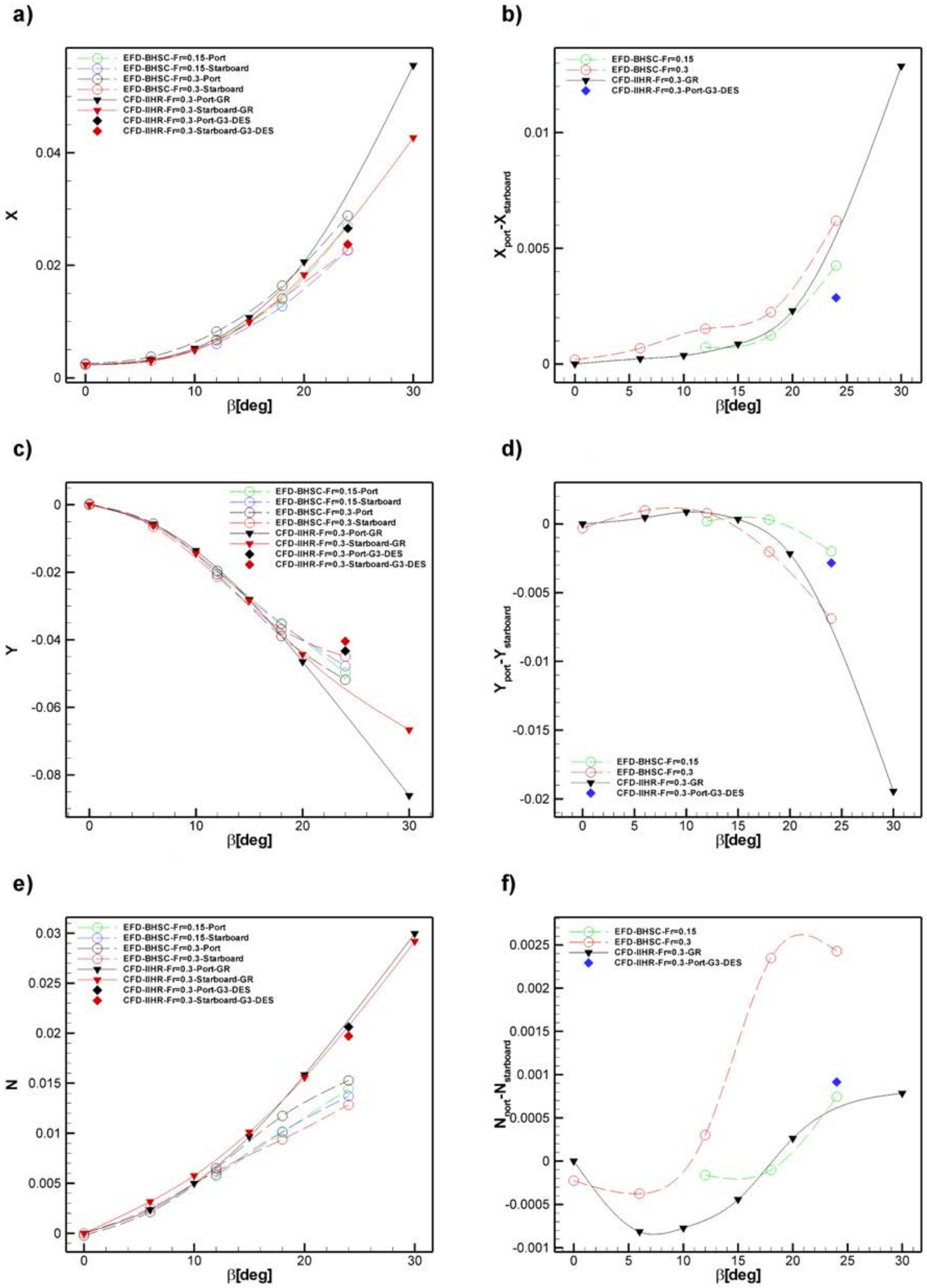

Figure 4.14: Comparison of X,Y, and N for EFD at $0.15 \leq Fr \leq 0.3$ and CFD at $Fr = 0.3$ with $0^0 \leq \beta \leq 30^0$ using GR on demihull

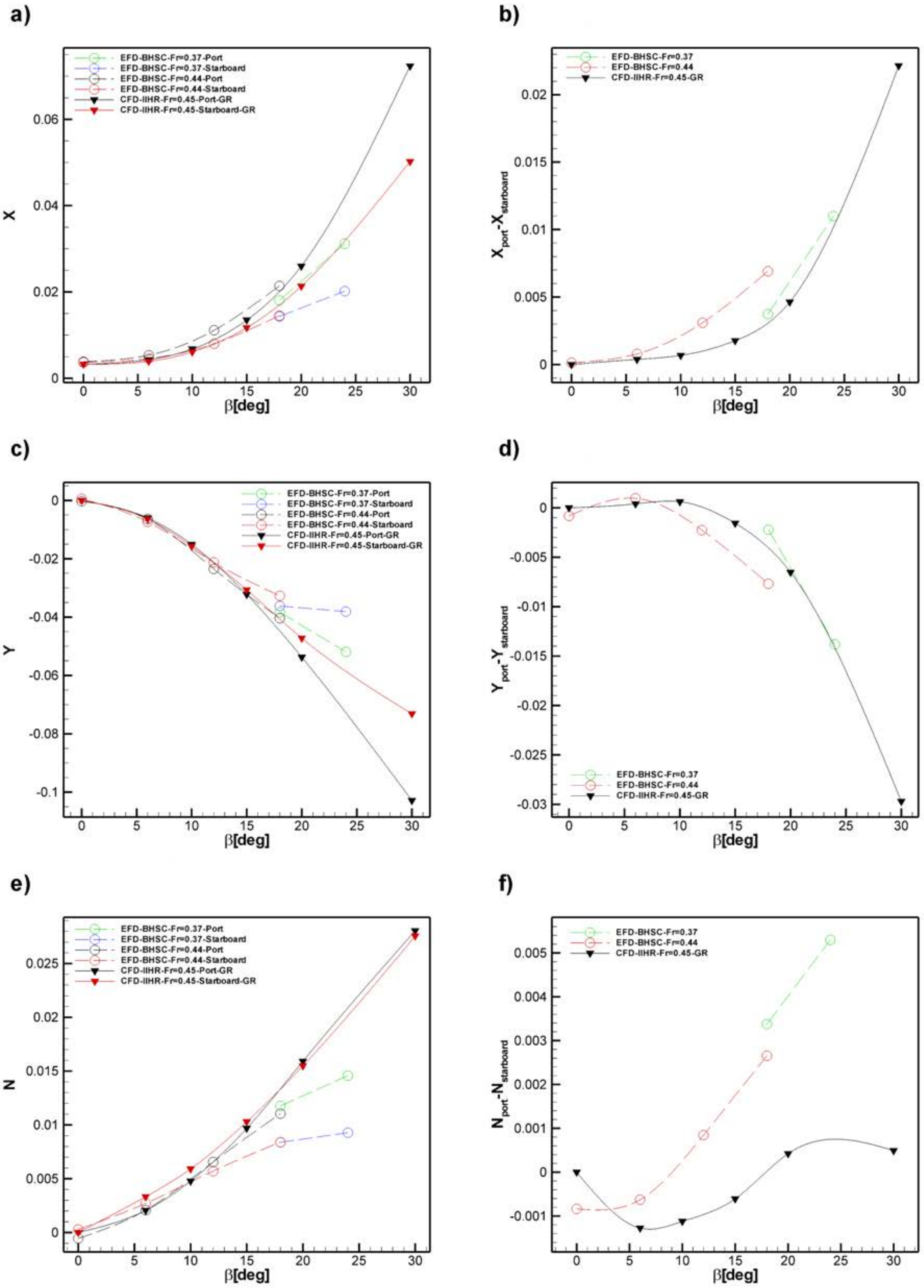

Figure 4.15: Comparison of X,Y, and N for EFD at $0.37 \leq Fr \leq 0.44$ and CFD at $Fr = 0.45$ with $0^0 \leq \beta \leq 30^0$ using GR on demihull

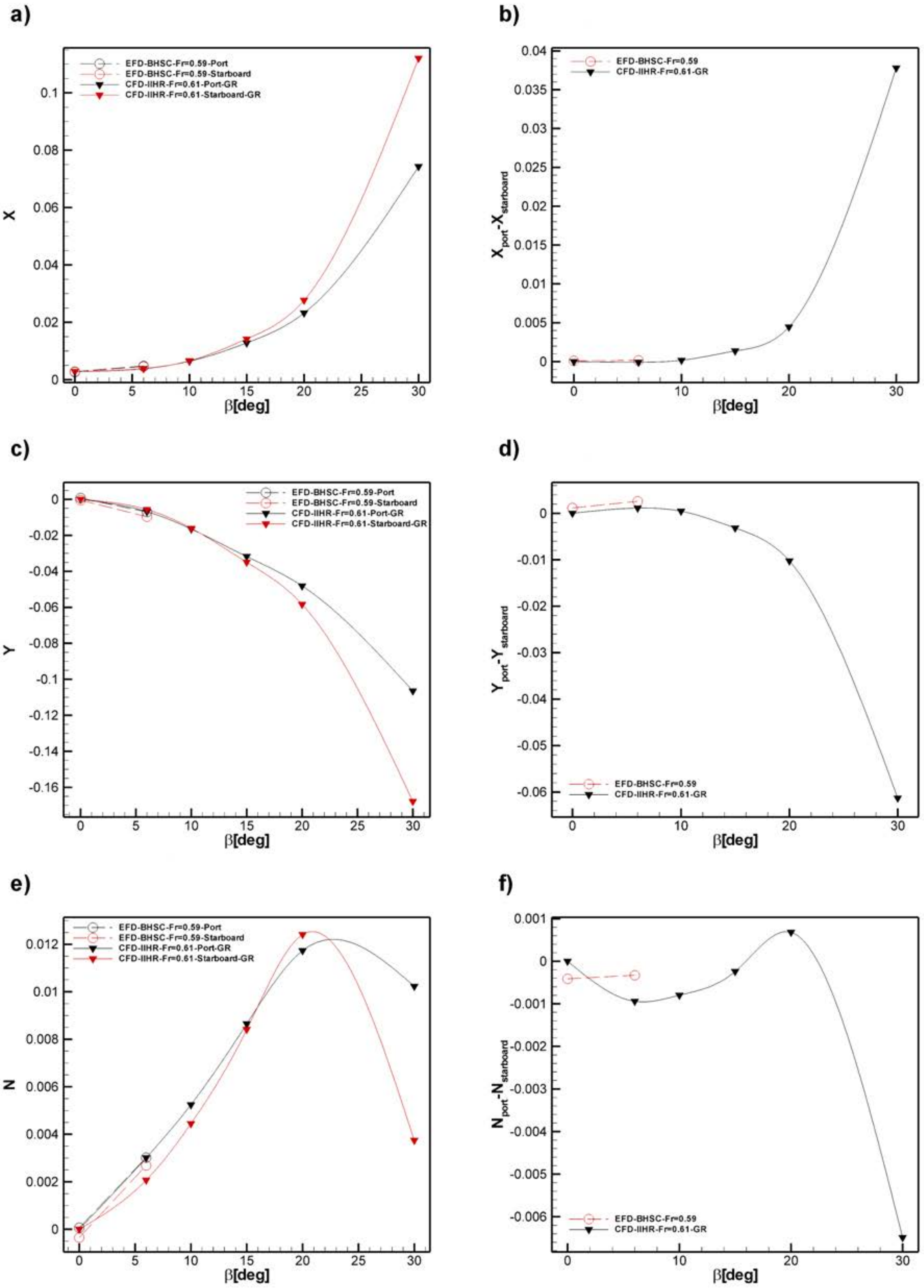

Figure 4.16: Comparison of X,Y, and N for EFD at $Fr = 0.6$ and CFD at $Fr = 0.61$ with $0^0 \leq \beta \leq 30^0$ using GR on demihull

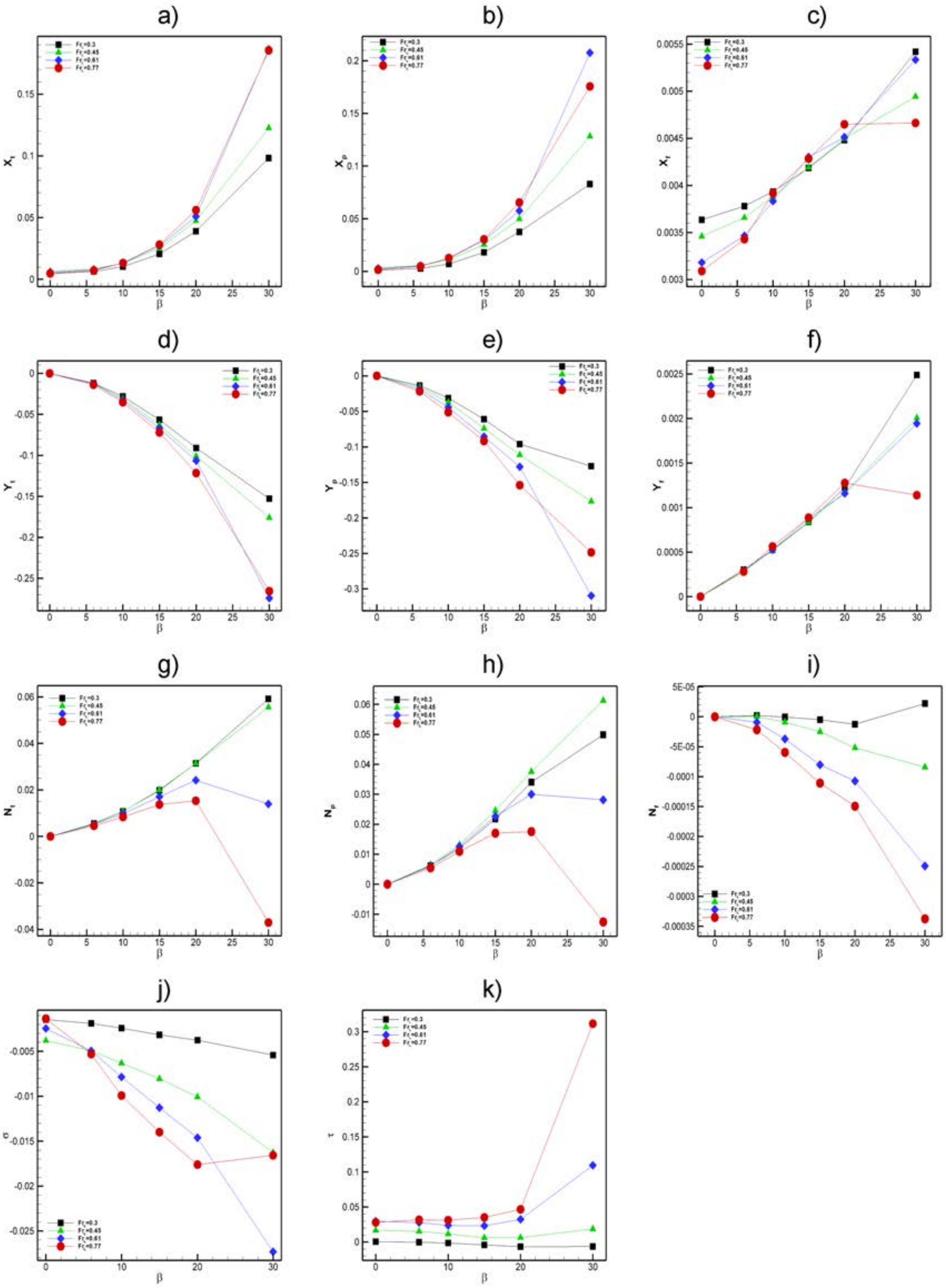

Figure 4.17: Comparison of total, pressure and frictional components of the integral variables using GR for CFD results at $0.3 \leq Fr \leq 0.77$ and $0^0 \leq \beta \leq 30^0$

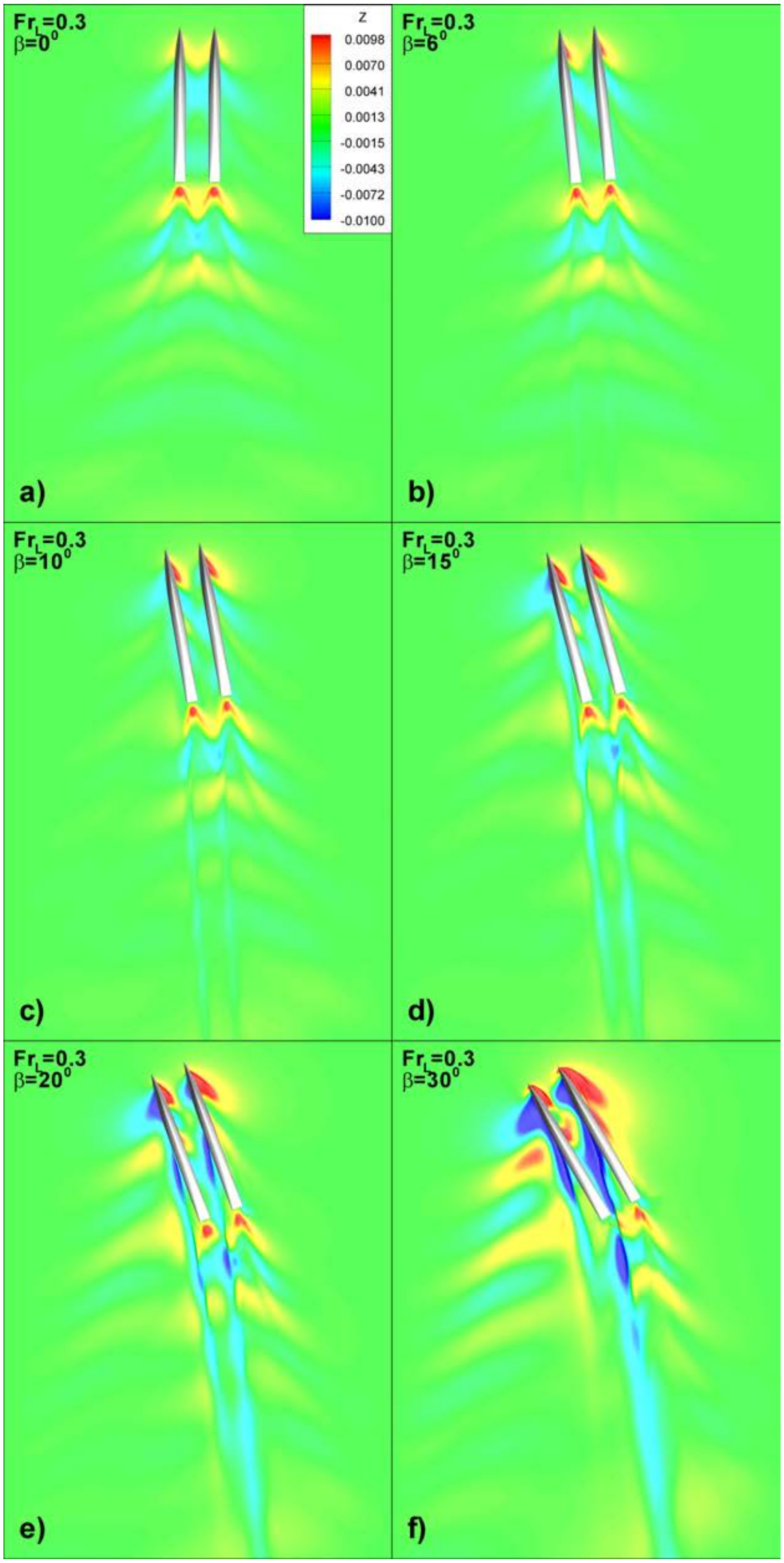

Figure 4.18: Wave patterns at $Fr = 0.3$ and $0^0 \leq \beta \leq 30^0$ using GR

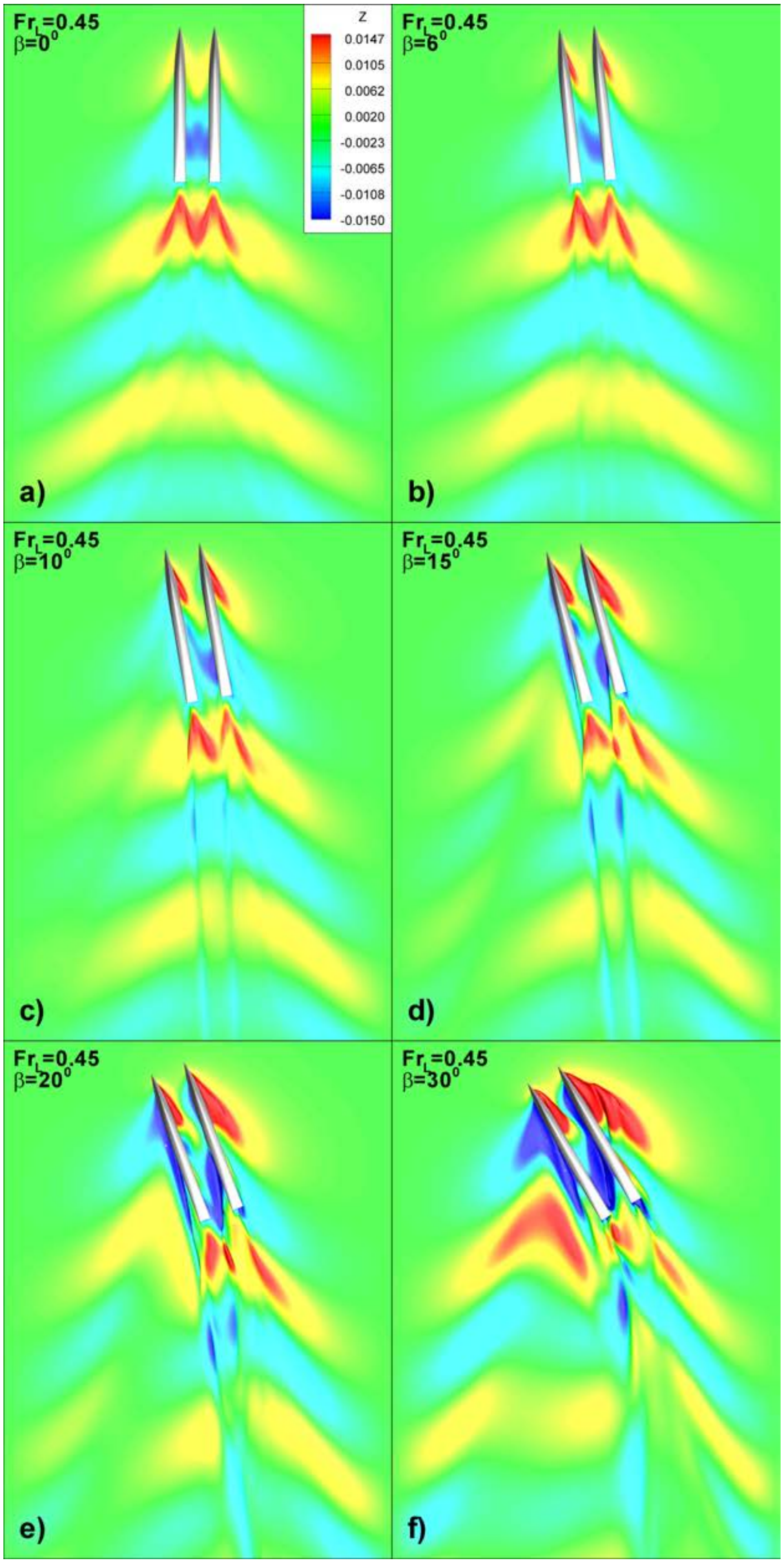

Figure 4.19: Wave patterns at $Fr = 0.45$ and $0^0 \leq \beta \leq 30^0$ using GR

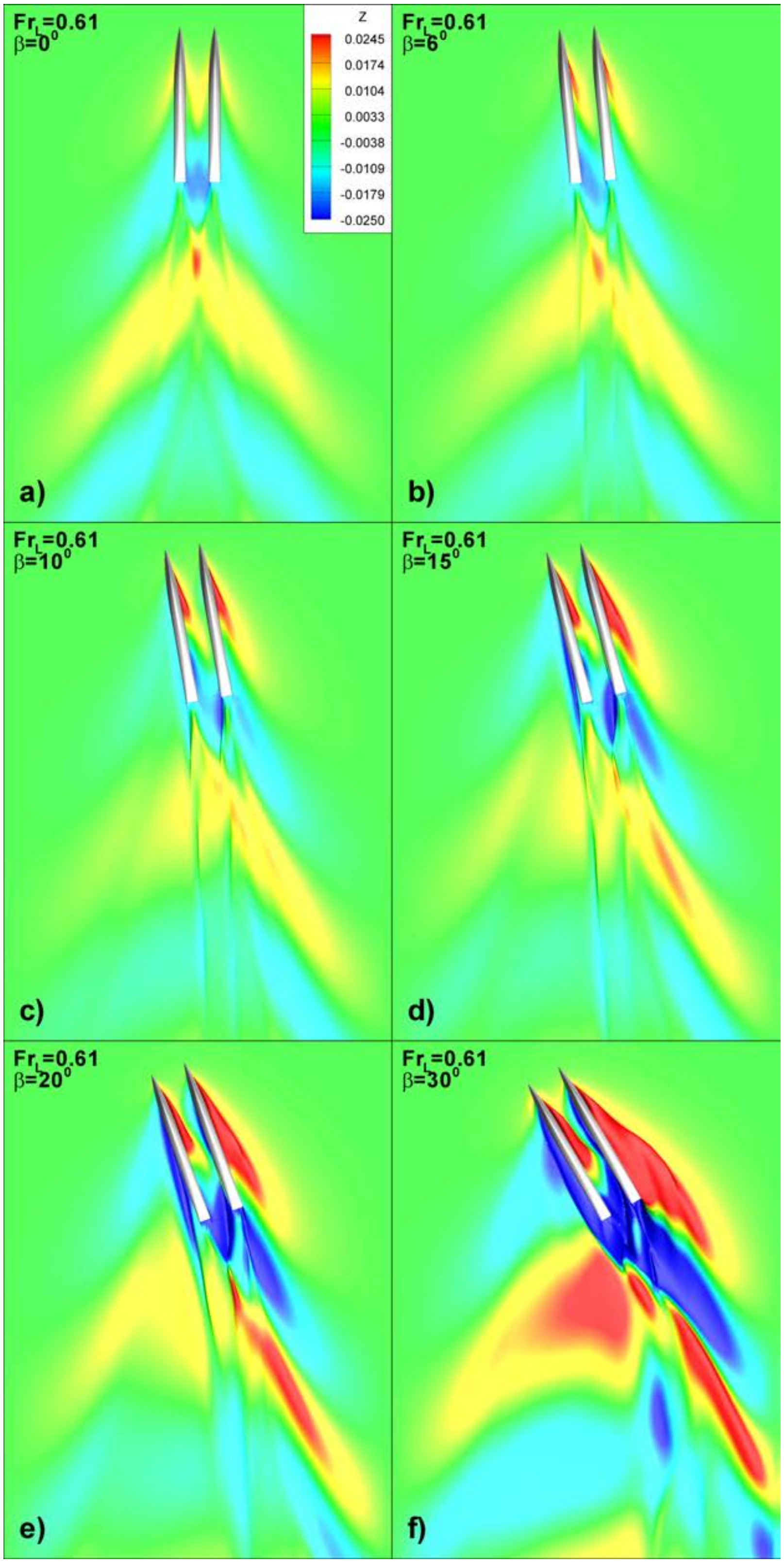

Figure 4.20: Wave patterns at $Fr = 0.61$ and $0^0 \leq \beta \leq 30^0$ using GR

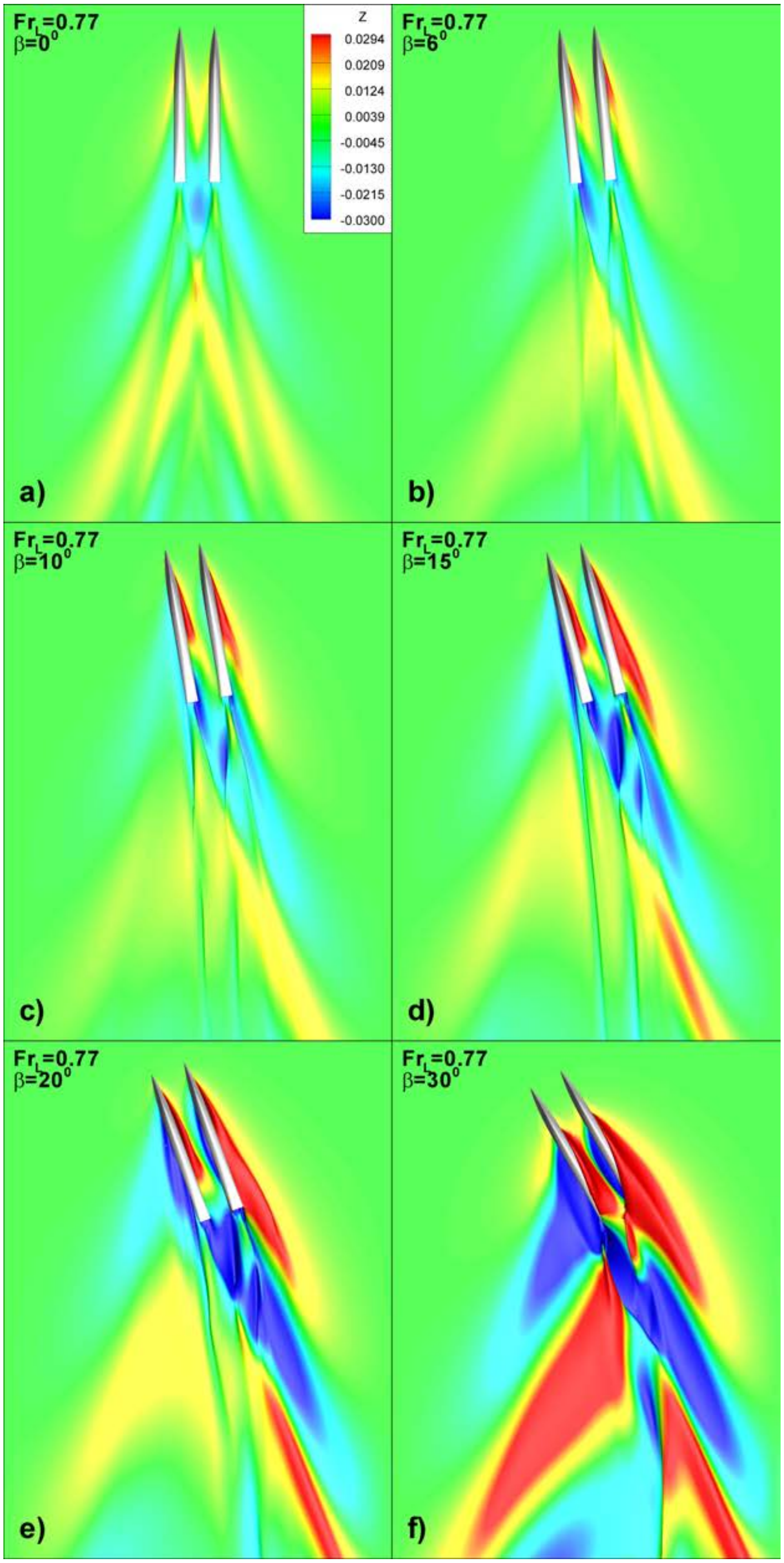

Figure 4.21: Wave patterns at $Fr = 0.77$ and $0^0 \leq \beta \leq 30^0$ using GR

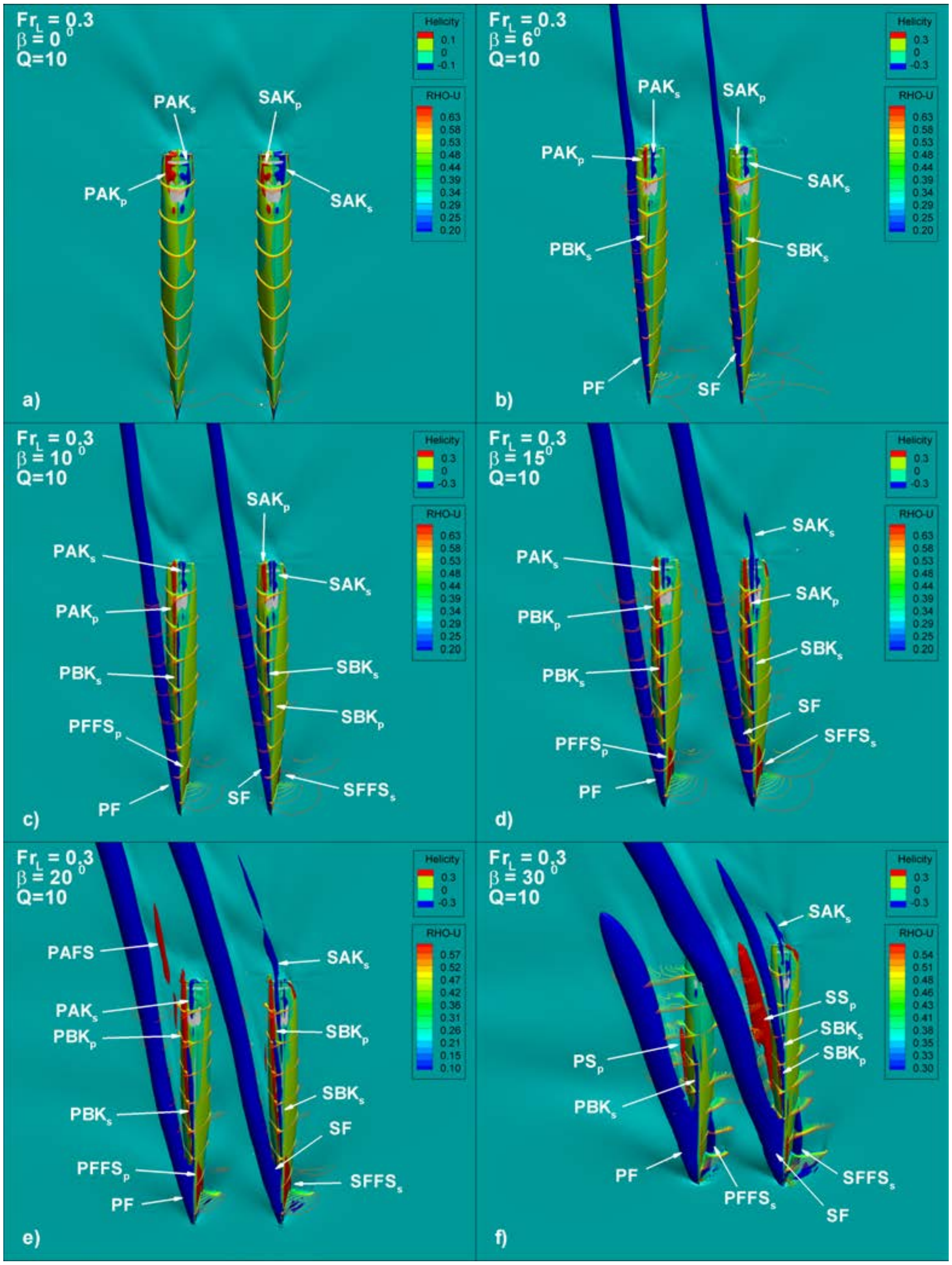

Figure 4.22: Vortex structures and boundary layer at $Fr = 0.3$ and $0^0 \leq \beta \leq 30^0$ using GR

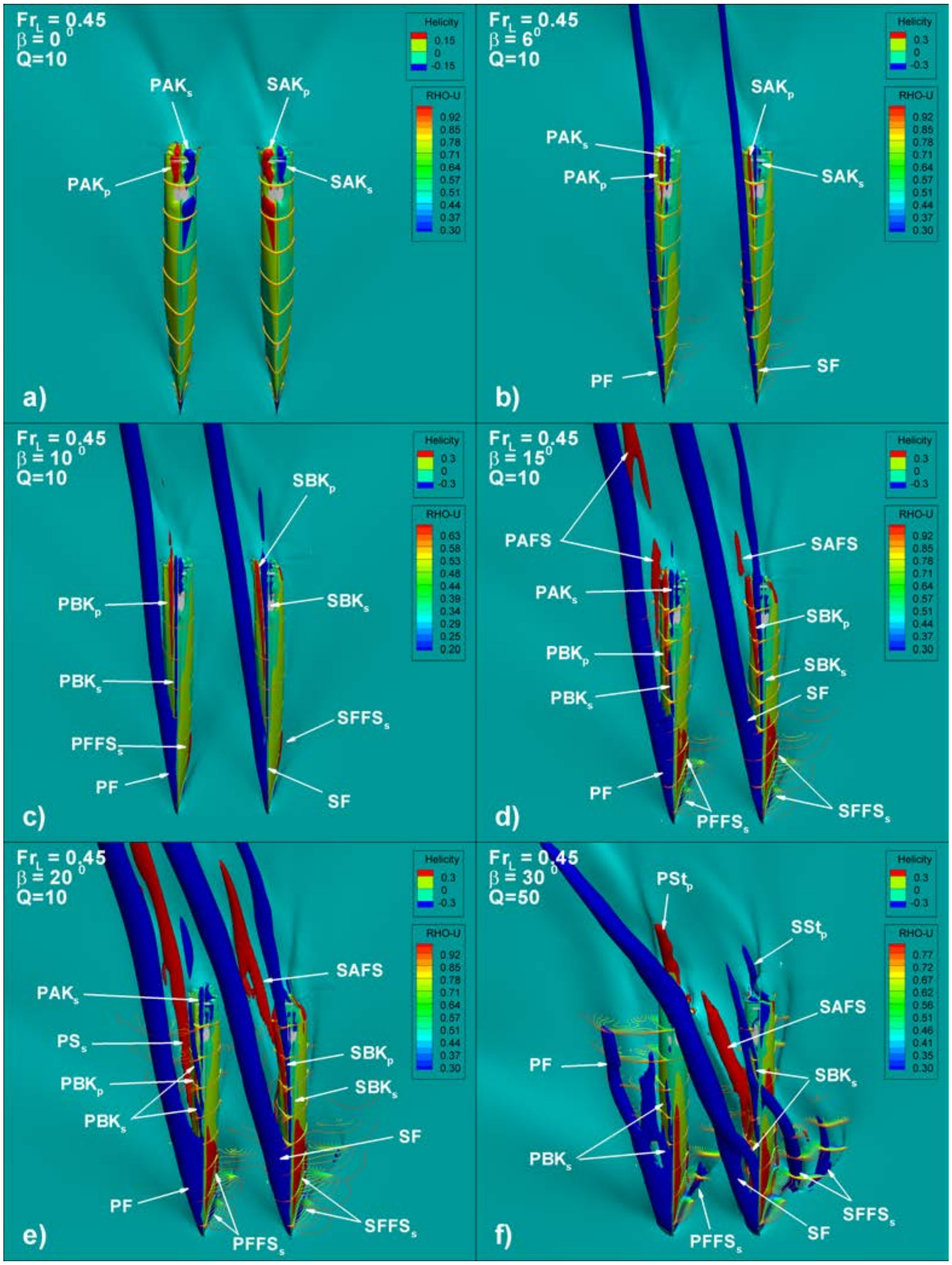

Figure 4.23: Vortex structures and boundary layer at $Fr = 0.45$ and $0^0 \leq \beta \leq 30^0$ using GR

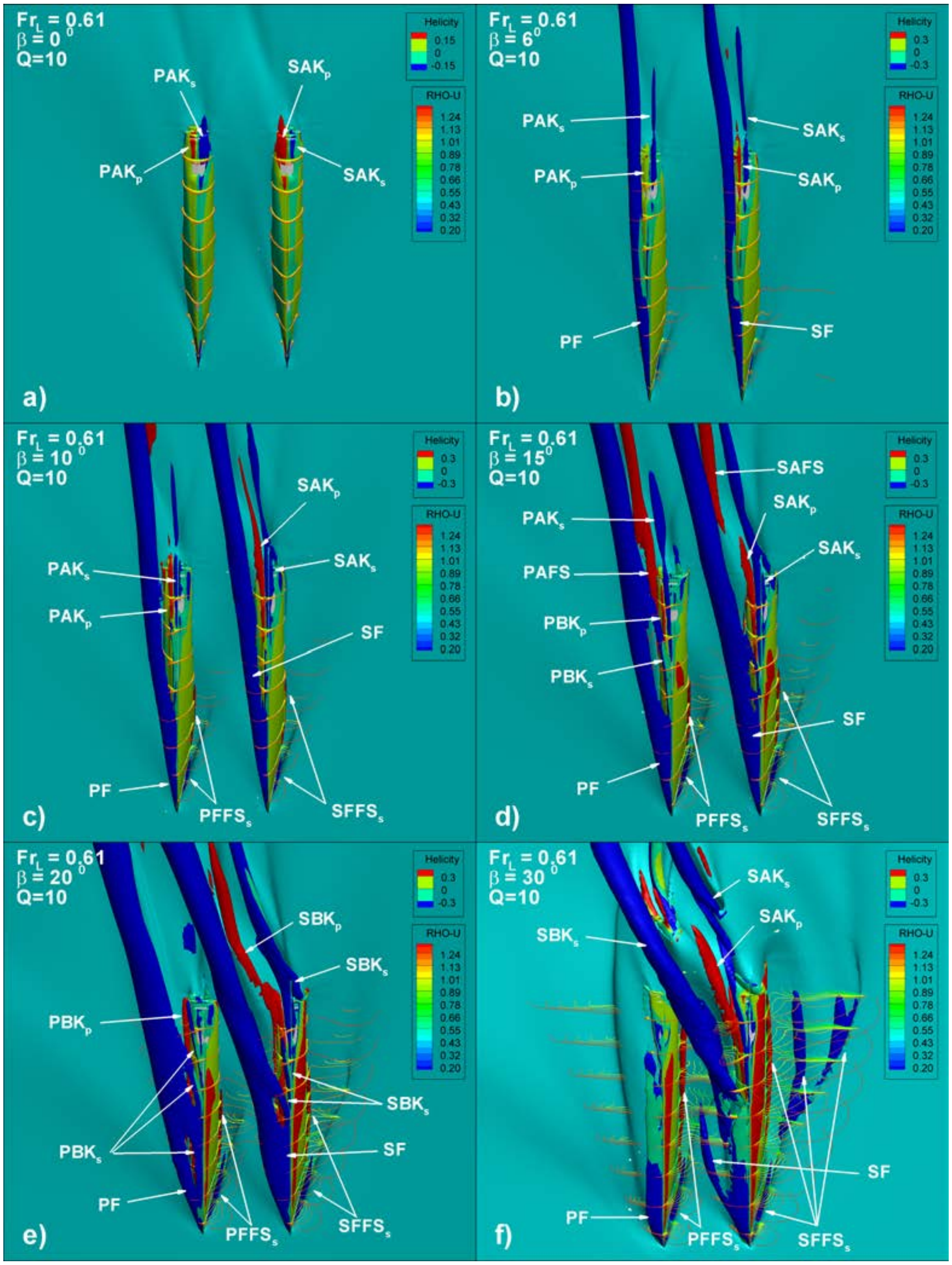

Figure 4.24: Vortex structures and boundary layer at $Fr = 0.61$ and $0^0 \leq \beta \leq 30^0$ using GR

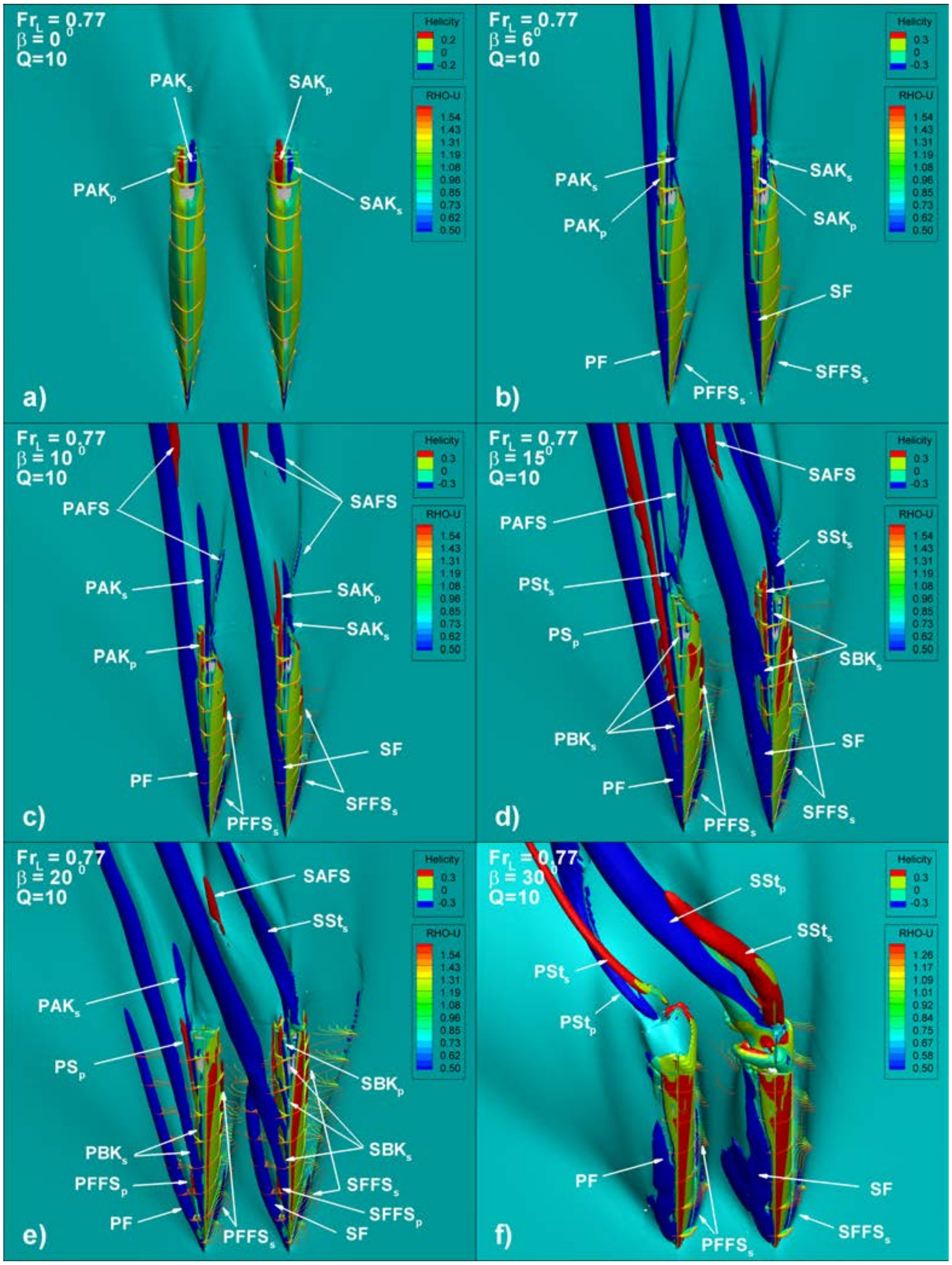

Figure 4.25: Vortex structures and boundary layer at $Fr = 0.77$ and $0^0 \leq \beta \leq 30^0$ using GR

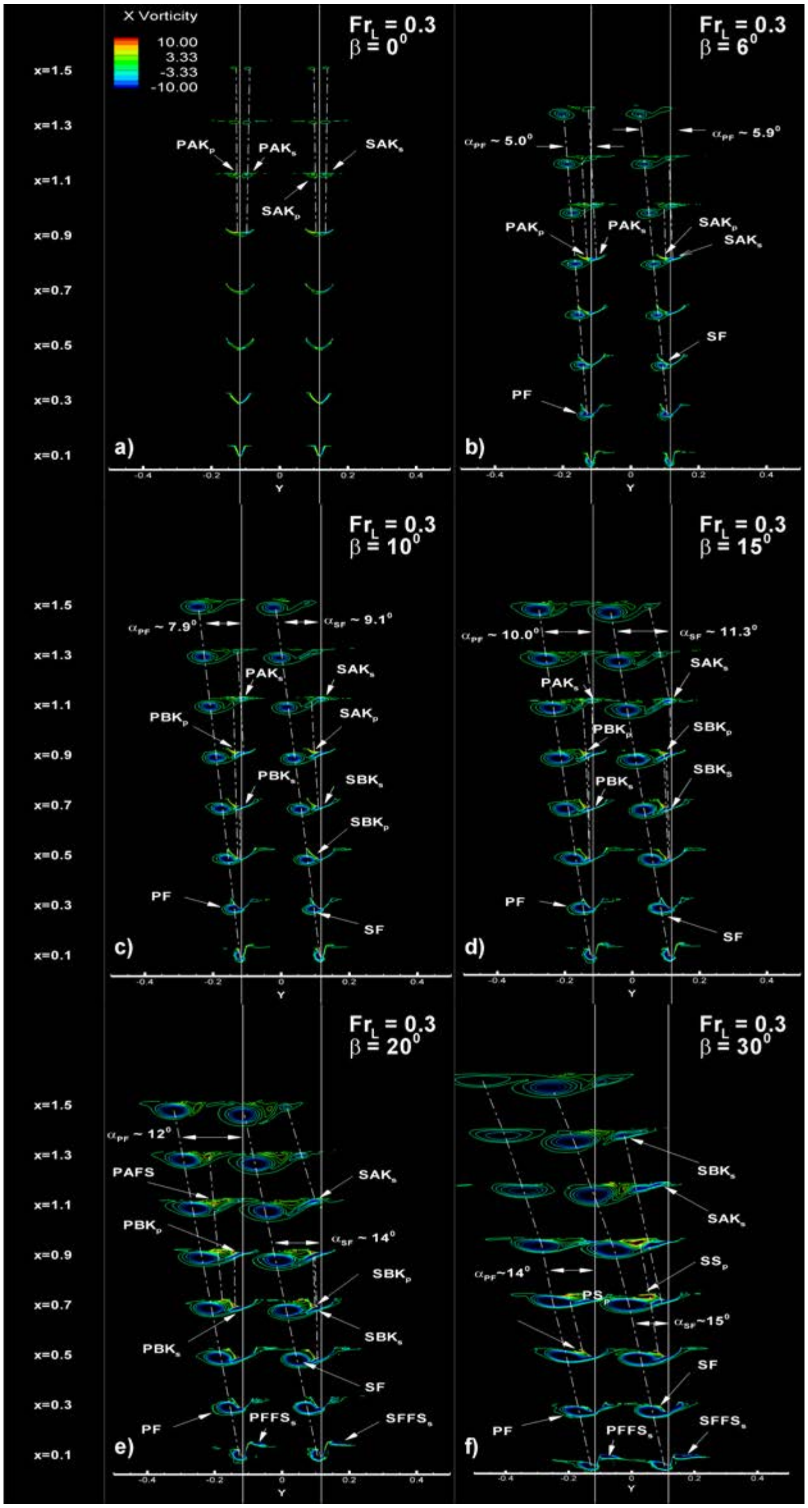

Figure 4.26: Vorticity plot at $Fr = 0.3$ and $0^0 \leq \beta \leq 30^0$ using GR

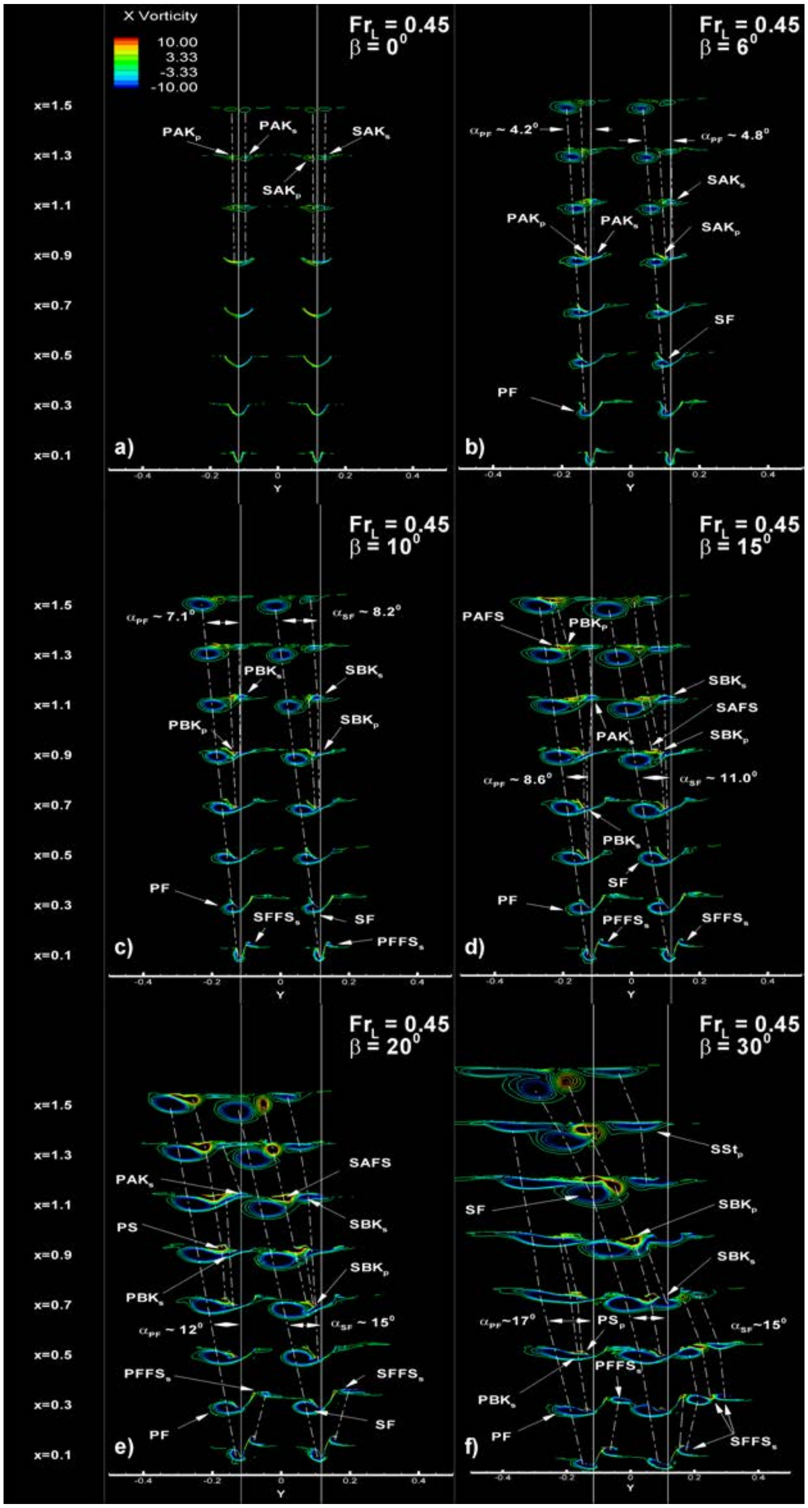

Figure 4.27: Vorticity plot at $Fr = 0.45$ and $0^0 \leq \beta \leq 30^0$ using GR

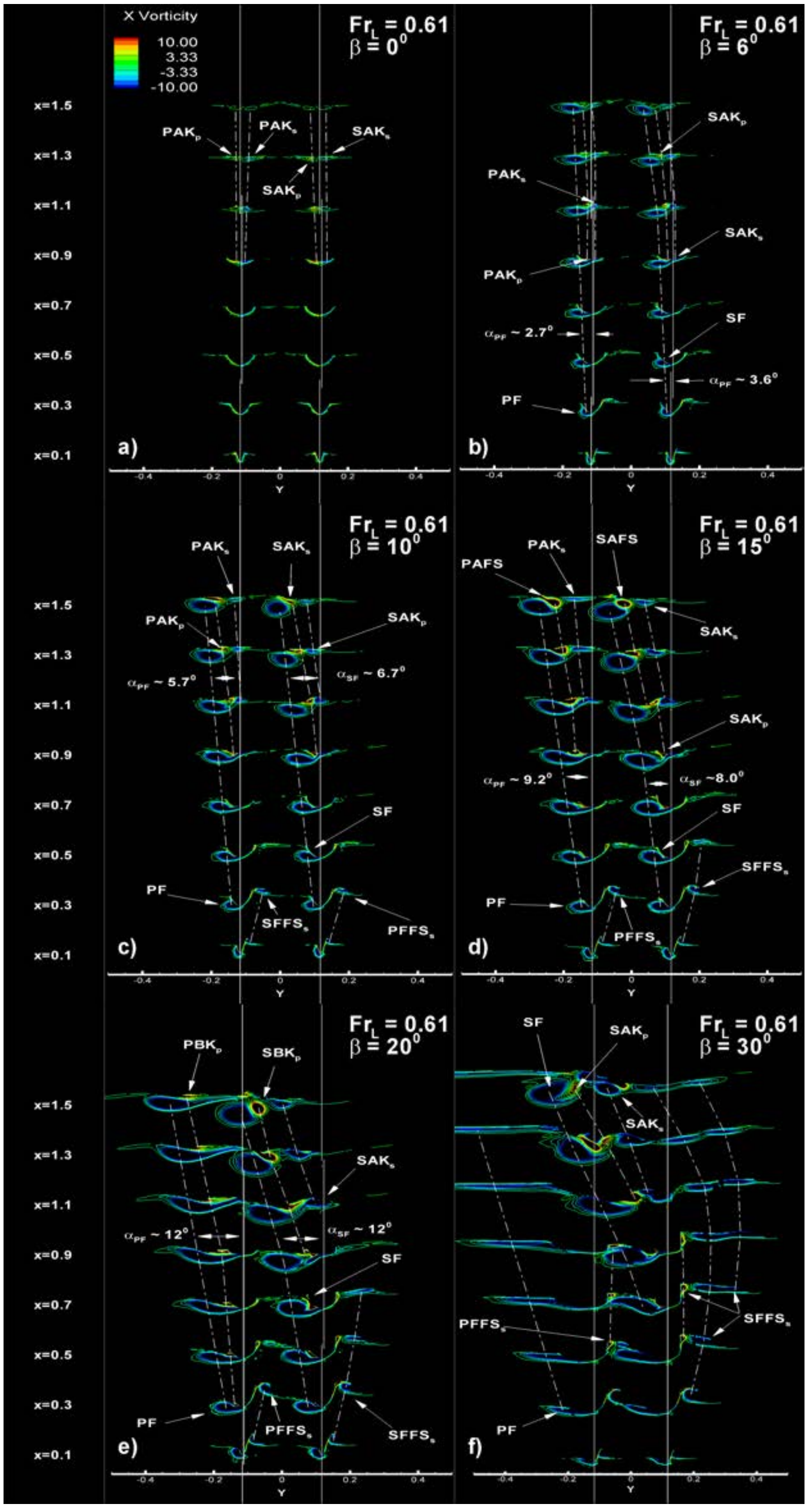

Figure 4.28: Vorticity plot at $Fr = 0.61$ and $0^0 \leq \beta \leq 30^0$ using GR

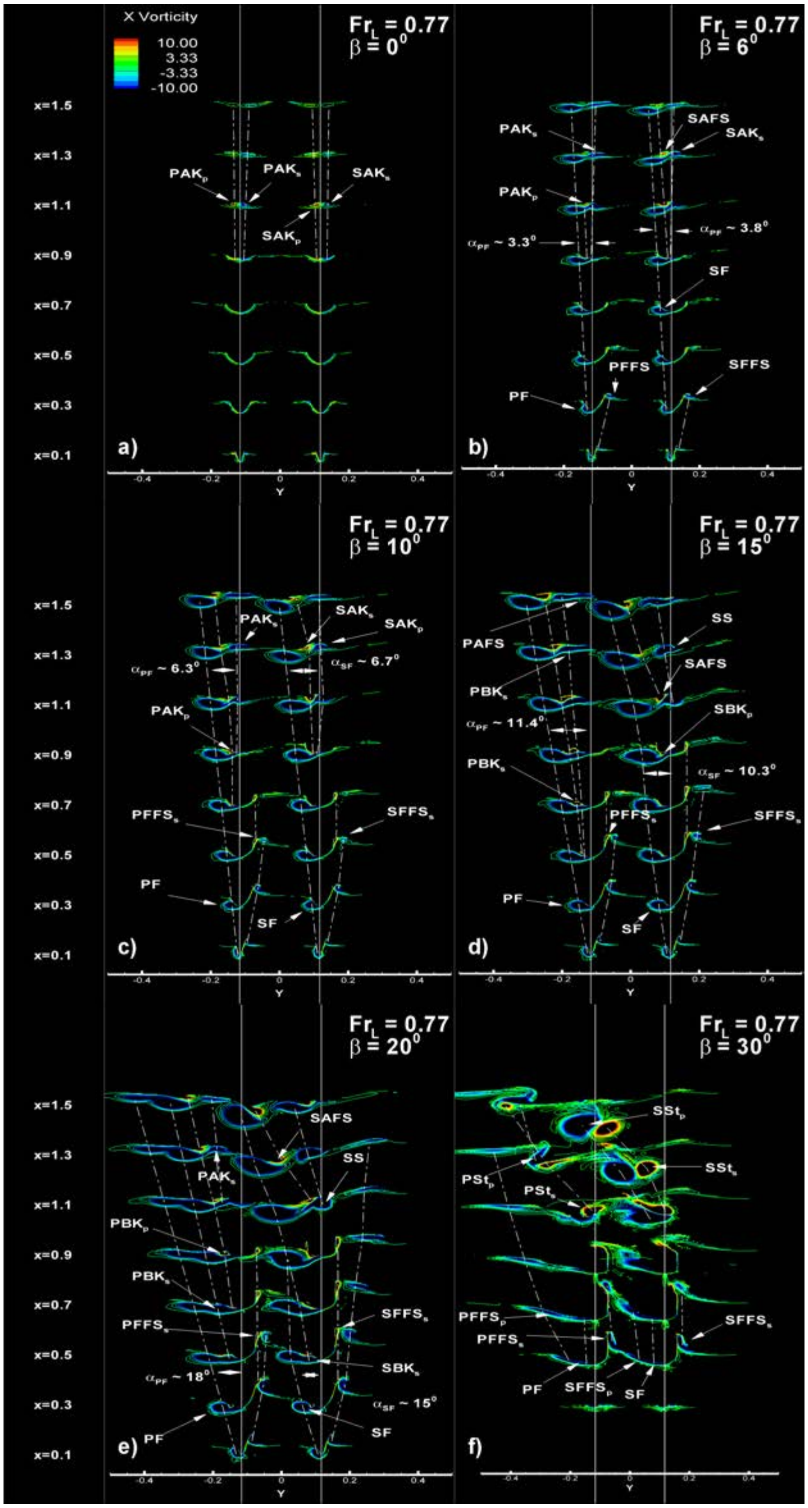

Figure 4.29: Vorticity plot at $Fr = 0.77$ and $0^0 \leq \beta \leq 30^0$ using GR

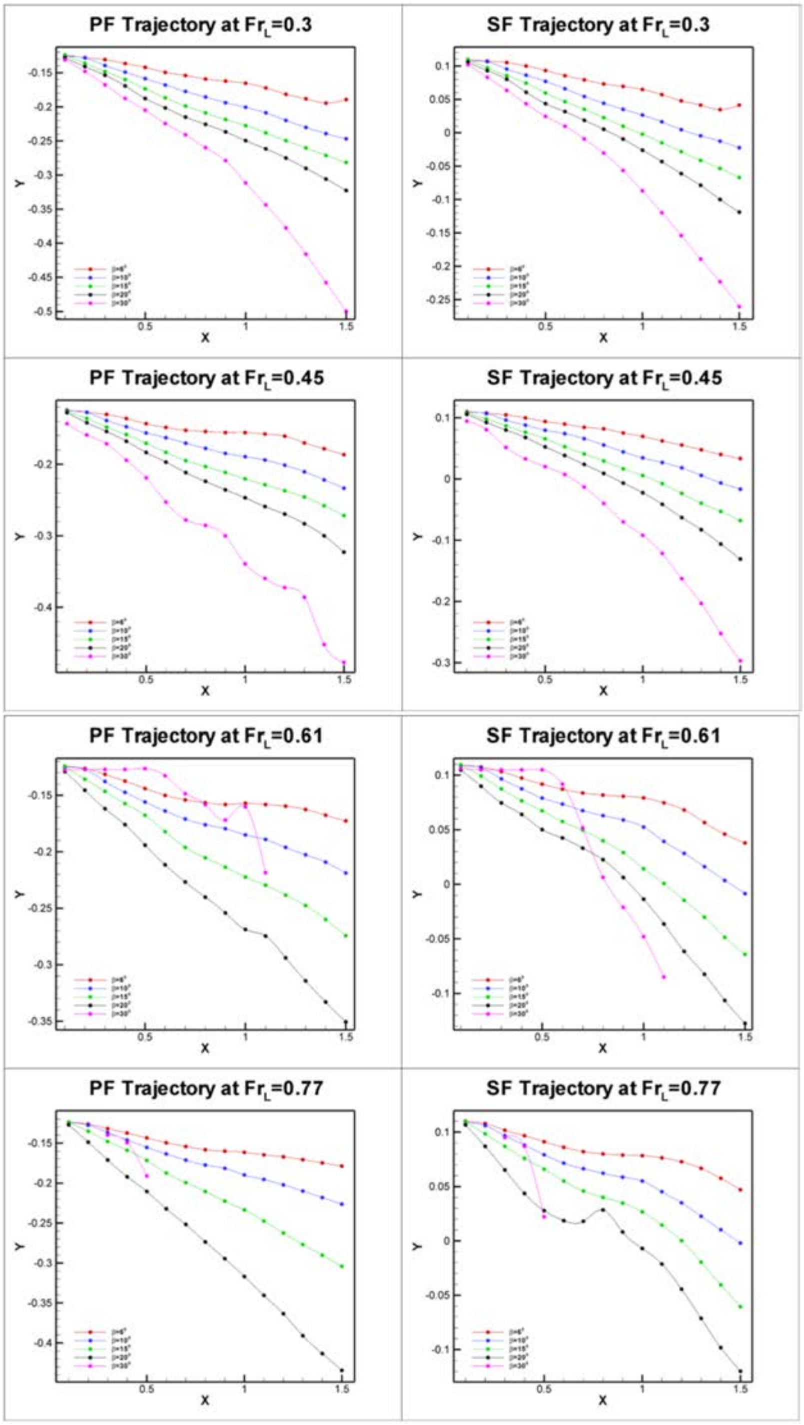

Figure 4.30: Comparison of vortex core trajectories at $0 \leq Frle0.77$ and $0^0 \leq \beta \leq 30^0$ using GR

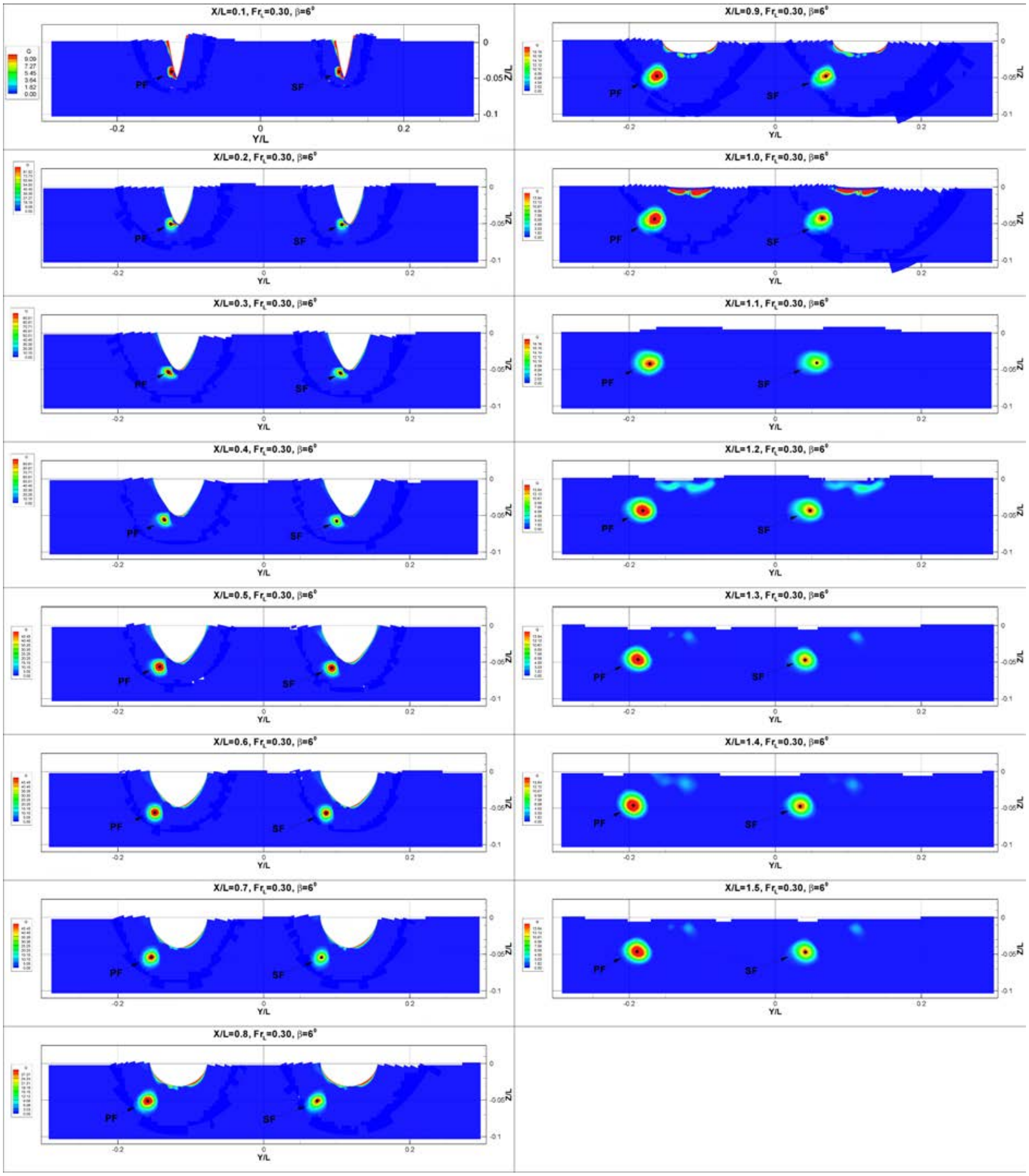

Figure 4.31: Q plots at $Fr = 0.3$ and $\beta = 6^0$ for GR

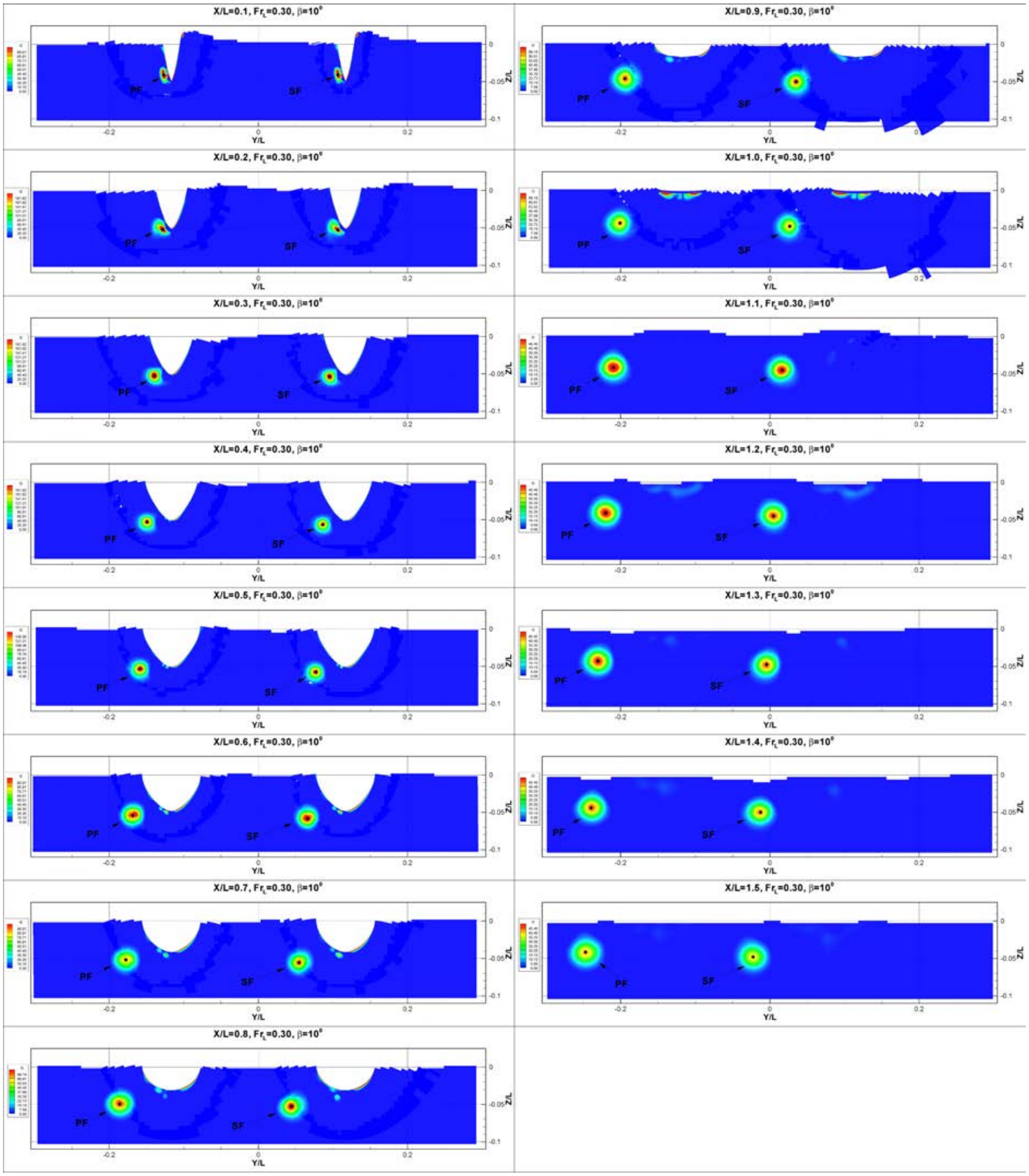

Figure 4.32: Q plots at $Fr = 0.3$ and $\beta = 10^0$ for GR

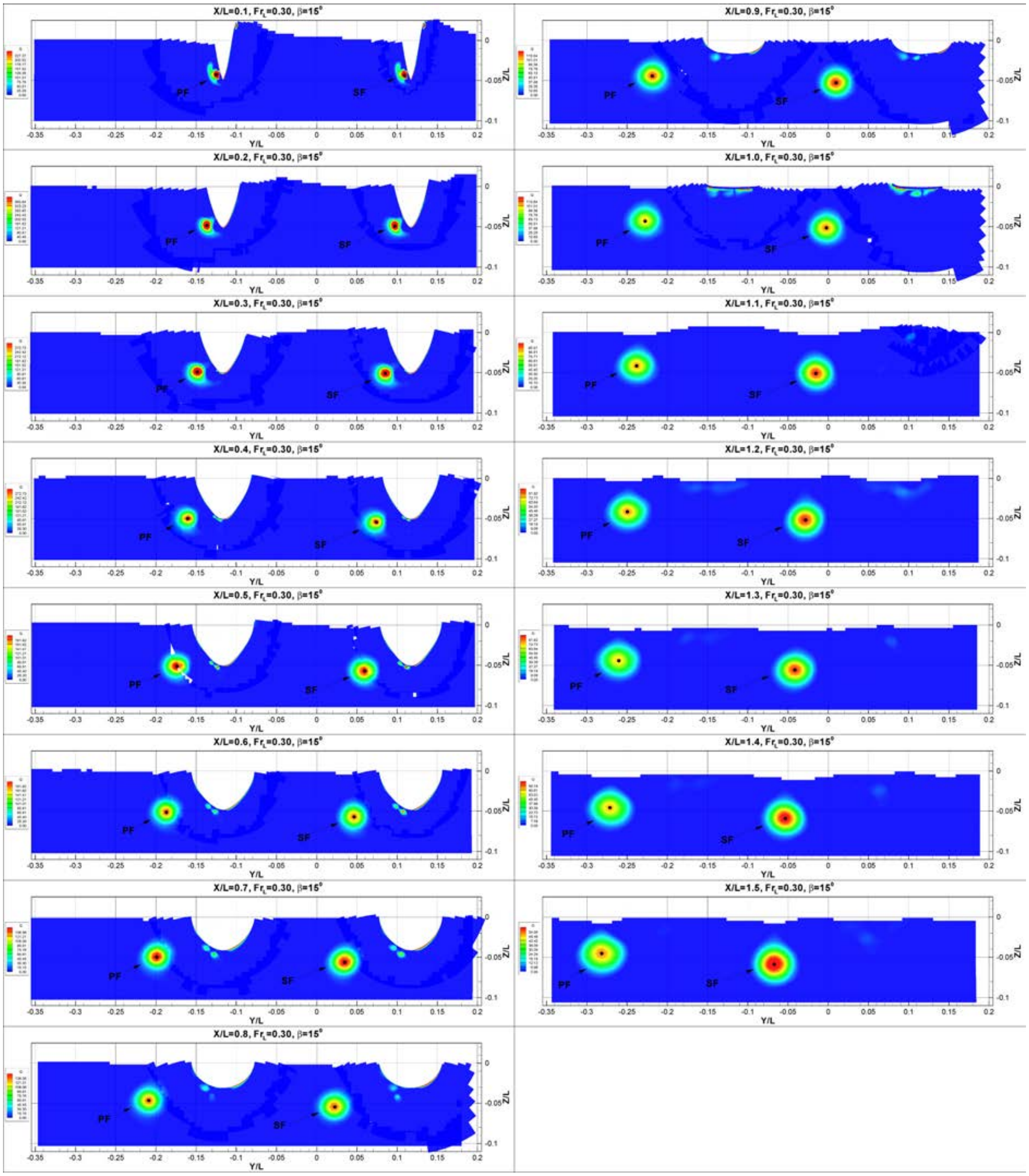

Figure 4.33: Q plots at $Fr = 0.3$ and $\beta = 15^0$ for GR

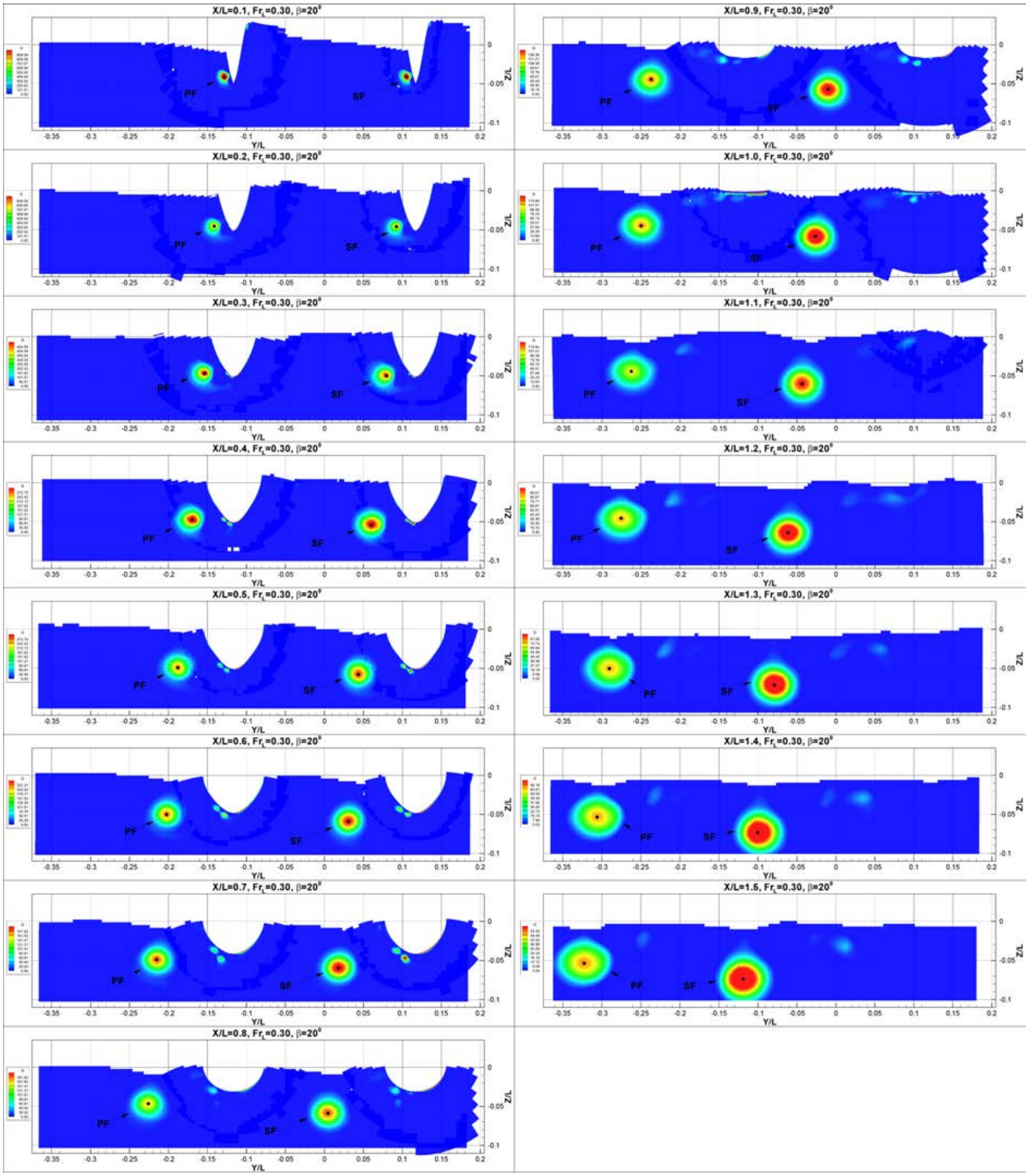

Figure 4.34: Q plots at $Fr = 0.3$ and $\beta = 20^0$ for GR

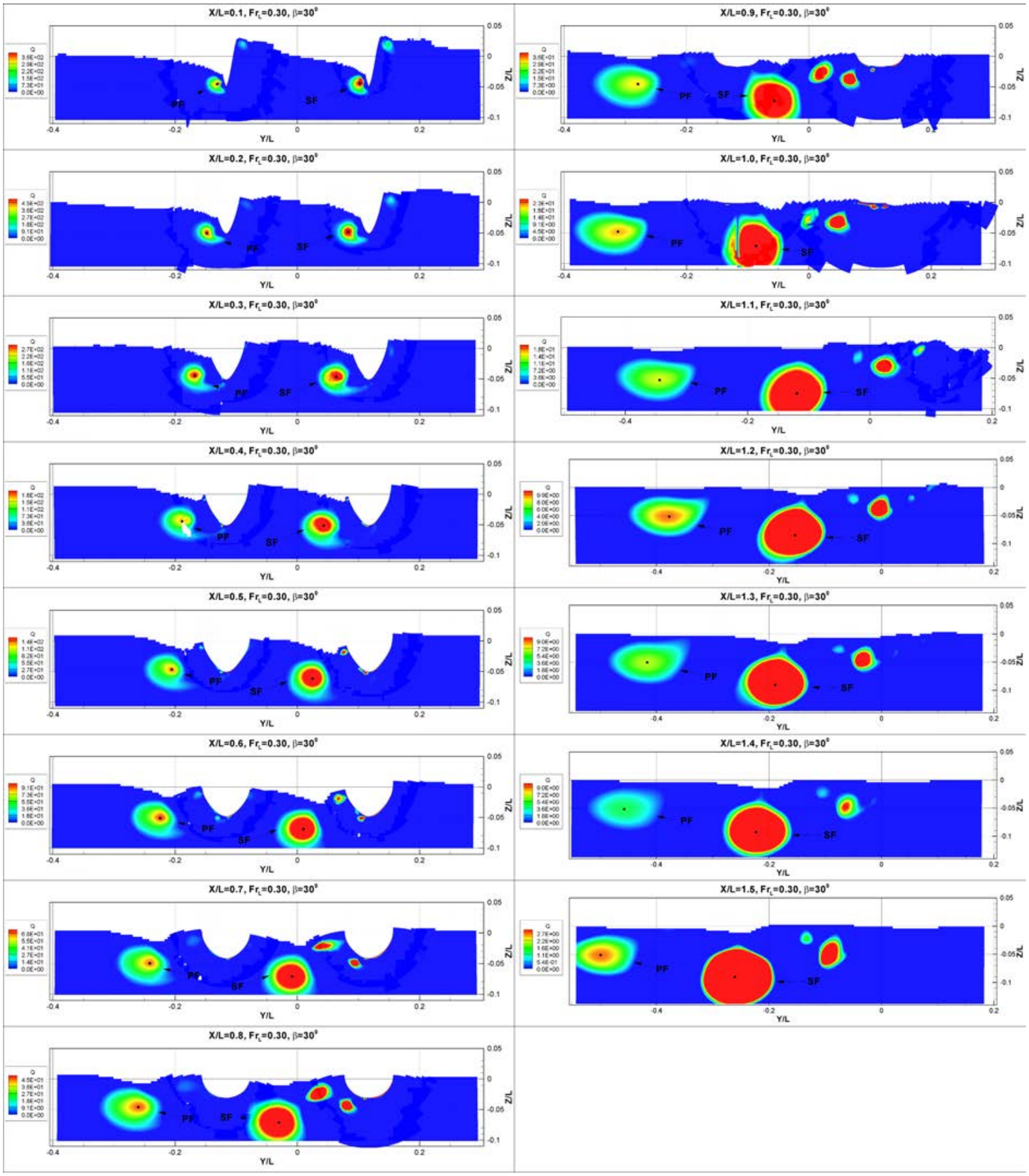

Figure 4.35: Q plots at $Fr = 0.3$ and $\beta = 30^0$ for GR

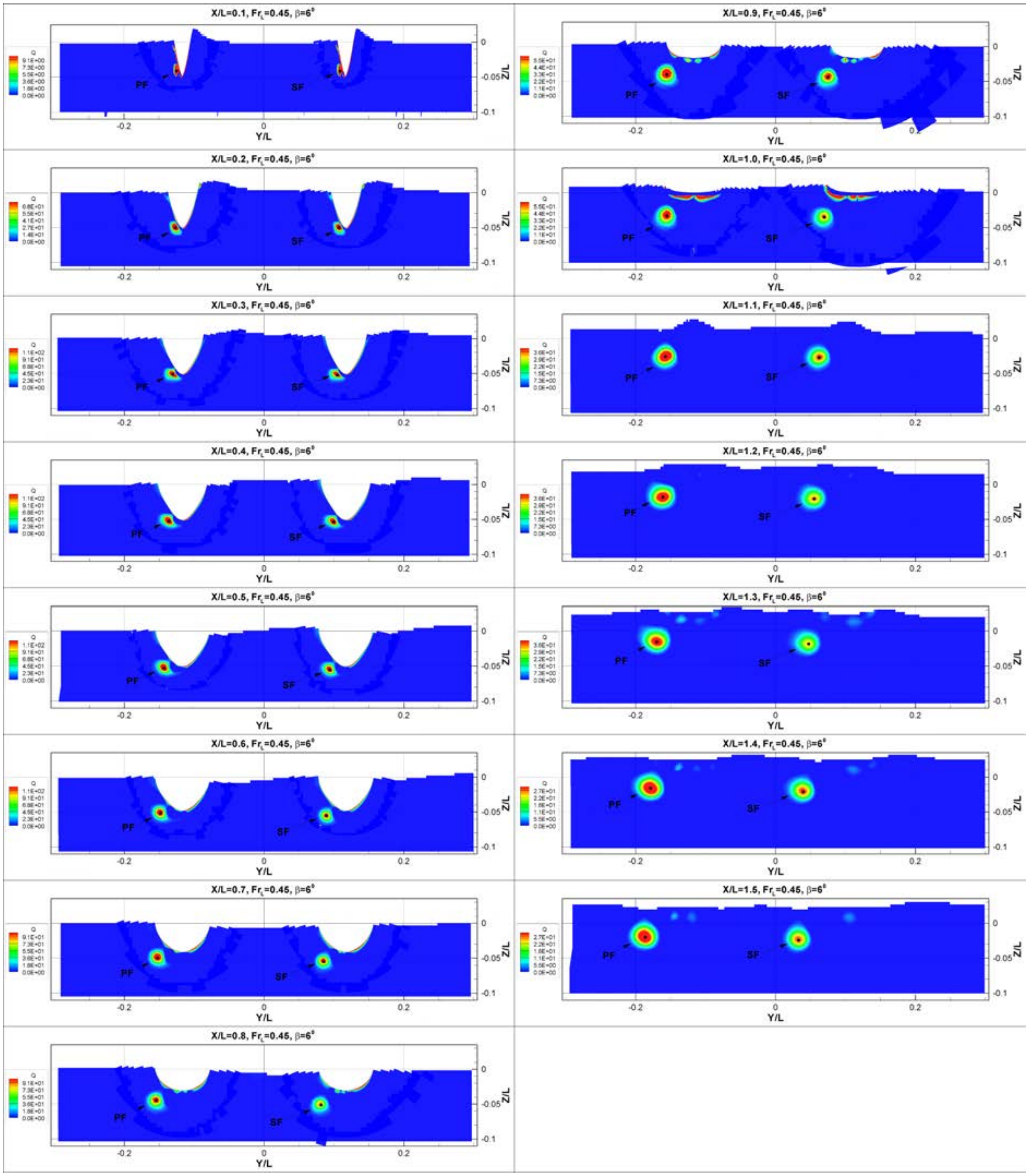

Figure 4.36: Q plots at $Fr = 0.45$ and $\beta = 6^0$ for GR

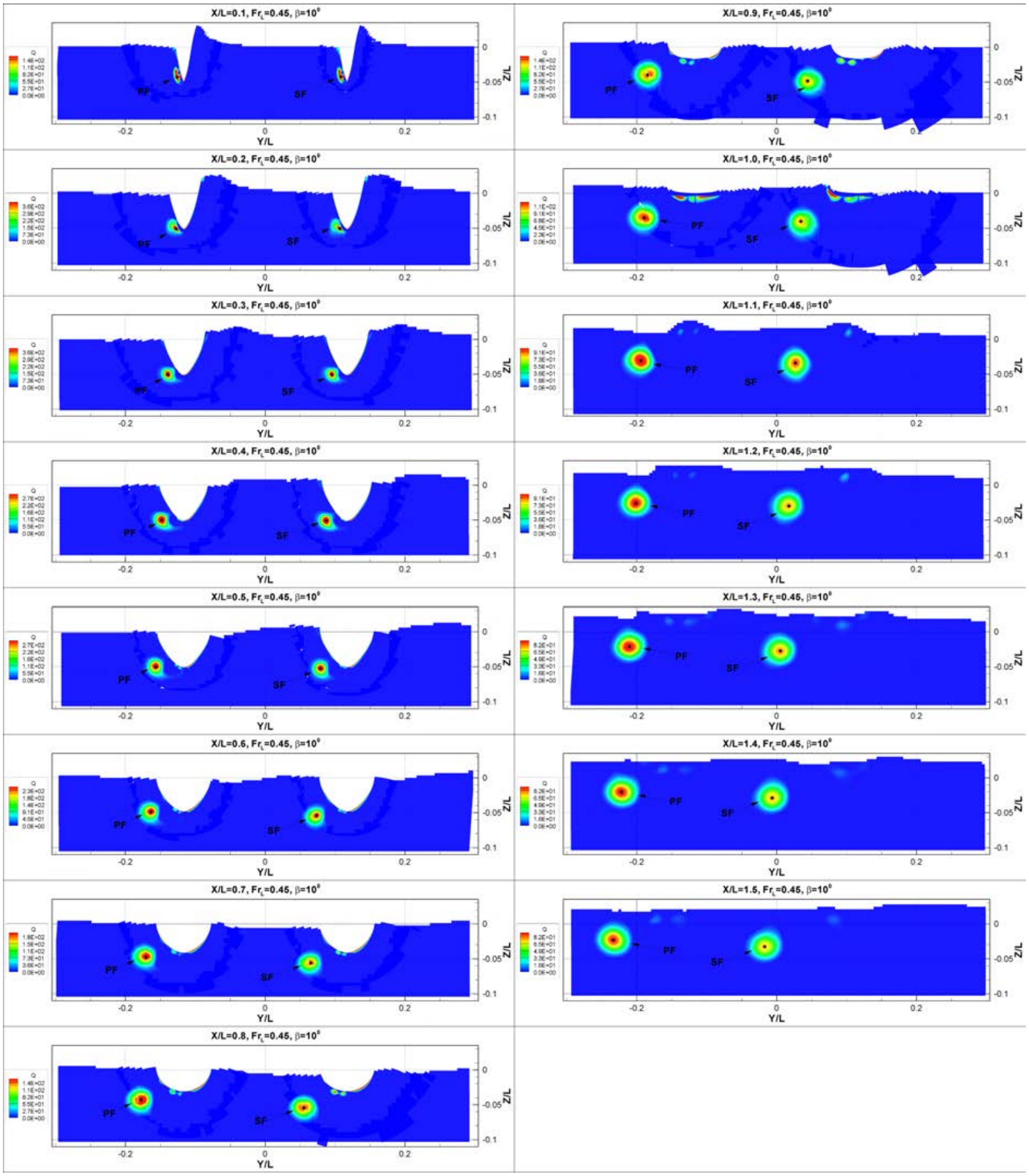

Figure 4.37: Q plots at $Fr = 0.45$ and $\beta = 10^0$ for GR

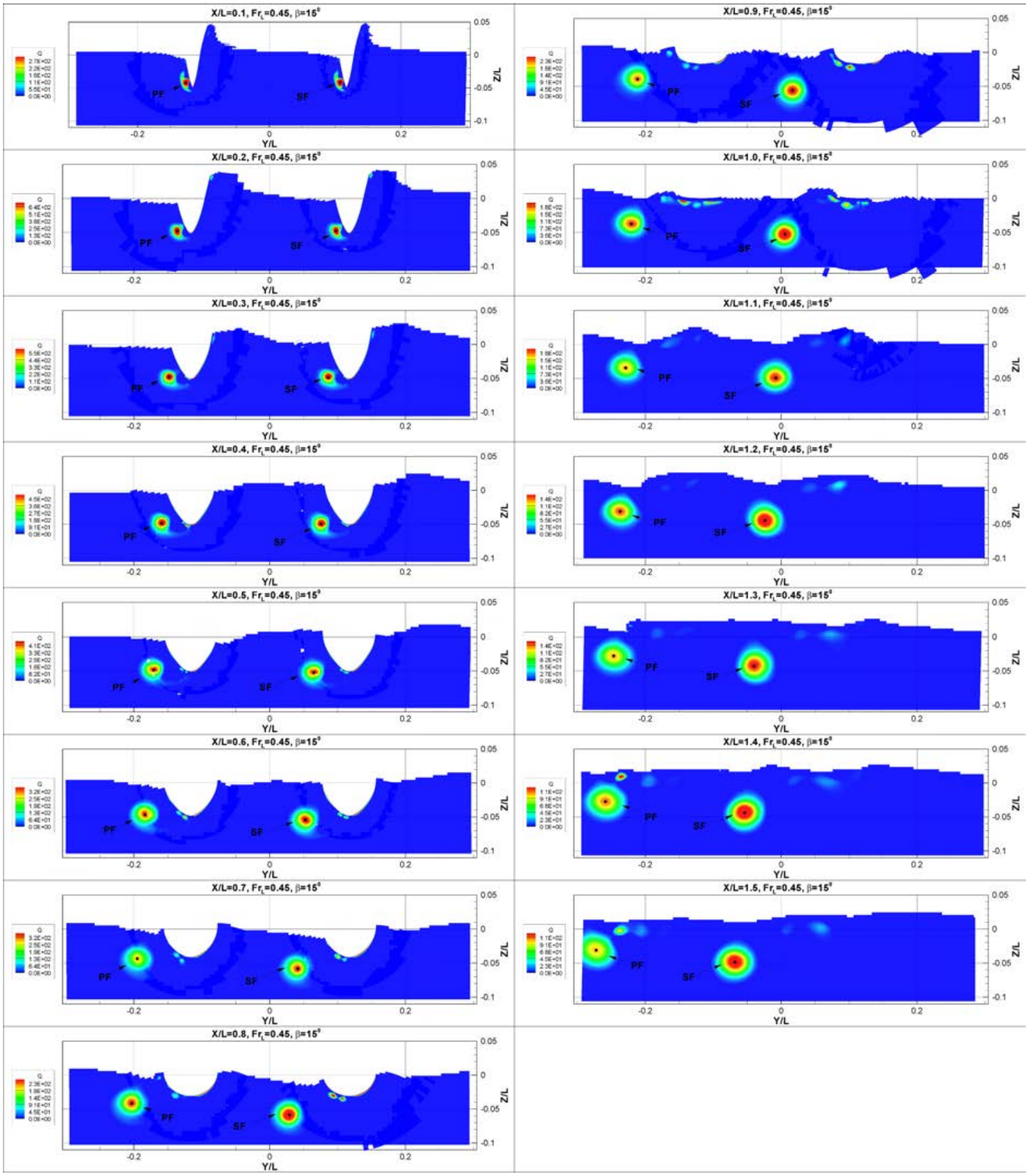

Figure 4.38: Q plots at $Fr = 0.45$ and $\beta = 15^0$ for GR

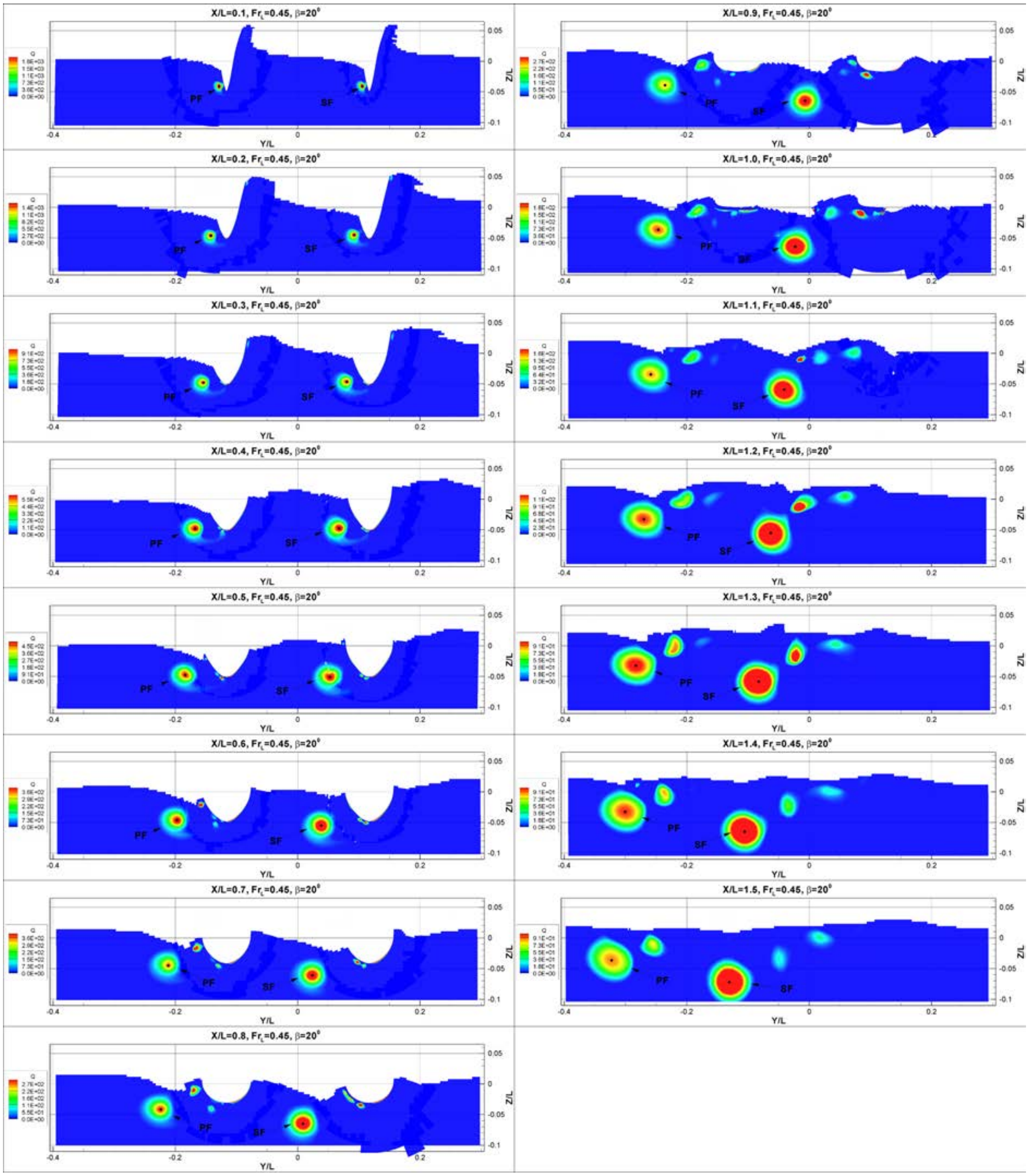

Figure 4.39: Q plots at $Fr = 0.45$ and $\beta = 20^0$ for GR

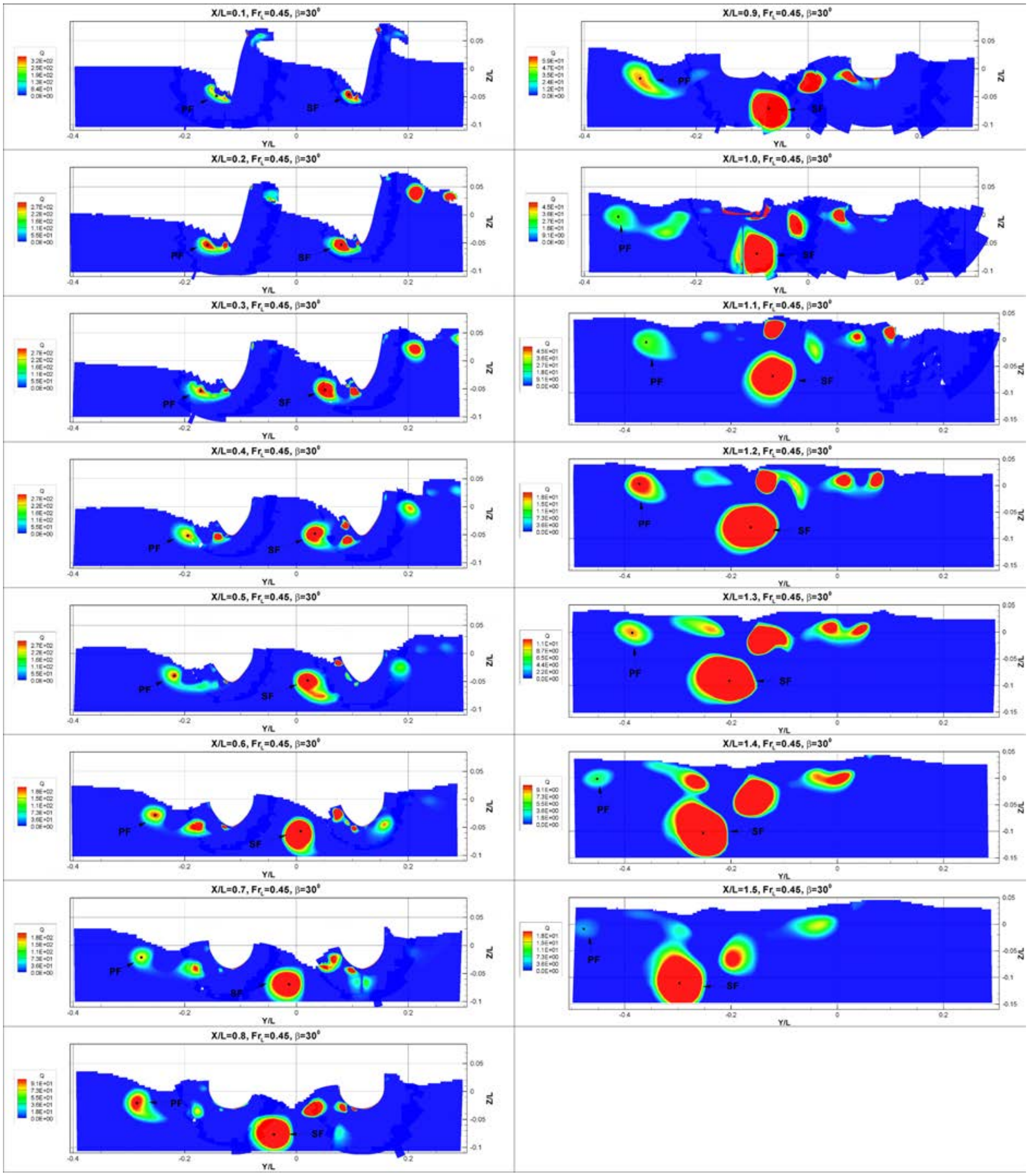

X/L=0.1, Fr_L=0.45, β=30°

X/L=0.2, Fr_L=0.45, β=30°

X/L=0.3, Fr_L=0.45, β=30°

X/L=0.4, Fr_L=0.45, β=30°

X/L=0.5, Fr_L=0.45, β=30°

X/L=0.6, Fr_L=0.45, β=30°

X/L=0.7, Fr_L=0.45, β=30°

X/L=0.8, Fr_L=0.45, β=30°

X/L=0.9, Fr_L=0.45, β=30°

X/L=1.0, Fr_L=0.45, β=30°

X/L=1.1, Fr_L=0.45, β=30°

X/L=1.2, Fr_L=0.45, β=30°

X/L=1.3, Fr_L=0.45, β=30°

X/L=1.4, Fr_L=0.45, β=30°

X/L=1.5, Fr_L=0.45, β=30°

Figure 4.40: Q plots at $Fr = 0.45$ and $\beta = 30^0$ for GR

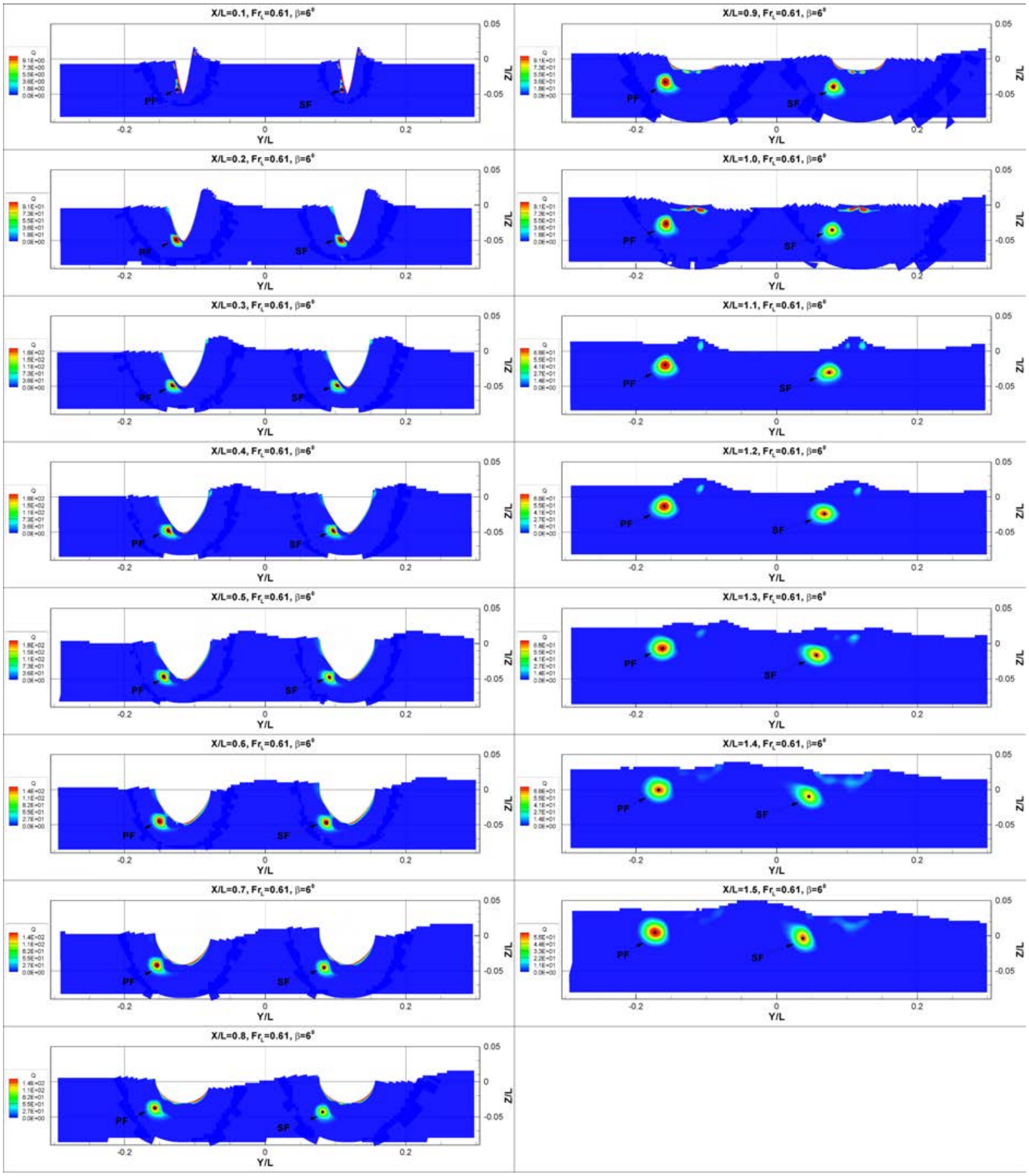

Figure 4.41: Q plots at $Fr = 0.61$ and $\beta = 6^0$ for GR

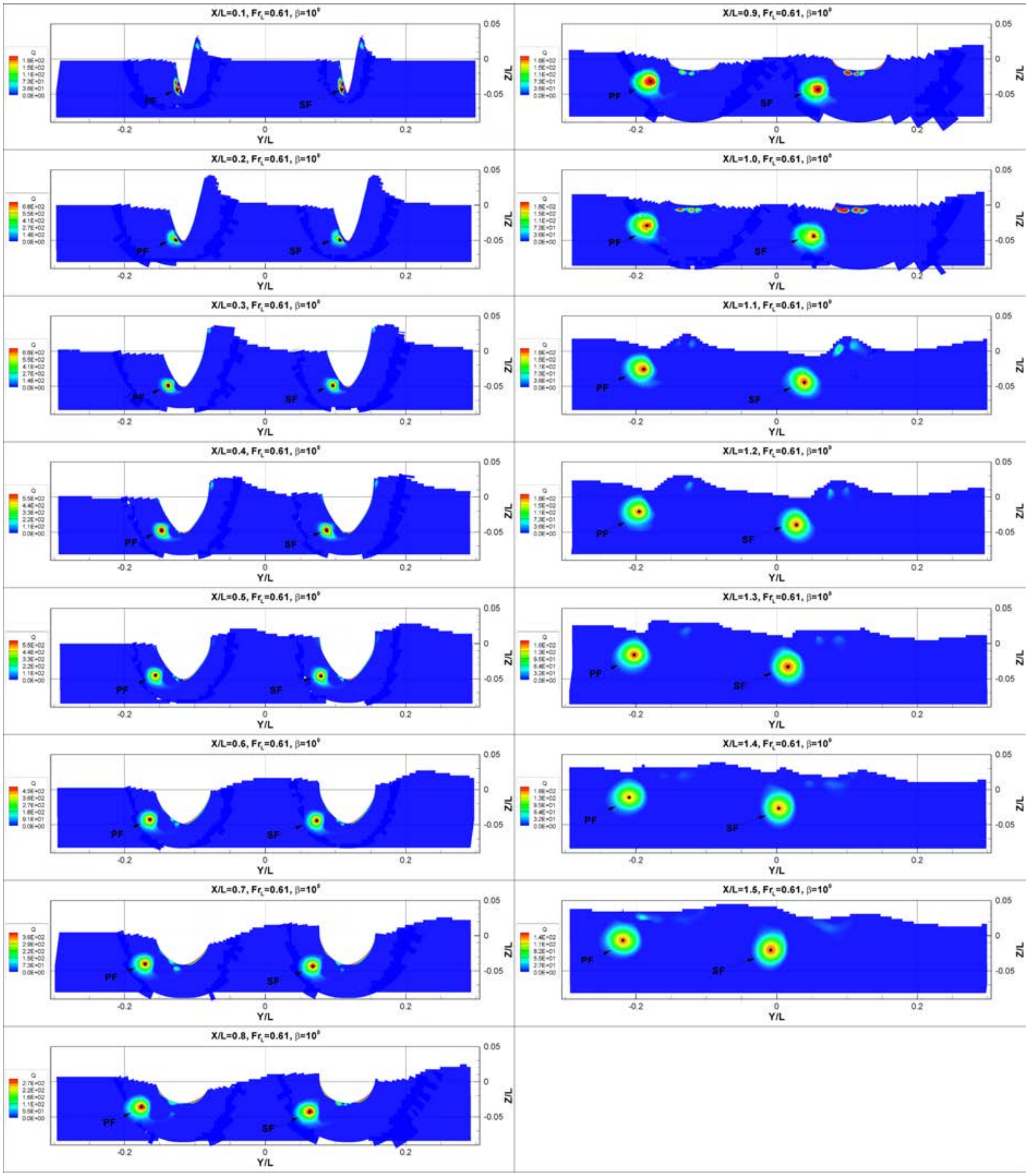

Figure 4.42: Q plots at $Fr = 0.61$ and $\beta = 10^0$ for GR

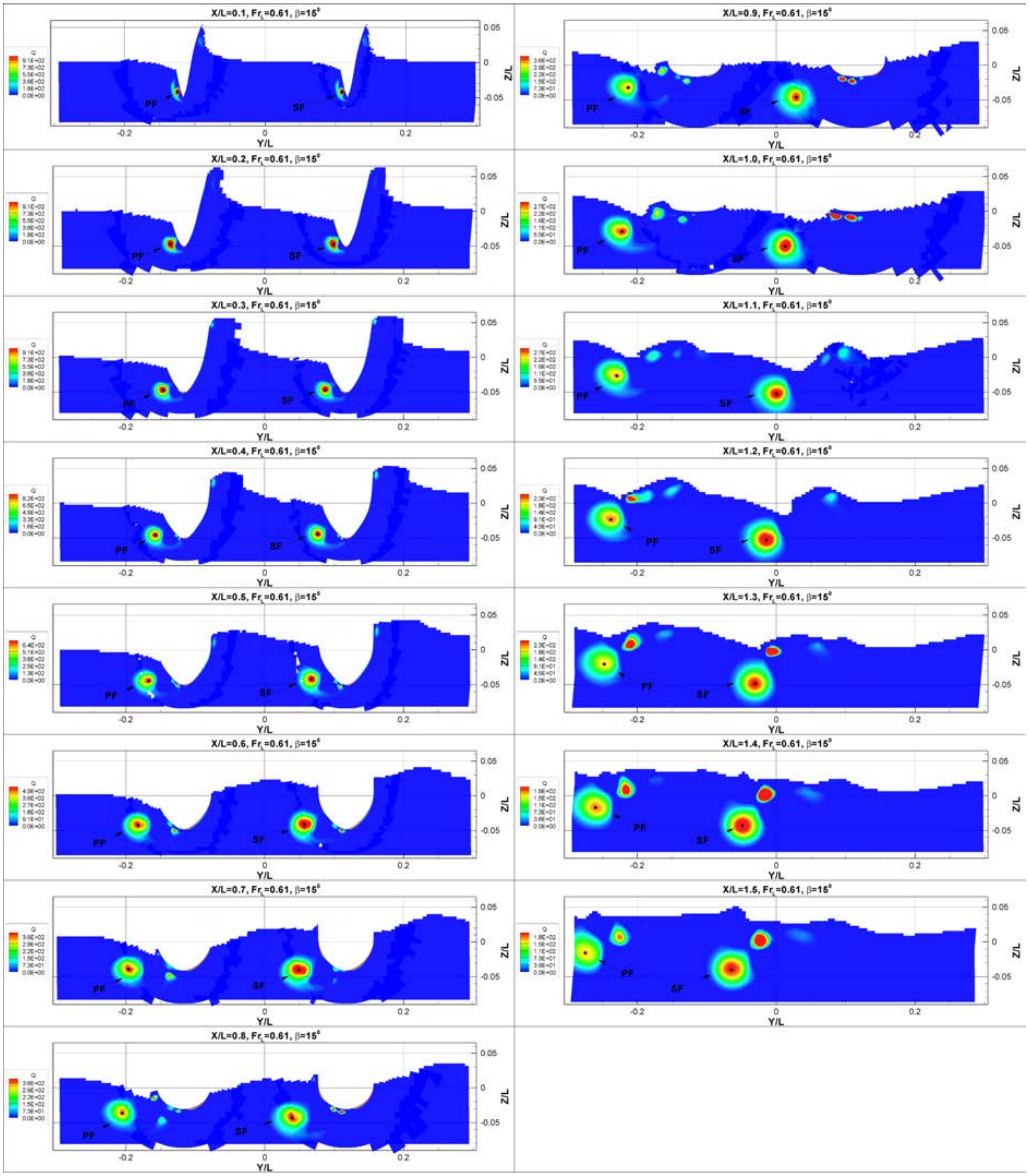

Figure 4.43: Q plots at $Fr = 0.61$ and $\beta = 15^0$ for GR

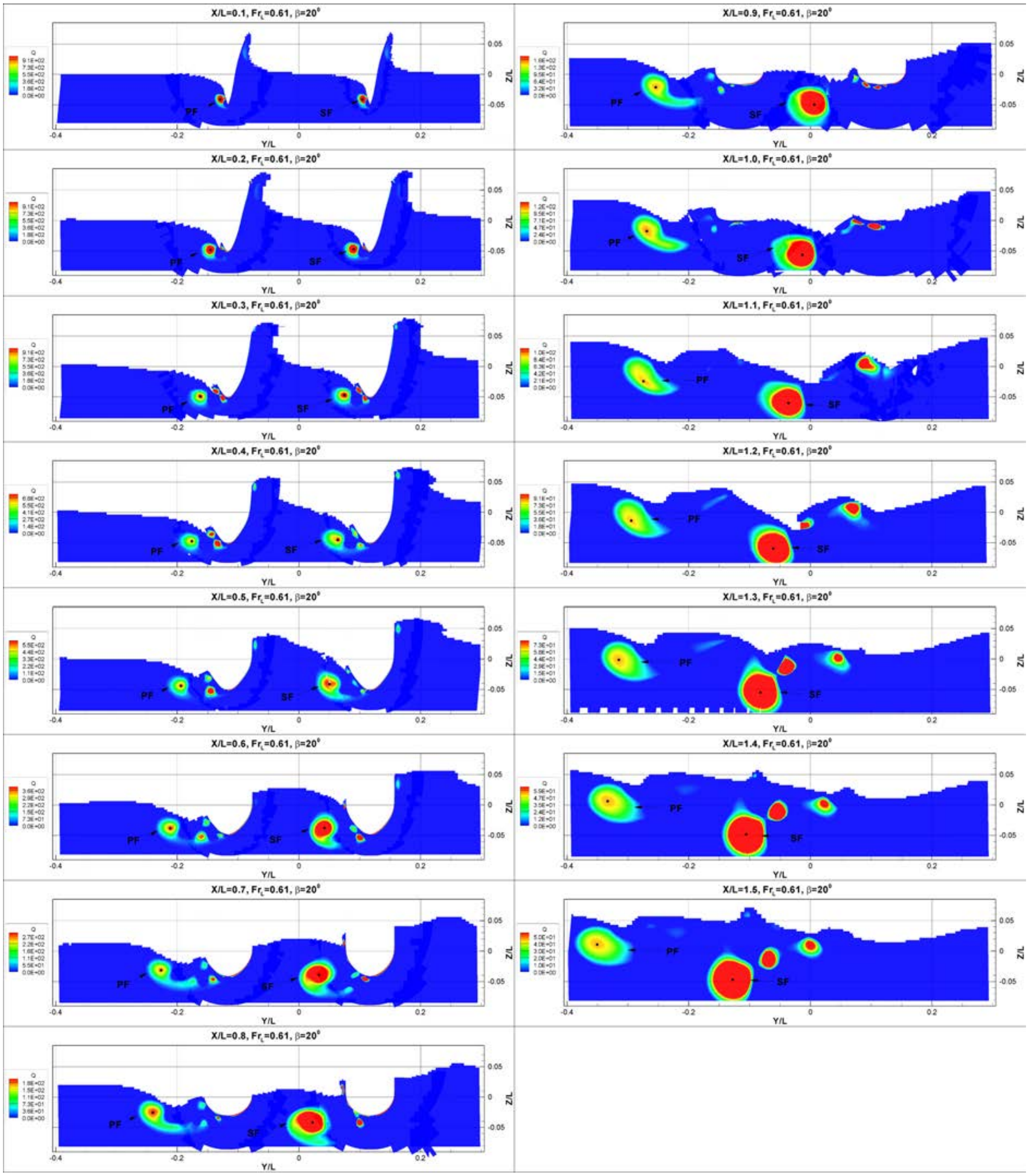

Figure 4.44: Q plots at $Fr = 0.61$ and $\beta = 20^0$ for GR

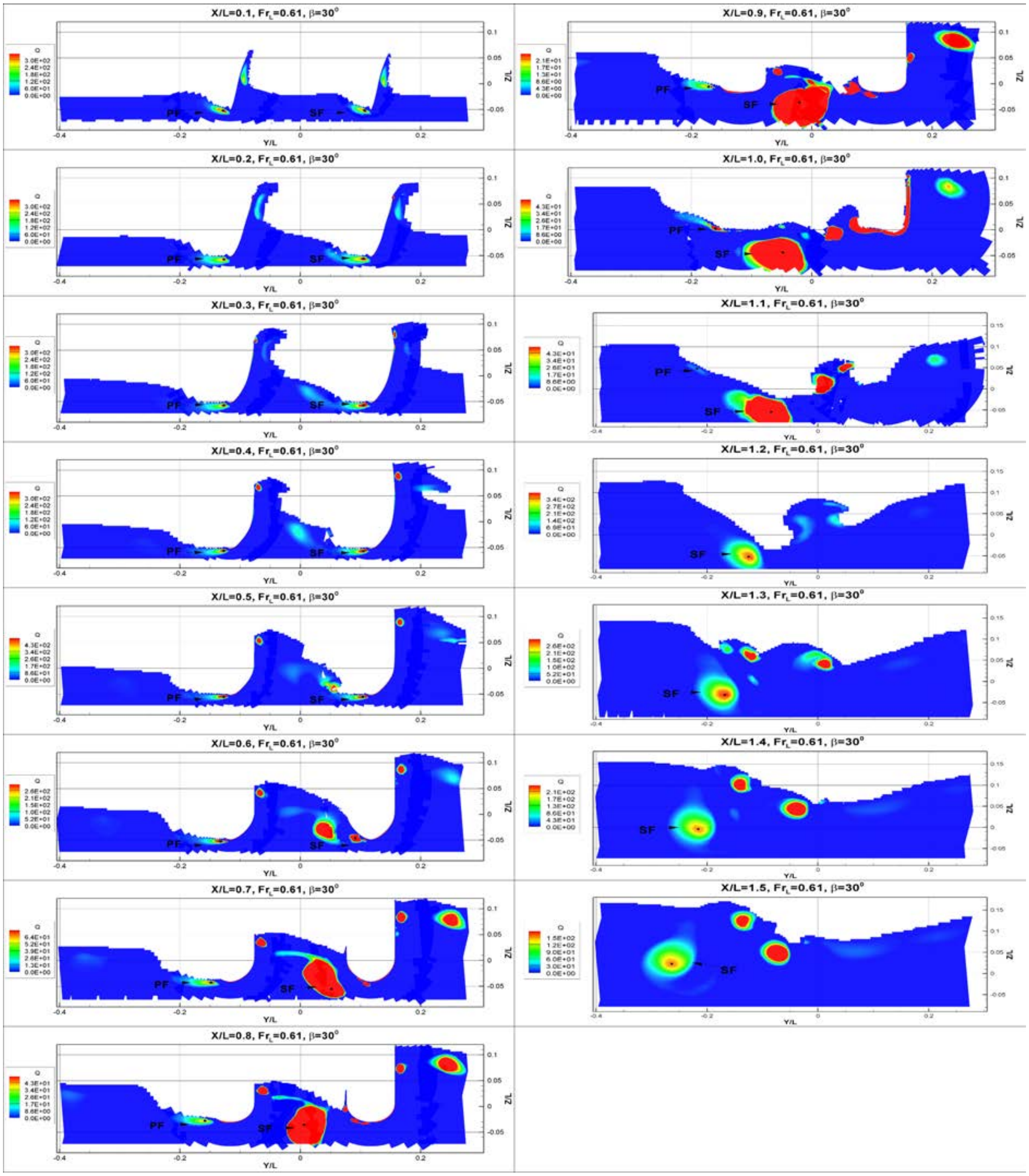

Figure 4.45: Q plots at $Fr = 0.61$ and $\beta = 30^0$ for GR

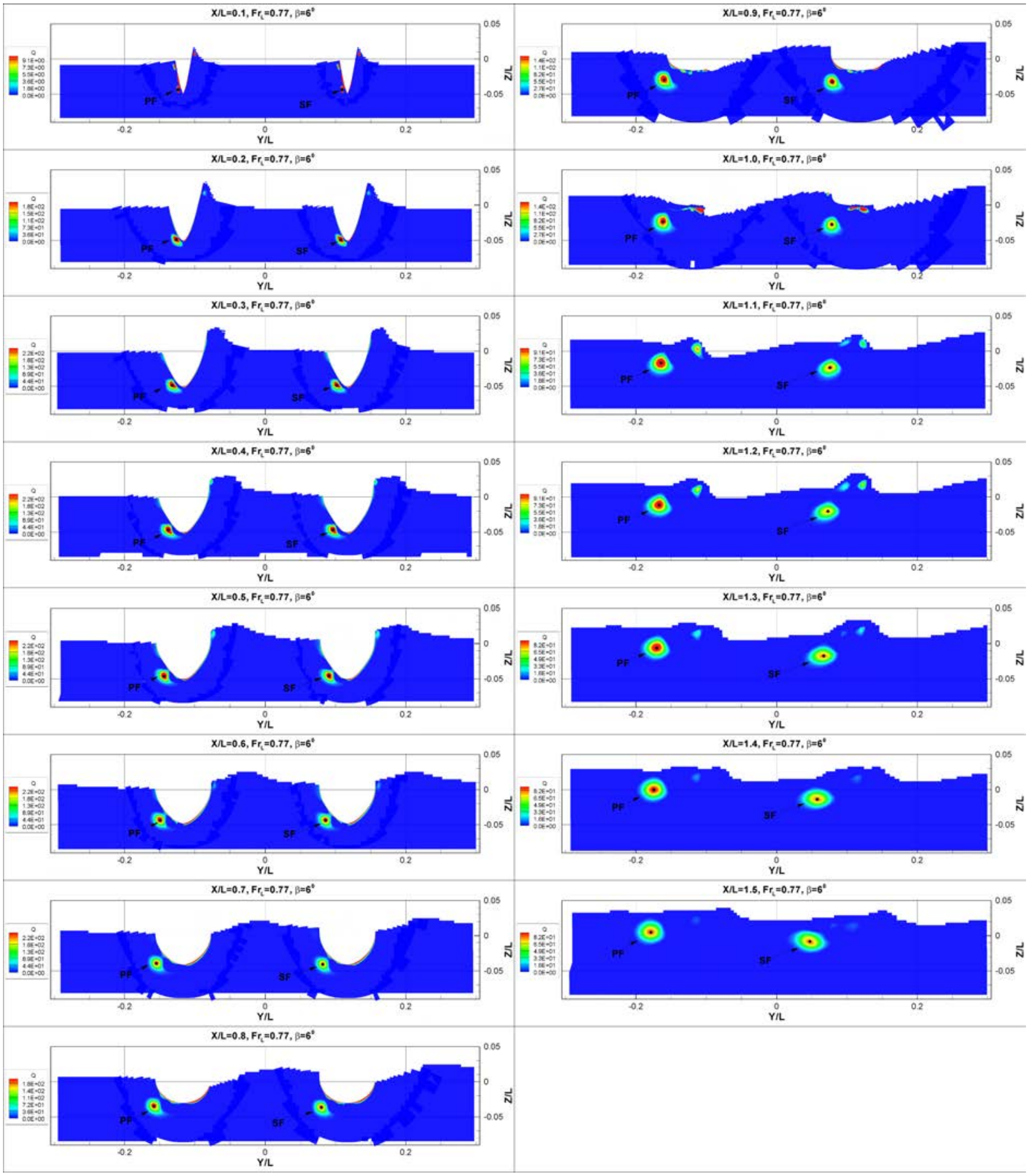

Figure 4.46: Q plots at $Fr = 0.77$ and $\beta = 6^0$ for GR

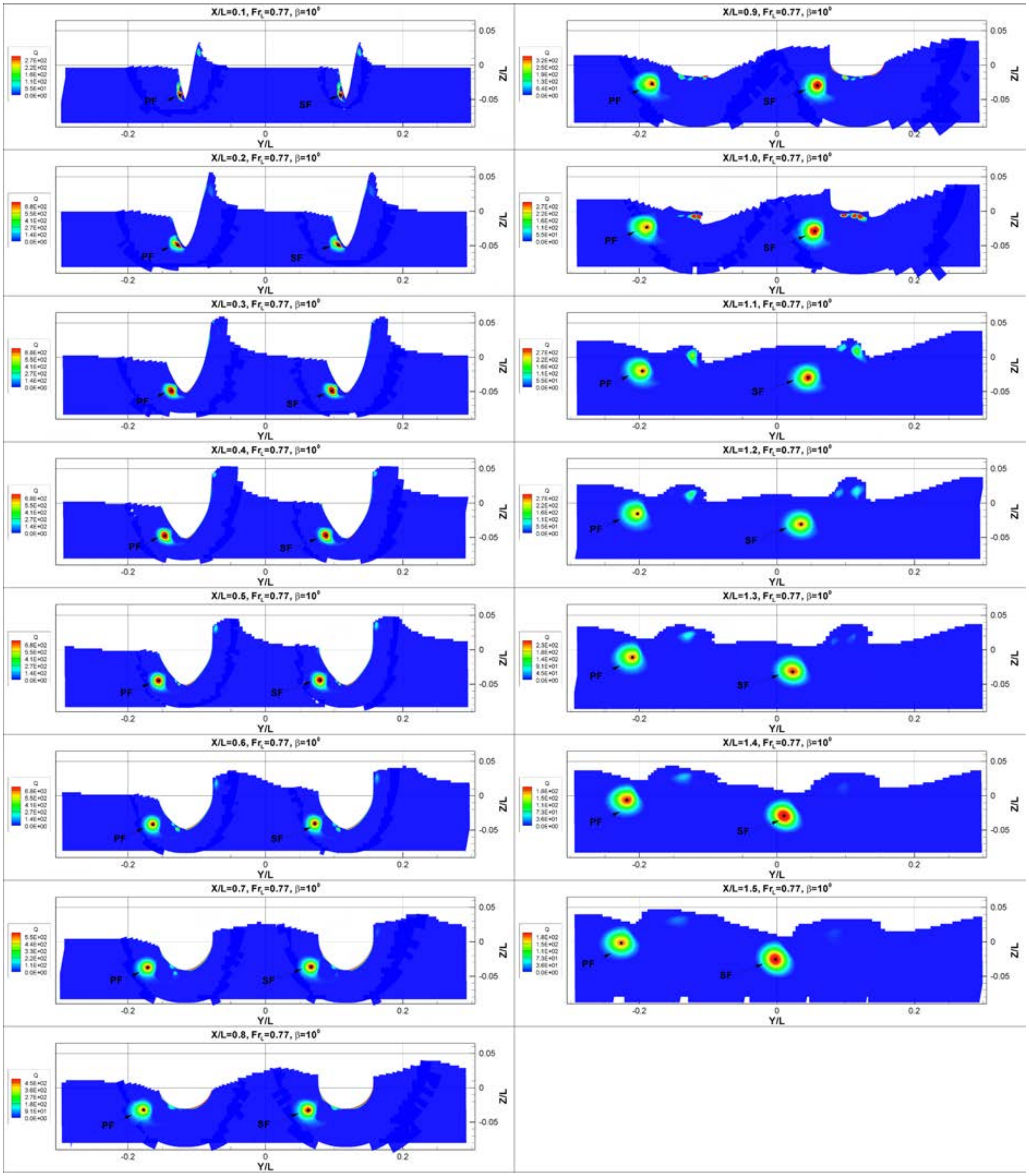

Figure 4.47: Q plots at $Fr = 0.77$ and $\beta = 10^0$ for GR

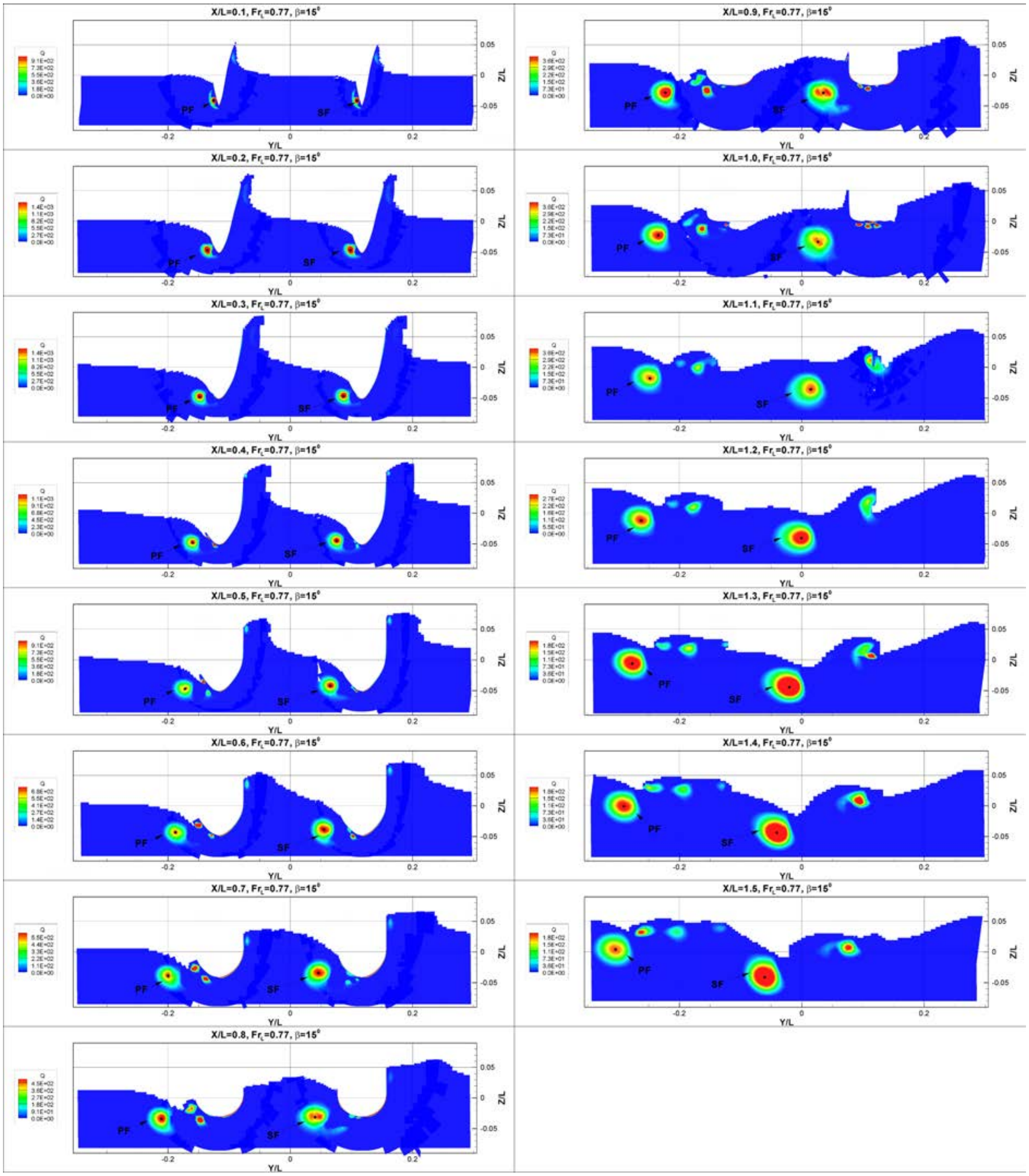
$X/L=0.1$, $Fr_L=0.77$, $\beta=15^0$

$X/L=0.2$, $Fr_L=0.77$, $\beta=15^0$

$X/L=0.3$, $Fr_L=0.77$, $\beta=15^0$

$X/L=0.4$, $Fr_L=0.77$, $\beta=15^0$

$X/L=0.5$, $Fr_L=0.77$, $\beta=15^0$

$X/L=0.6$, $Fr_L=0.77$, $\beta=15^0$

$X/L=0.7$, $Fr_L=0.77$, $\beta=15^0$

$X/L=0.8$, $Fr_L=0.77$, $\beta=15^0$

$X/L=0.9$, $Fr_L=0.77$, $\beta=15^0$

$X/L=1.0$, $Fr_L=0.77$, $\beta=15^0$

$X/L=1.1$, $Fr_L=0.77$, $\beta=15^0$

$X/L=1.2$, $Fr_L=0.77$, $\beta=15^0$

$X/L=1.3$, $Fr_L=0.77$, $\beta=15^0$

$X/L=1.4$, $Fr_L=0.77$, $\beta=15^0$

$X/L=1.5$, $Fr_L=0.77$, $\beta=15^0$

Figure 4.48: Q plots at $Fr = 0.77$ and $\beta = 15^0$ for GR

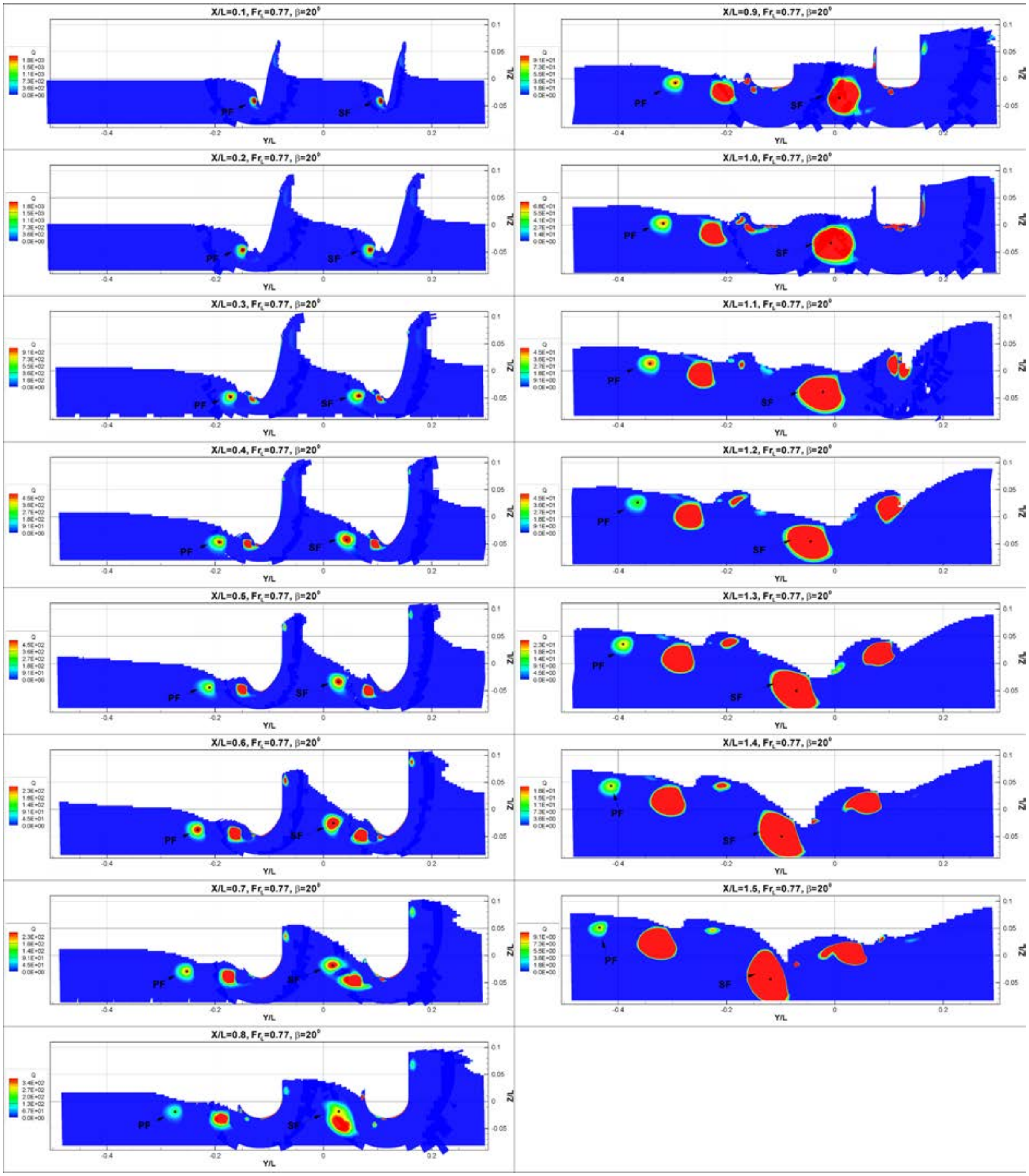

Figure 4.49: Q plots at $Fr = 0.77$ and $\beta = 20^0$ for GR

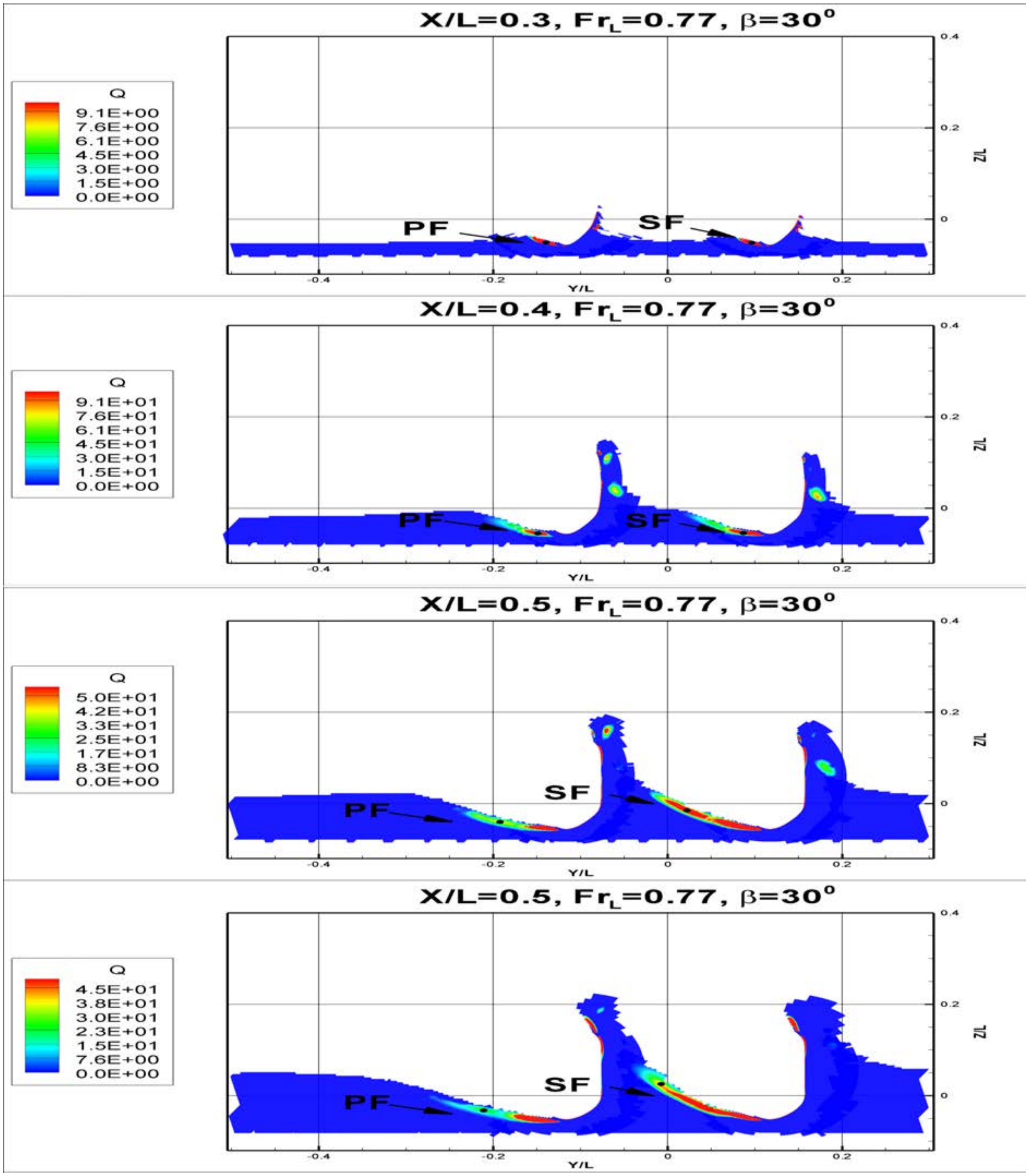

Figure 4.50: Q plots at $Fr = 0.77$ and $\beta = 30^0$ for GR

CHAPTER 5
URANS AND DES RESULTS USING G2,G3,G4, AND G5 GRIDS

Two verification studies were conducted using DES and URANS. Local mean velocity components and x-vorticity were validated for CFD using DES with $\beta = 6^0, 9^0$ and $Fr = 0.4, 0.5$. The catamran was fixed at the same position as the SPIV experiments for local mean component validation. Additionally, integral variables and the wave elevations were validated at $\beta = 24^0$ and $Fr = 0.3$ where ship was free to sink and trim. Although LES was activated at the vortex region as shown in Figures 5.1-5.3, turbulence was not resolved for the cases where ship was fixed. The resolved turbulence was 66% for $Fr = 0.3$ and $\beta = 24^0$ case where most of the turbulence was resolved at the wake of the catamaran (Figure 5.4). The flow was steady for all cases except $Fr = 0.3$ and $\beta = 24$ using G3 (Figures 5.5-5.10.

5.1 Verification of Integral Variables

Verification study of the integral variables using DES model with two triplets of G5-G4-G3 and G4-G3-G2 was performed at $\beta = 6^0$, $Fr = 0.5$ and even keel condition (Table 5.1). Convergence was achieved for Xf, N, Nf, Np for triplet of G4-G3-G2 and X, Y, Yf, Yp for triplet G5-G4-G3. Most of the convergence achieved was oscillatory convergence. The LES activation region increased with increasing grid size as seen in Figures 5.1-5.3. The verification method does not account for the use of different models at different regions which could explain the poor verification results. Another verification study was performed using URANS model with triplet G5-G4-

G3 at $\beta = 24^0$ and $Fr = 0.3$ (Table 5.2). Monotonic convergence was achieved for all the principle variables with the exception of sink. However, large uncertainty was observed for x-force. This could be due to the fact that the flow was unsteady for G3 while it was steady for G4 and G5.

5.2 Validation of Integral and Local Variables

Validation study using both DES and URANS for the forces showed good agreement between EFD and CFD while larger errors were observed for the moment and motions (Table 5.3). Additionally, the difference of forces between the demihulls were underpredicted. These results are consistent with the previous results obtained using GR grids. DES improve the force prediction while the moment and motion prediction worsened. Difference in the vortical structures are observed for URANS and DES as shown in Figure 5.11.

Validation of local mean velocity and vorticity have been shown in Figures 5.12-5.20. Two large vorticies PF and SF have been validated with SPIV measurements. However, the location of the SPIV measurements were not appropriate to validate other vorticies observed in the CFD. Excellent agreement between EFD and CFD was achieved for the local mean velocity and vorticity for all the SPIV planes and experimental conditions (Table 5.4). Comparison of wave elevetion between EFD and CFD are shown in Figure 5.22 at $Fr = 0.3$ and $\beta = 24^0$. Similar wave patterns were observed for both EFD and CFD (Figure 5.22). TKE results at the same location as PIV were also shown in Figures 5.23-5.27.

5.3 Onset and Vortex Progression Analysis

Similar vortical structures and surface streamlines were observed for the fixed cases with $Fr = 0.4, 0.5$ and $\beta = 6^0, 9^0$ (Figures 5.28-5.42). Therefore, only detailed onset and vortical analysis were performed for $Fr = 0.5$ and $\beta = 9^0$ (Figures 5.43-5.46). Low surface pressure region was observed due to the large fore-body vortex. Convergence streamlines were followed by series of sink and saddles consequently followed by converging streamlines again on the hull surface along the fore-body vortex. Hence an open-closed type instability for the fore-body vorticies was found. Additionally, vortex progression and onset analysis were conducted for $Fr = 0.3$ and $\beta = 24^0$ (Figures 5.47-5.55). Wave induced, fore-body, and keel vorticies were traced along the ship.

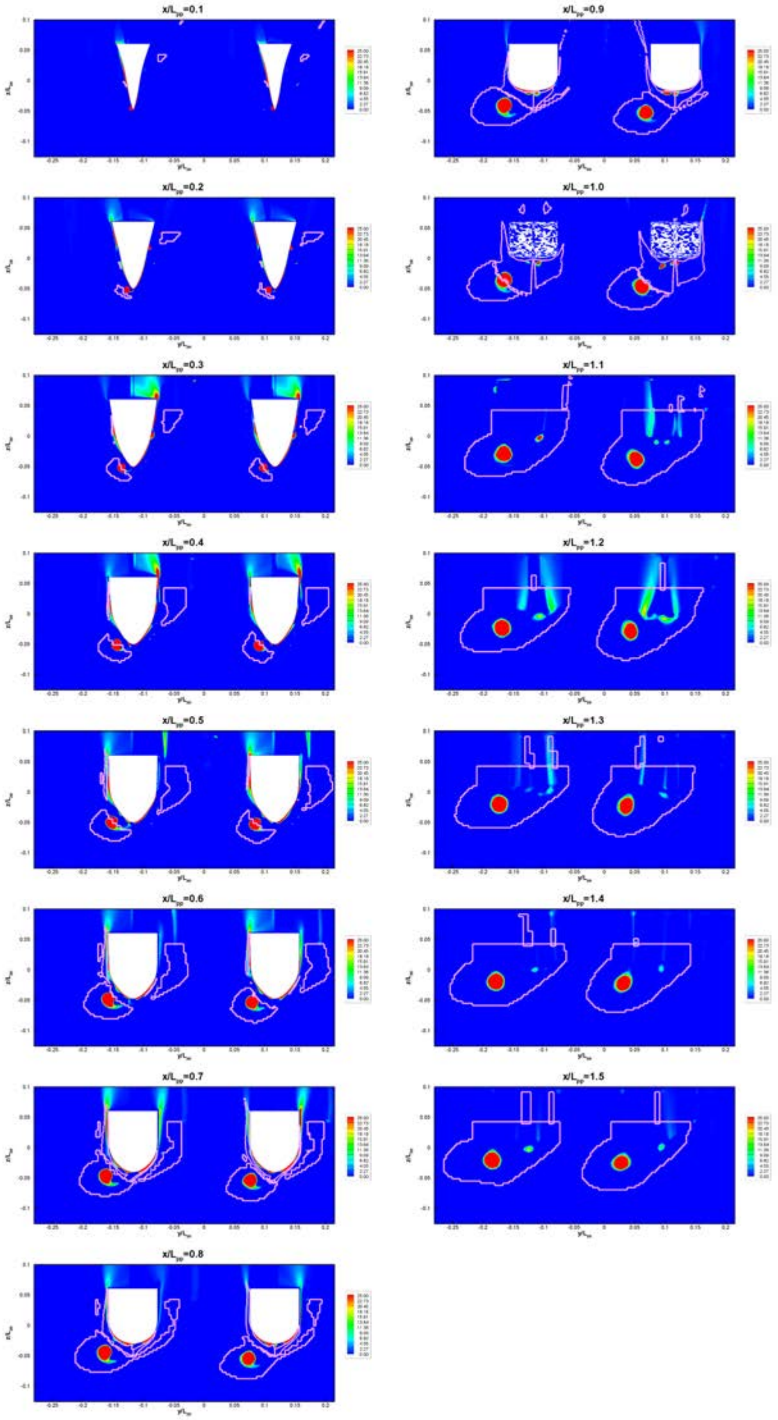

Figure 5.1: Q plot and LES activation (indicated by pink outline) at $\beta = 6^0$ and $Fr = 0.5$ for G3 at even keel condition

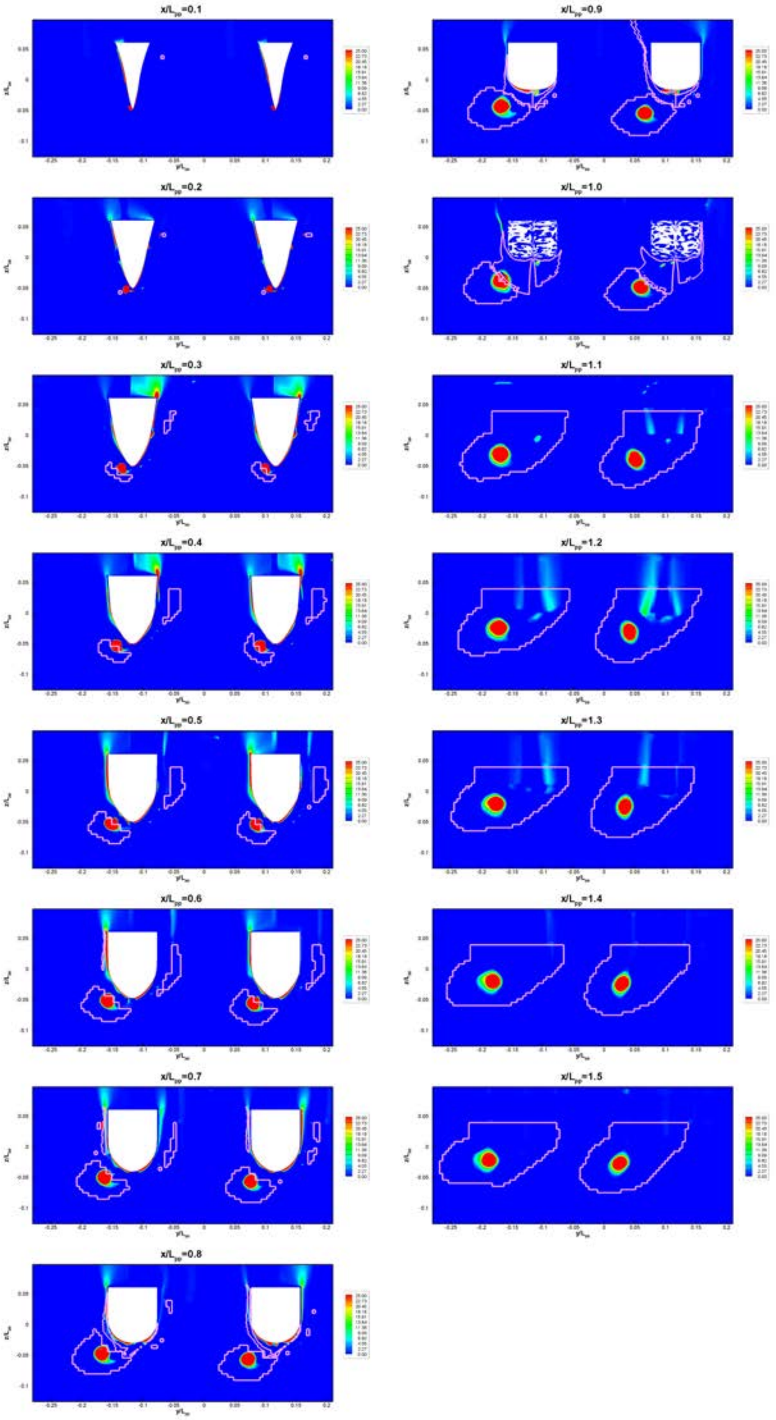

Figure 5.2: Q plot and LES activation (indicated by pink outline) at $\beta = 6^0$ and $Fr = 0.5$ for G4 at even keel condition

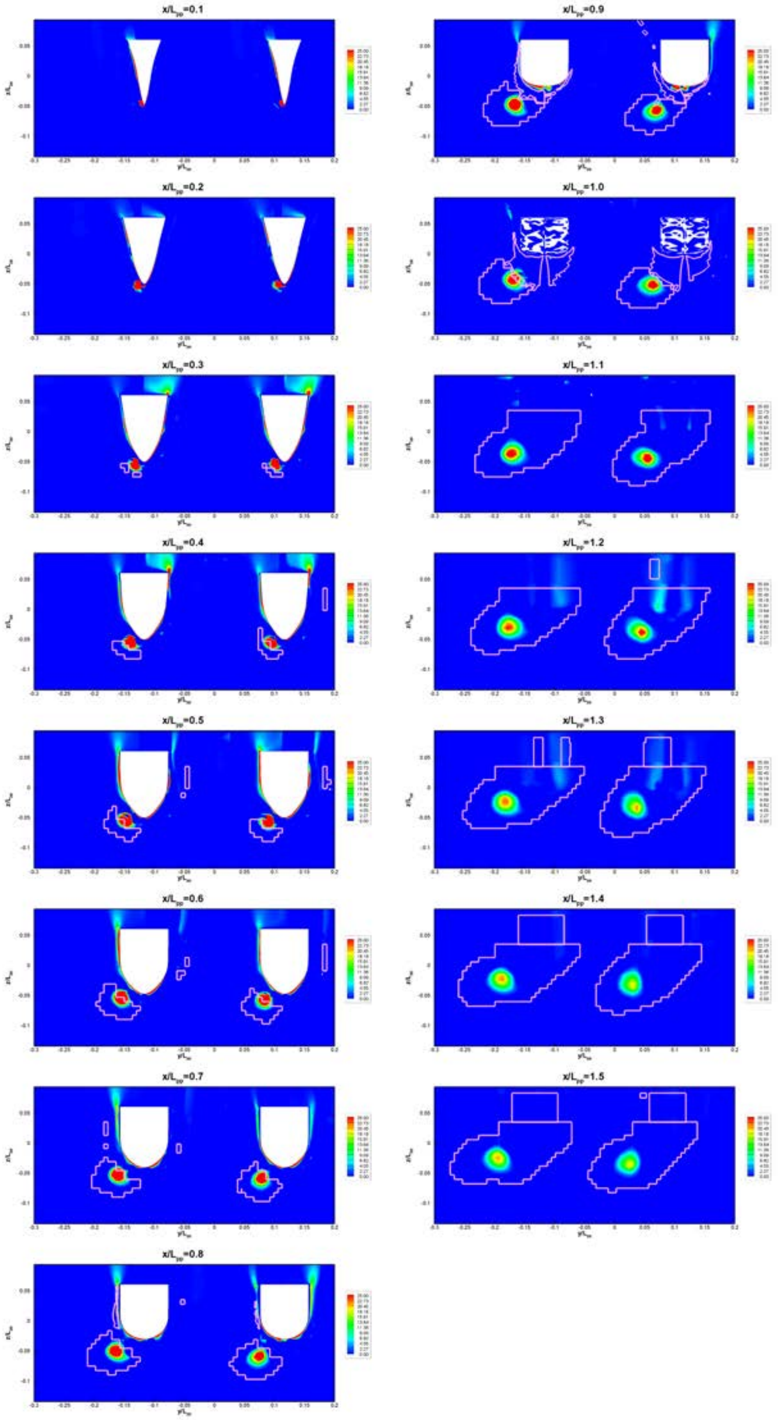

Figure 5.3: Q plot and LES activation (indicated by pink outline) at $\beta = 6^0$ and $Fr = 0.5$ for G5 at even keel condition

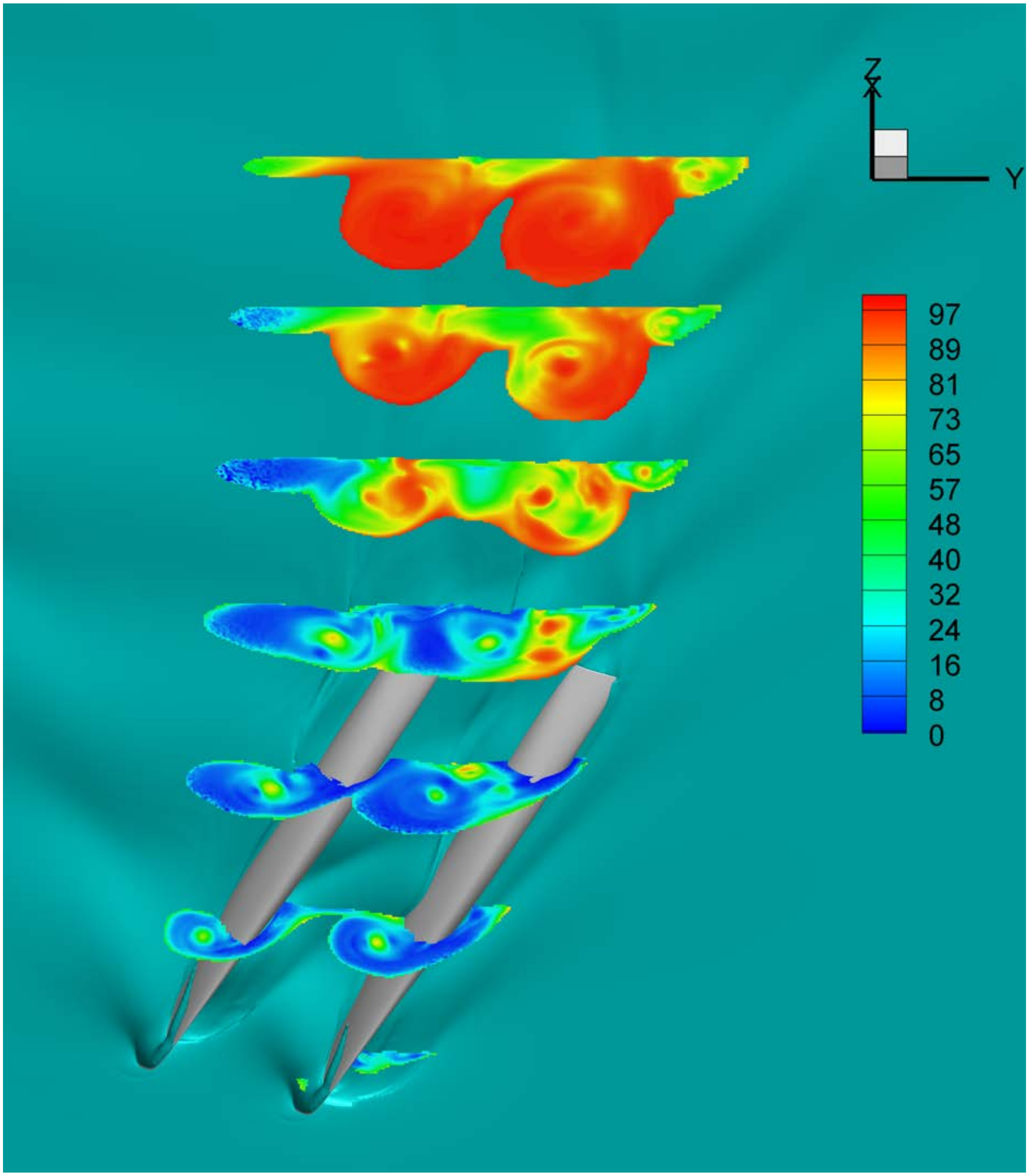

Figure 5.4: Percentage of resolved turbulence in the LES activated Region at $\beta = 24^0$, and $Fr = 0.3$

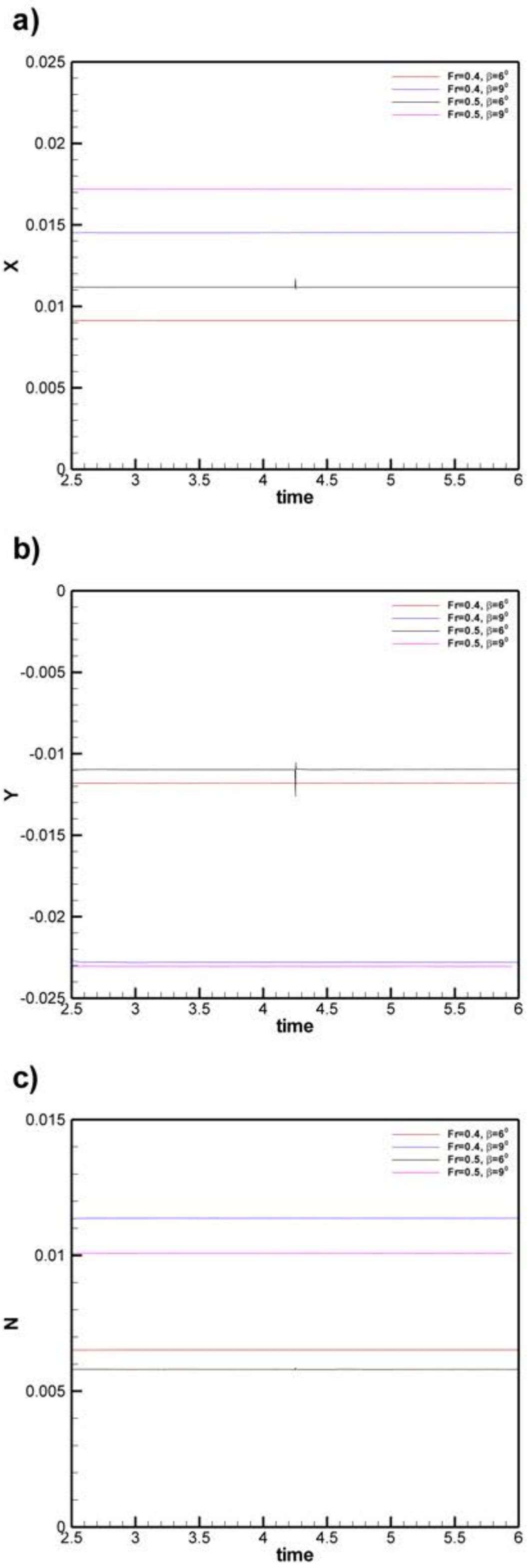

Figure 5.5: Time history for $Fr = 0.4, 0.5$ and $\beta = 6^0, 9^0$ fixed at dynamic sink and trim using G3

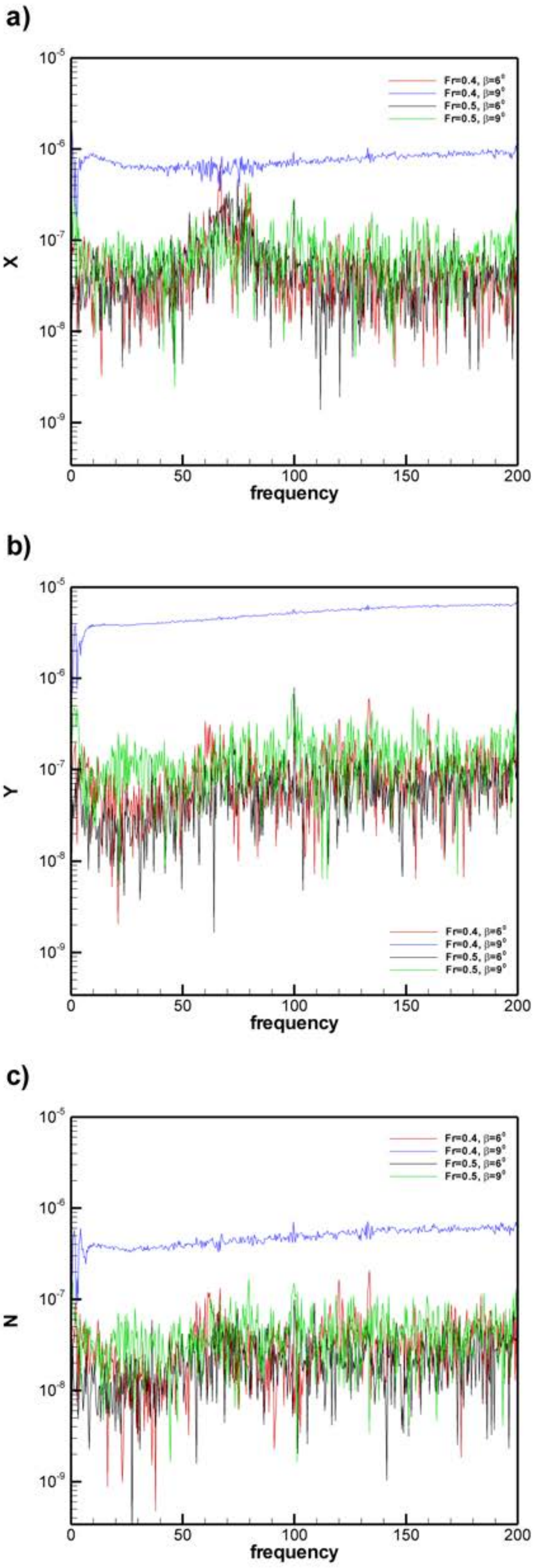

Figure 5.6: FFT for $Fr = 0.4, 0.5$ and $\beta = 6^0, 9^0$ fixed at dynamic sink and trim using G3

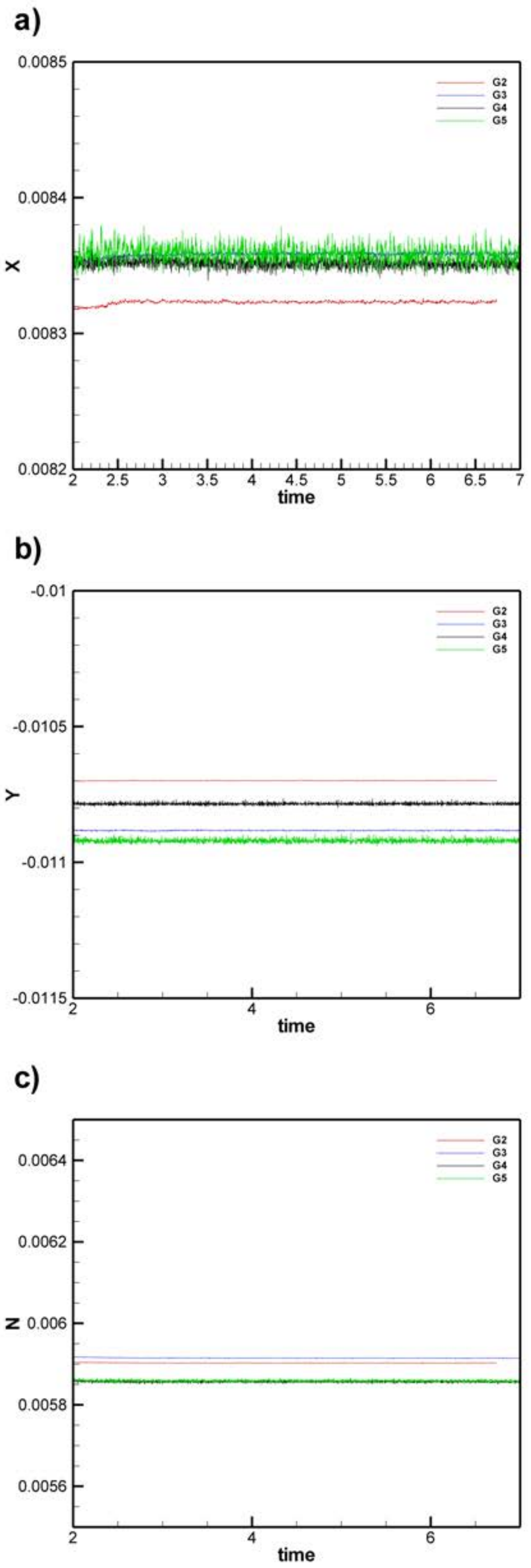

Figure 5.7: Time history for 0.5 and $\beta = 6^0$ fixed at even keel condition using G2-G5

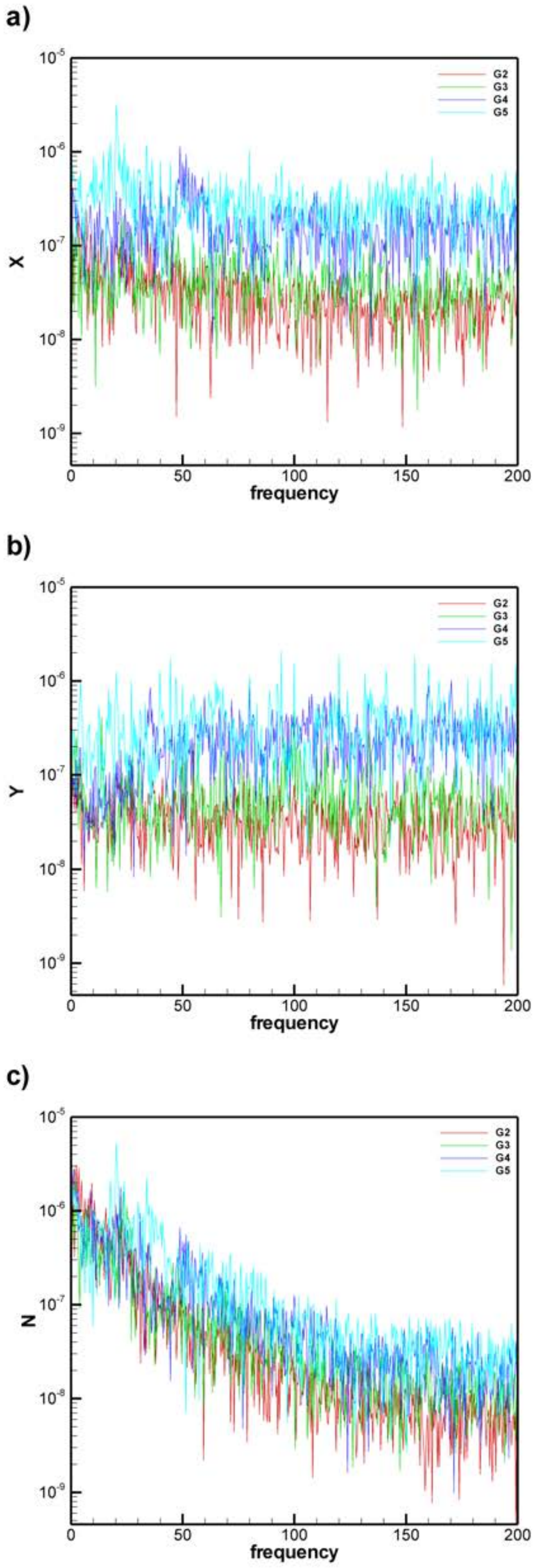

Figure 5.8: FFT for 0.5 and $\beta = 6^0$ fixed at even keel condition using G2-G5

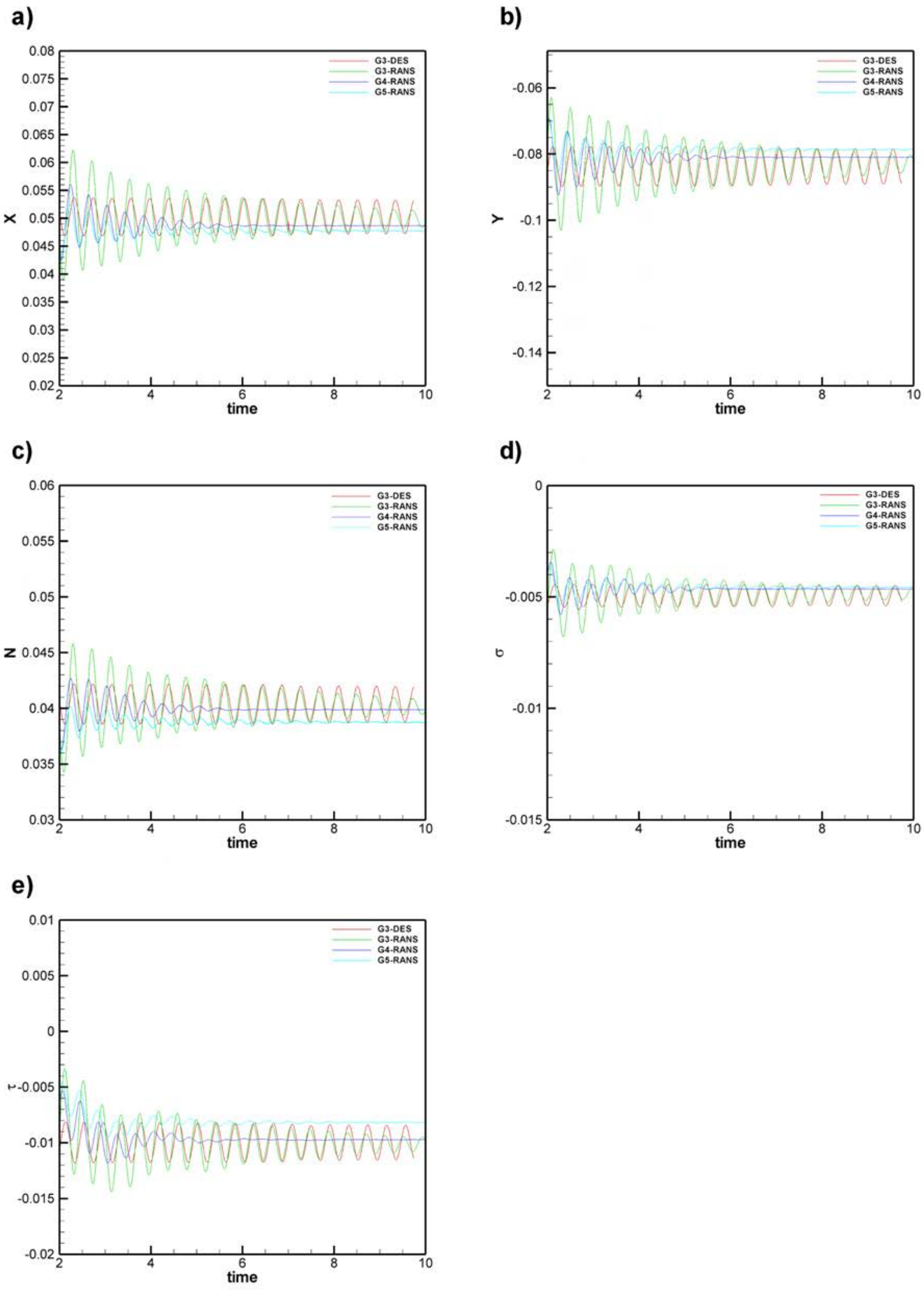

Figure 5.9: Time history for $Fr = 0.3$ and $\beta = 24^0$ using G3

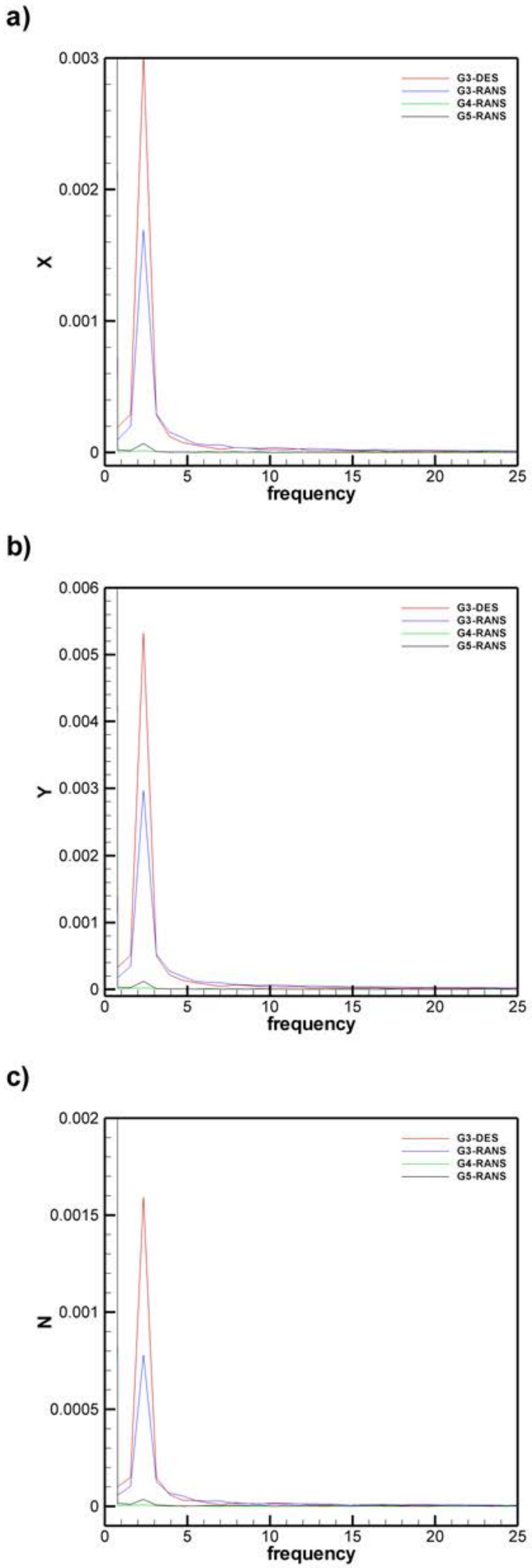

Figure 5.10: FFT for $Fr = 0.3$ and $\beta = 24^0$ using G3

Table 5.1: Verification study at even keel, $\beta = 6^0$ and $Fr = 0.5$ using DES

Grids	Variables	R	Convergence	$U_I\%S_1$	$U_G\%S_1$	$U_{SN}\%S_1$
G4,G3,G2	X	6.30	MD	-	-	-
	Xf	-0.17	OC	0.0065	0.1876	0.1877
	Xp	2.64	MD	-	-	-
	Y	-1.89	OD	-	-	-
	Yf	-5.25	OD	-	-	-
	Yp	-2.24	OD	-	-	-
	N	0.29	MC	0.0323	11.7327	11.7328
	Nf	0.29	MC	0.0323	11.7327	11.7328
	Np	-0.96	OC	0.0489	0.5354	0.5376
G5,G4,G3	X	-0.35	OC	0.0349	0.0501	0.0611
	Xf	1.28	MD	-	-	-
	Xp	1.22	MD	-	-	-
	Y	-0.72	OC	0.0365	0.5828	0.5840
	Yf	-0.35	OC	0.0607	0.5722	0.5754
	Yp	-0.73	OC	0.0294	0.4667	0.4676
	N	1.18	MD	-	-	-
	Nf	1.18	MD	-	-	-
	Np	-10.19	OD	-	-	-

Table 5.2: Verification study at $\beta = 24^0$ and $Fr = 0.3$ using URANS

Grids	Variables	R	Convergence	$U_I\%S_1$	$U_G\%S_1$	$U_{SN}\%S_1$
G5,G4,G3	X	0.91	MC	0.013	42.426	42.426
	Xf	1.66	MD	0.031	-	-
	Xp	-0.54	OD	0.019	-	-
	Y	0.54	MC	0.163	3.100	3.104
	Yf	1.77	MD	6.868	-	-
	Yp	0.11	MC	0.078	0.323	0.332
	N	0.03	MC	0.006	0.141	0.141
	Nf	0.21	MC	1.215	46.588	46.604
	Np	1.29	MD	0.013	-	-
	s	2.14	MD	0.003	-	-
	t	0.15	MC	0.470	12.250	12.259

Table 5.3: Error comparison for

URANS and DES

at $\beta = 24^0$ and $Fr = 0.3$

Variables	G3-URANS	G3-DES
X	-3.72	-2.18
Y	-15.05	-13.30
N	38.63	40.29
σ	19.28	20.67
τ	-98.87	-98.88

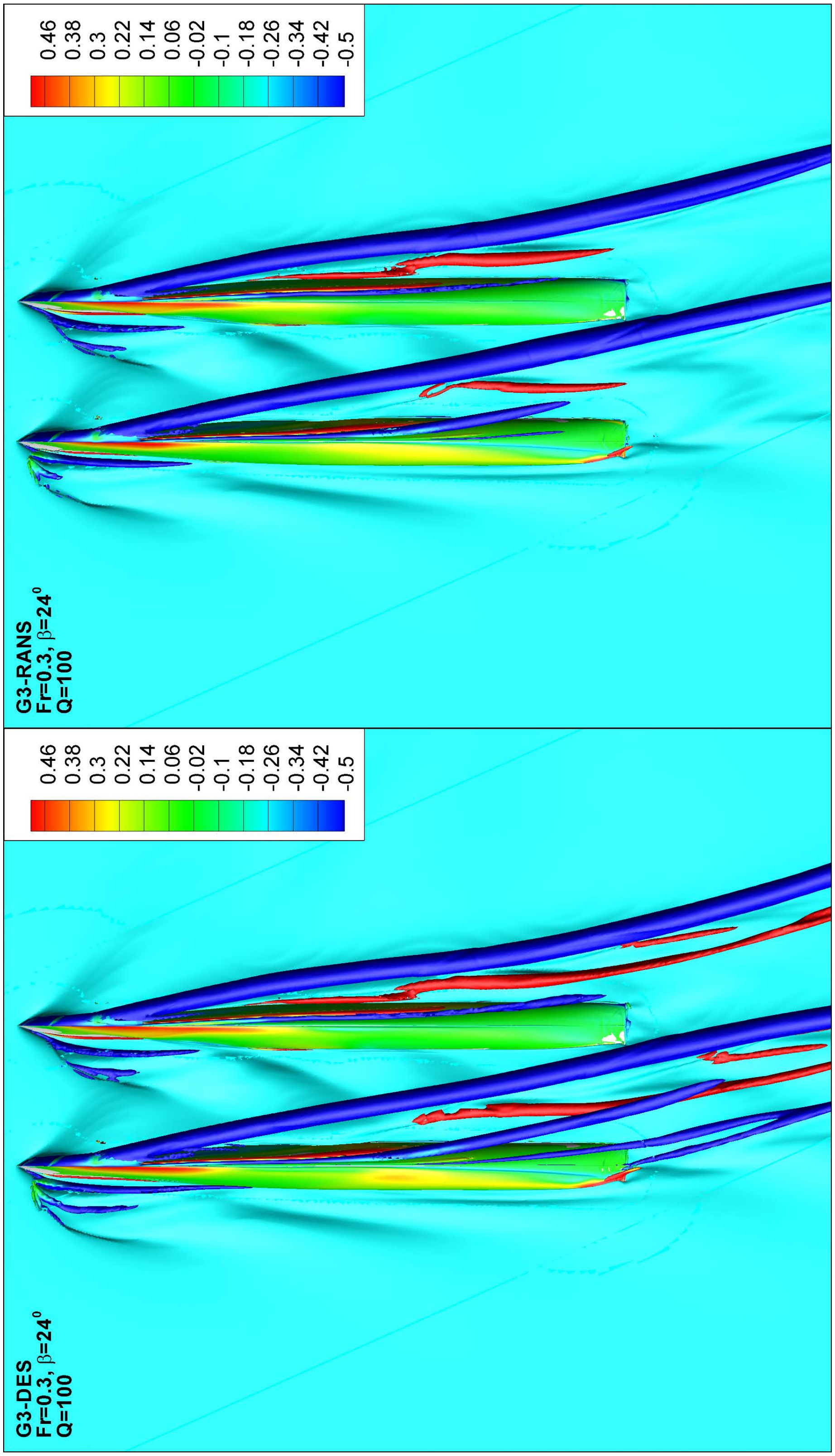

Figure 5.11: Comparison of vortical structures between URANS and DES $\beta = 24^0$, and $Fr = 0.3$

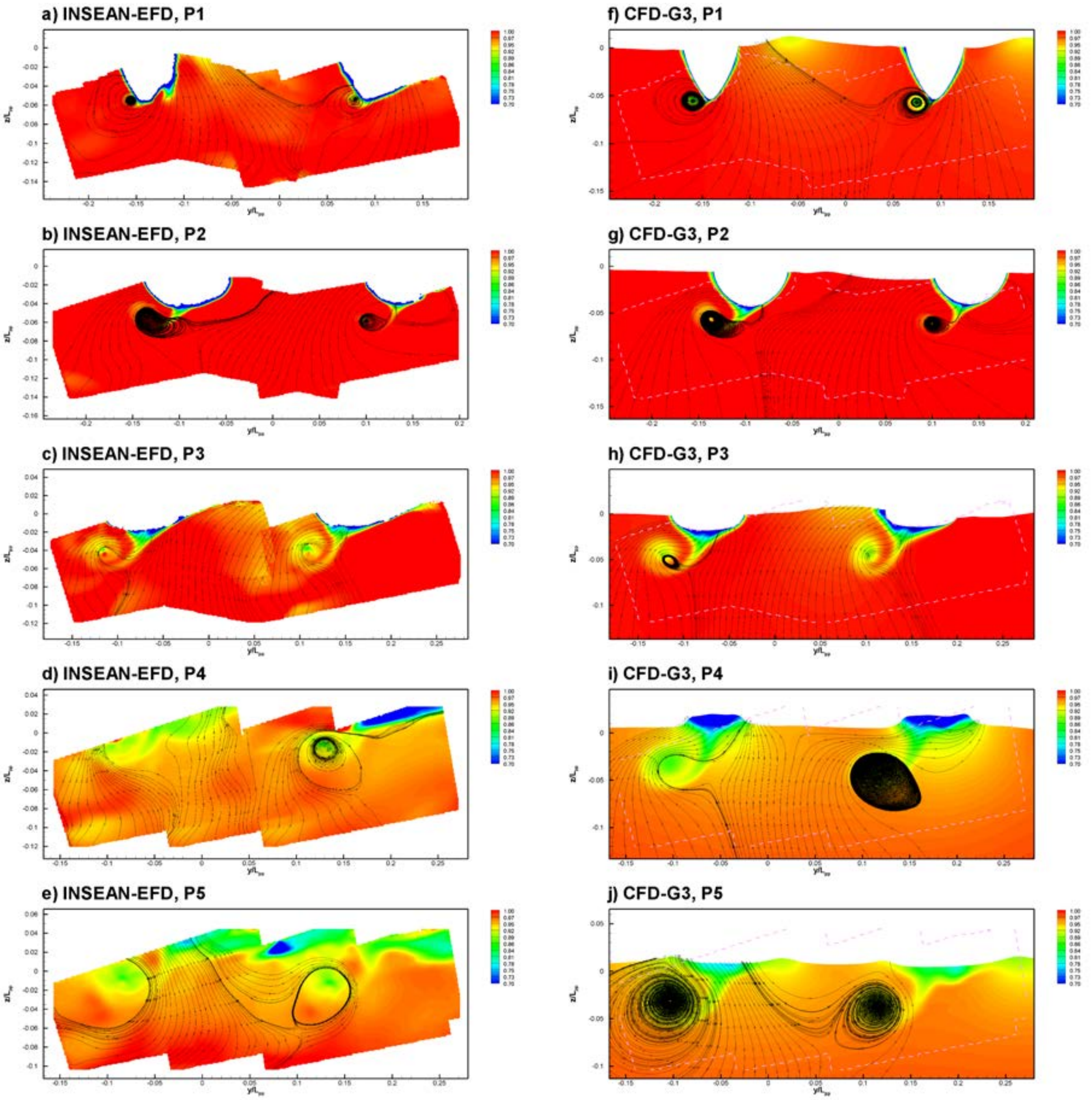

Figure 5.12: EFD-CFD comparison at $Fr = 0.4$ and $\beta = 6^0$ for u-velocity

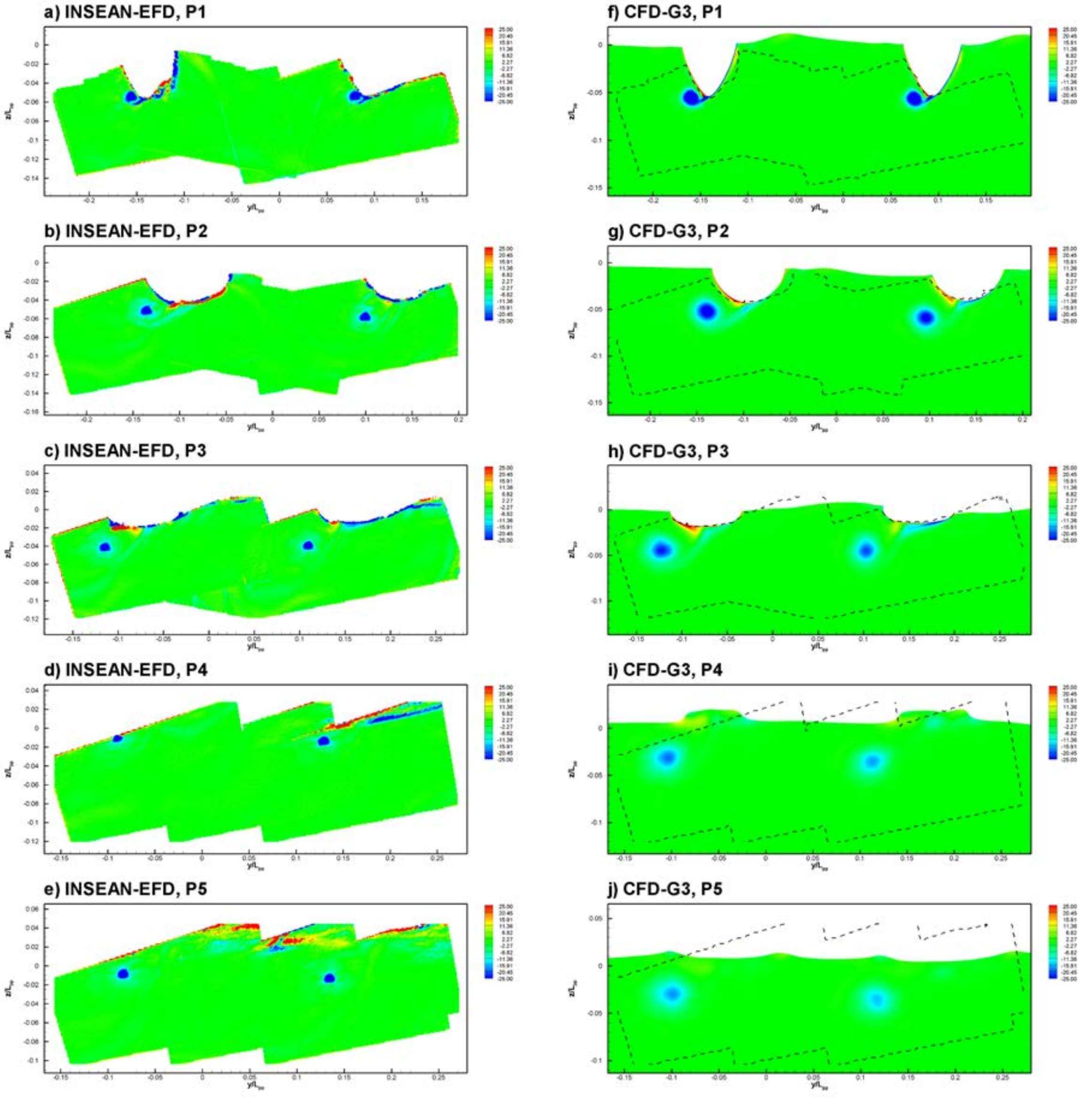

a) INSEAN-EFD, P1

b) INSEAN-EFD, P2

c) INSEAN-EFD, P3

d) INSEAN-EFD, P4

e) INSEAN-EFD, P5

f) CFD-G3, P1

g) CFD-G3, P2

h) CFD-G3, P3

i) CFD-G3, P4

j) CFD-G3, P5

Figure 5.13: EFD-CFD comparison at $Fr = 0.4$ and $\beta = 6^0$ for vorticity

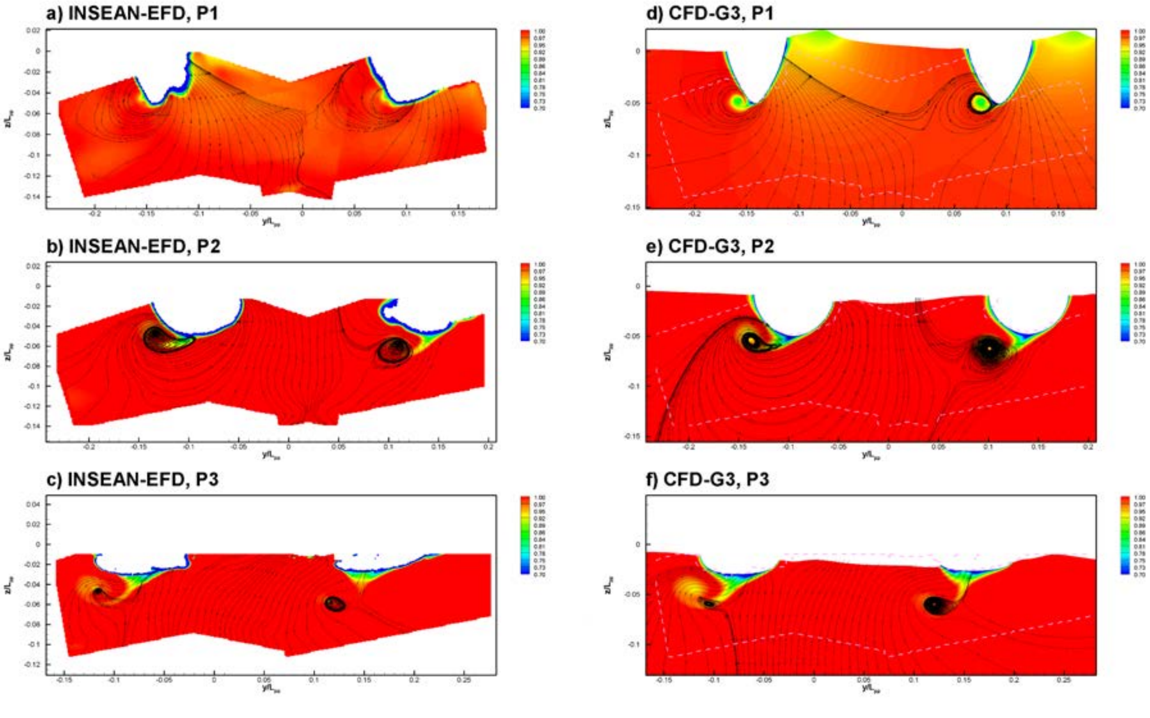

Figure 5.14: EFD-CFD comparison at $Fr = 0.5$ and $\beta = 6^0$ for u velocity

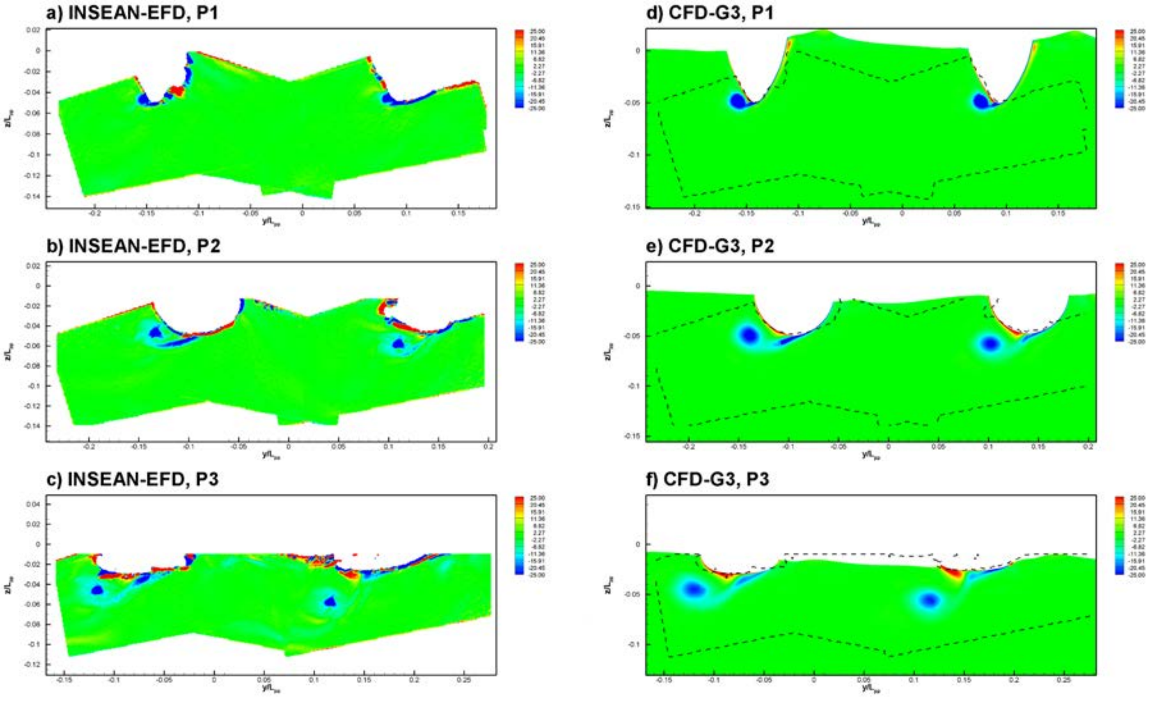

Figure 5.15: EFD-CFD comparison at $Fr = 0.5$ and $\beta = 6^0$ for vorticity

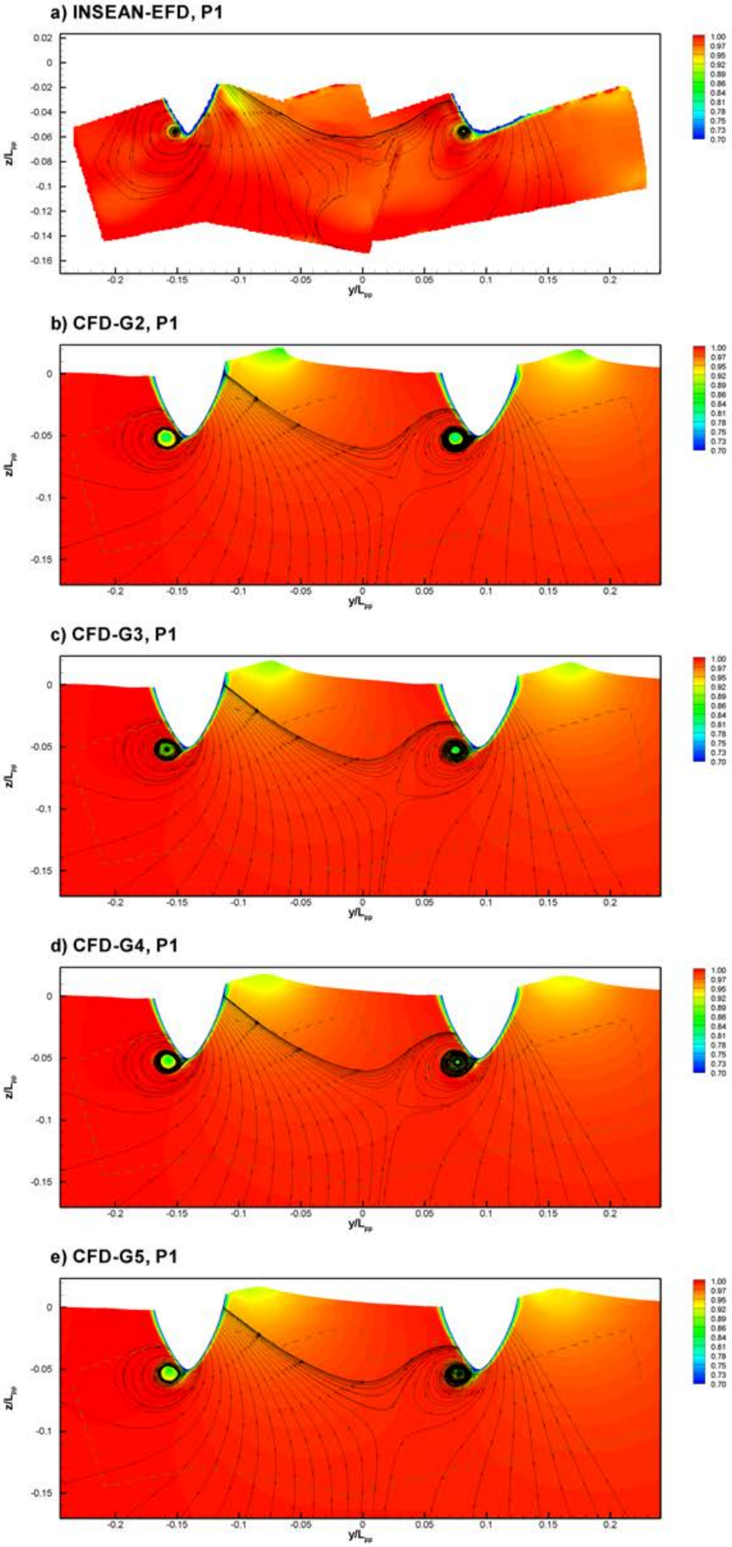

Figure 5.16: EFD-CFD comparison at even keel, $Fr = 0.5$ and $\beta = 6^0$ for u velocity

a) INSEAN-EFD, P1

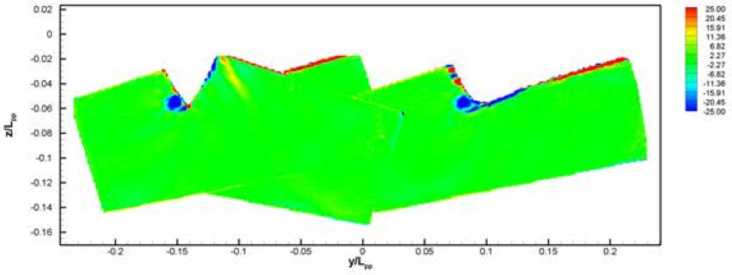

b) CFD-G2, P1

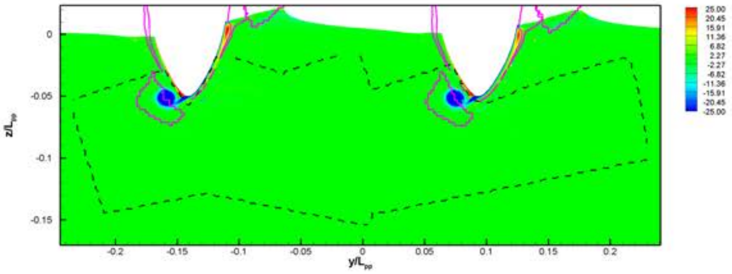

c) CFD-G3, P1

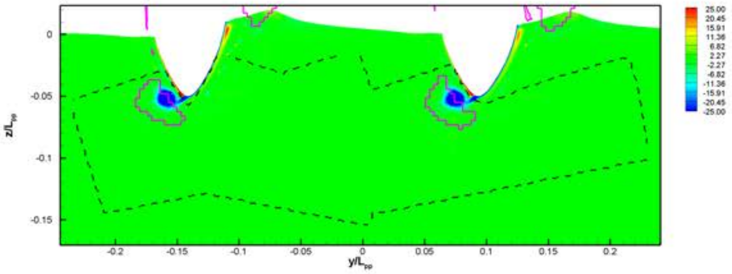

d) CFD-G4, P1

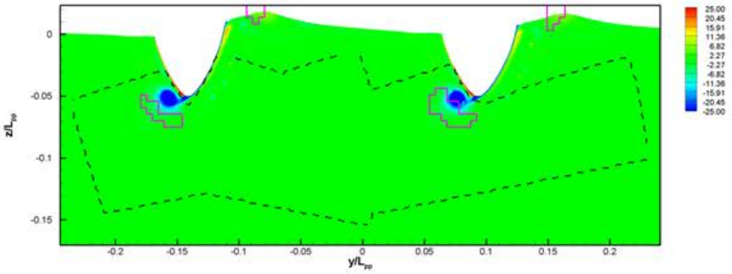

e) CFD-G5, P1

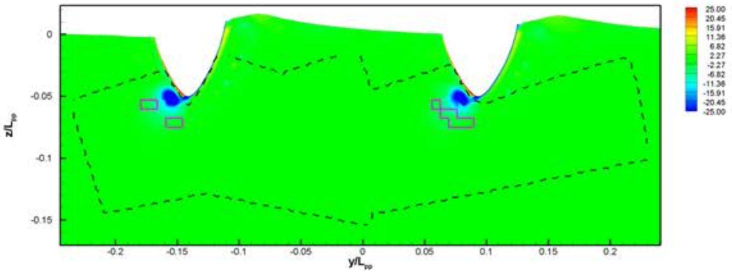

Figure 5.17: EFD-CFD comparison at even keel, $Fr = 0.5$ and $\beta = 6^0$ for vorticity

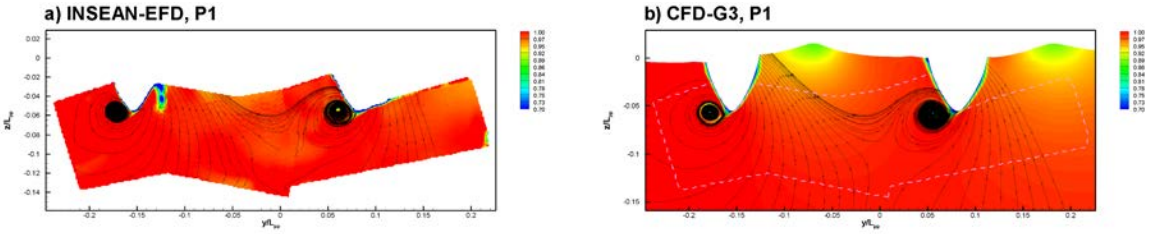

Figure 5.18: EFD-CFD comparison, $Fr = 0.4$ and $\beta = 9^0$ for u velocity

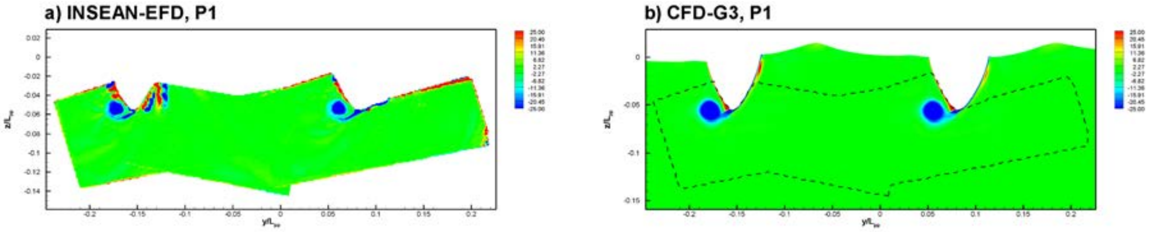

Figure 5.19: EFD-CFD comparison, $Fr = 0.4$ and $\beta = 9^0$ for vorticity

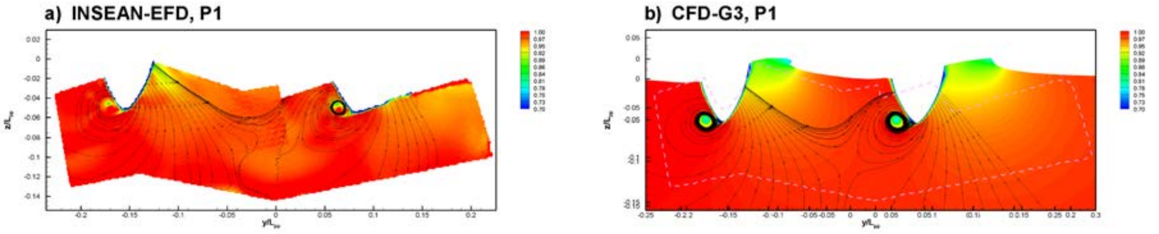

Figure 5.20: EFD-CFD comparison, $Fr = 0.5$ and $\beta = 9^0$ for u velocity

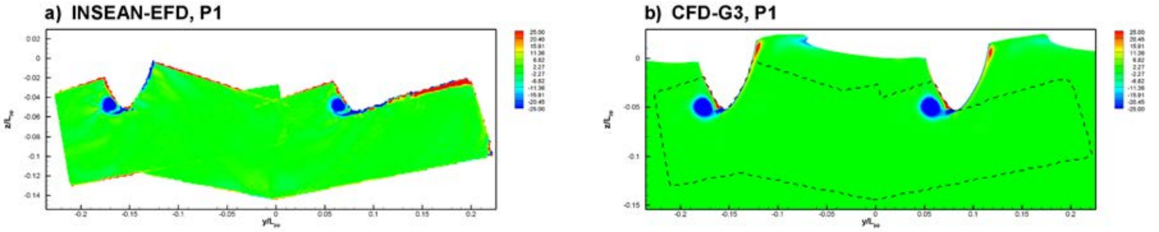

Figure 5.21: EFD-CFD comparison, $Fr = 0.5$ and $\beta = 9^0$ for vorticity

Table 5.4: Mean of local velocity error

Ship Orientation	β	Fr	Location	Grid	u	v	w
dynamic sinkage and trim	6	0.4	P1	G3	2.01	2.07	3.33
			P2		2.09	1.69	2.57
			P3		1.11	1.42	2.23
			P4		3.28	6.97	7.99
			P5		6.60	7.09	10.10
dynamic sinkage and trim	6	0.5	P1	G3	1.68	2.32	3.63
			P2		2.40	2.94	4.87
			P3		1.10	1.25	2.56
even keel	6	0.5	P1	G2	1.69	2.76	4.39
				G3	1.69	2.72	4.37
				G4	1.69	2.67	4.26
				G5	1.69	2.67	4.26
dynamic sinkage and trim	9	0.4	P1	G3	0.62	1.17	1.59
dynamic sinkage and trim	9	0.5	P1	G3	0.51	0.95	1.27

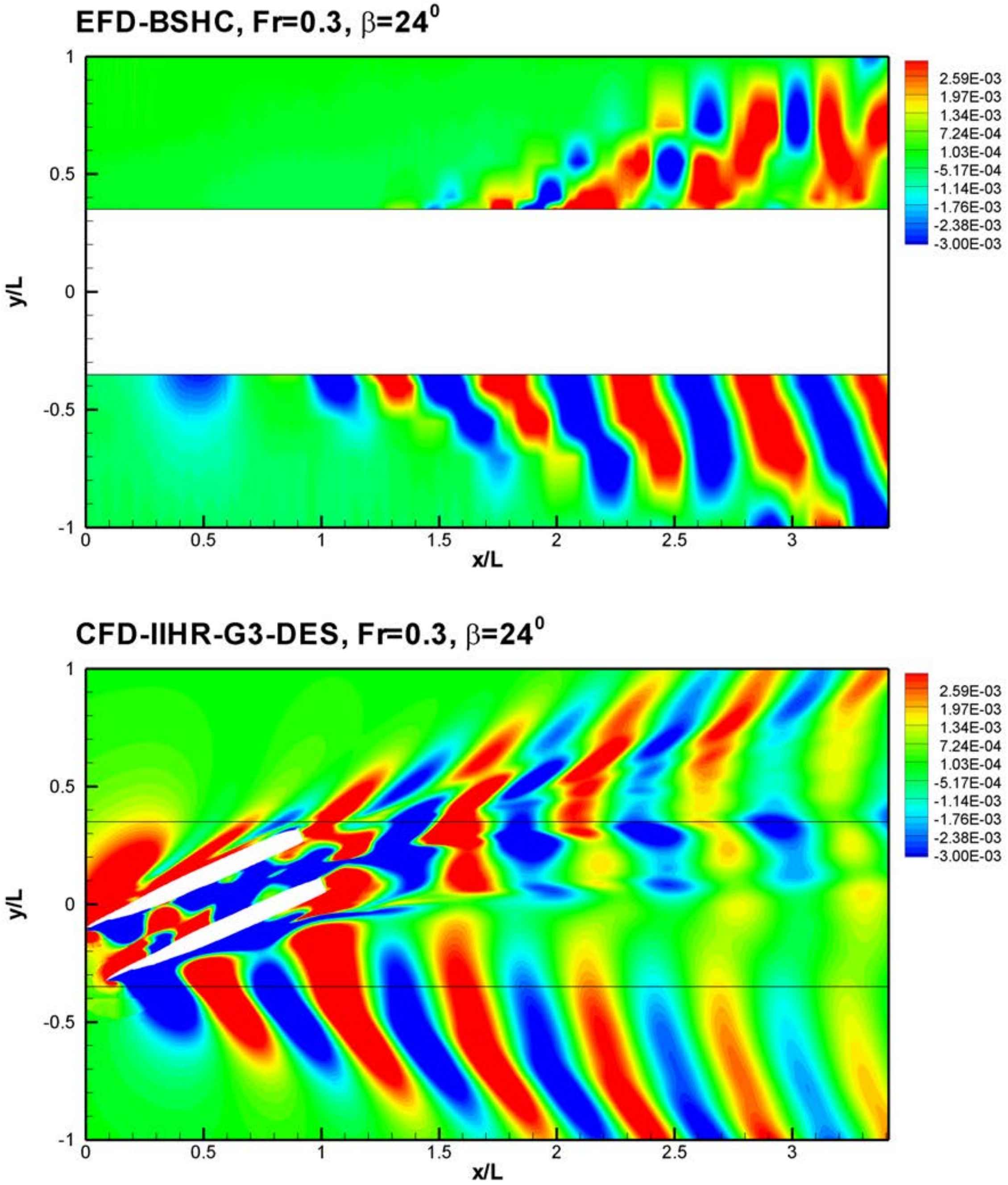

Figure 5.22: Comparison of wave patterns for EFD and CFD at $Fr = 0.3$ and $\beta = 24^0$

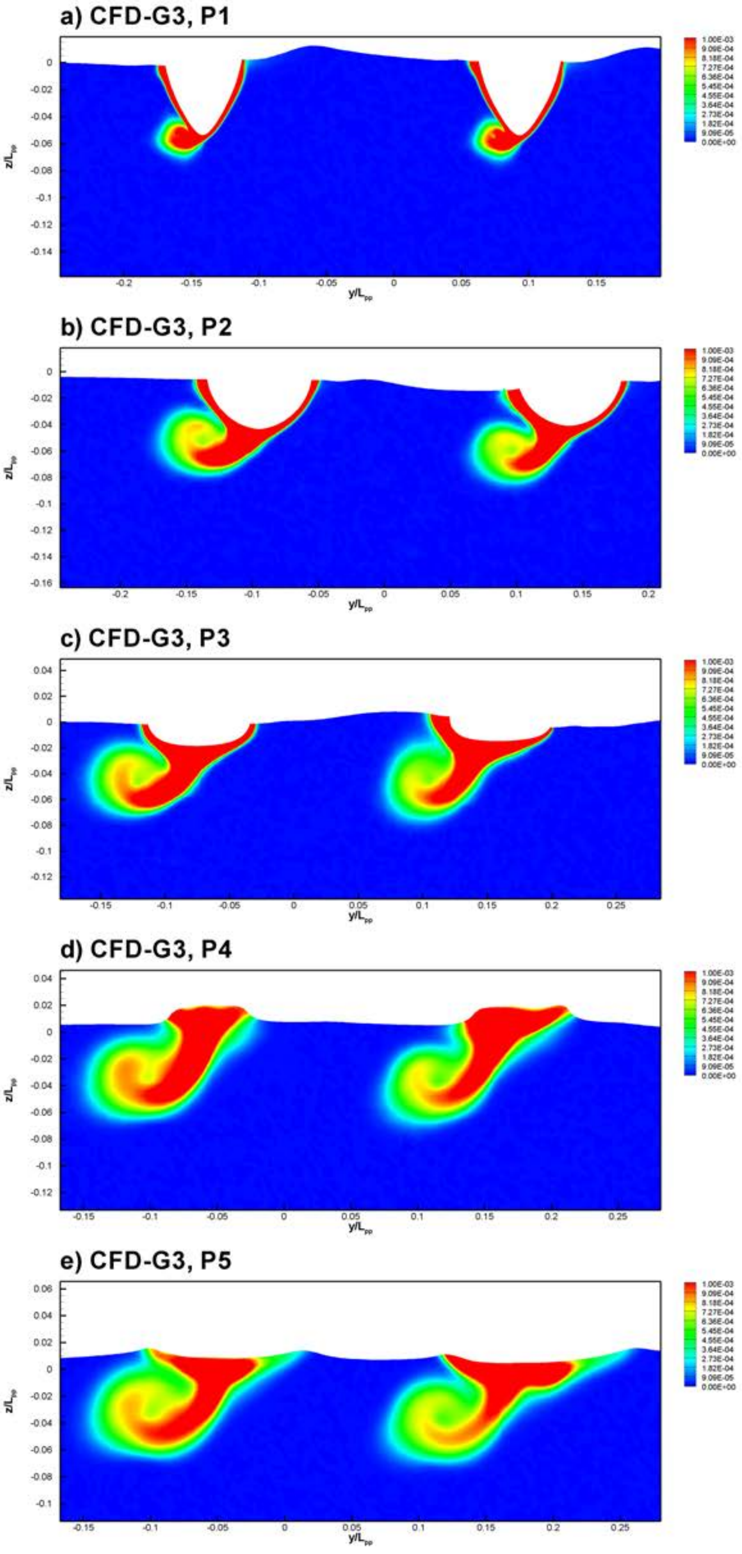
a) CFD-G3, P1

b) CFD-G3, P2

c) CFD-G3, P3

d) CFD-G3, P4

e) CFD-G3, P5

Figure 5.23: CFD TKE at $Fr = 0.4$ and $\beta = 6^0$

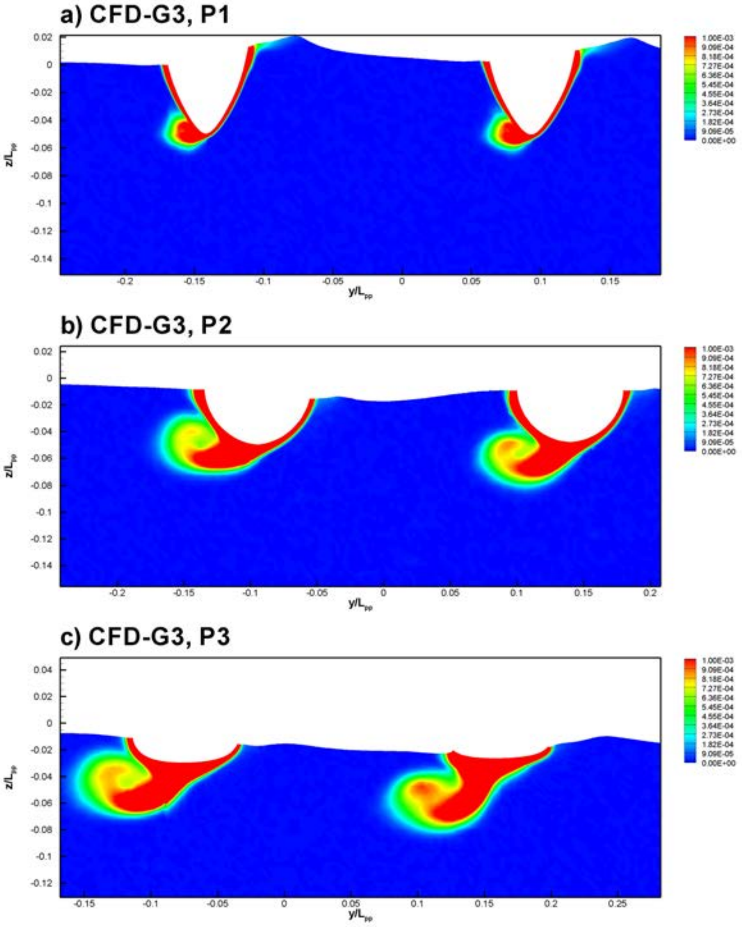

Figure 5.24: CFD TKE at $Fr = 0.5$ and $\beta = 6^0$

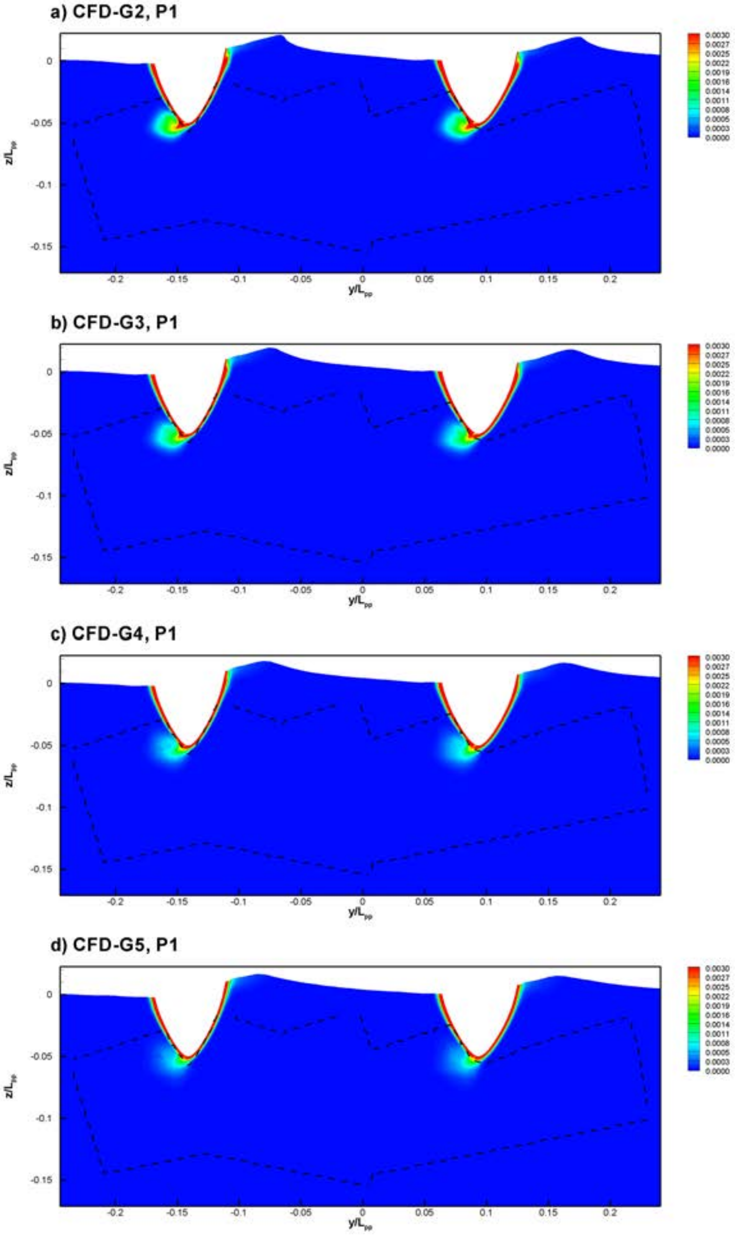

Figure 5.25: CFD TKE at even keel, $Fr = 0.5$ and $\beta = 6^0$

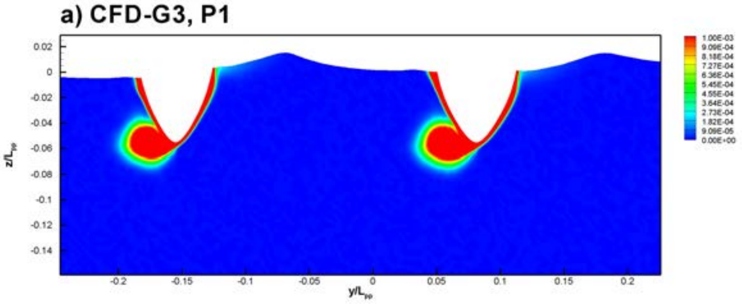

Figure 5.26: CFD TKE at $Fr = 0.4$ and $\beta = 9^0$

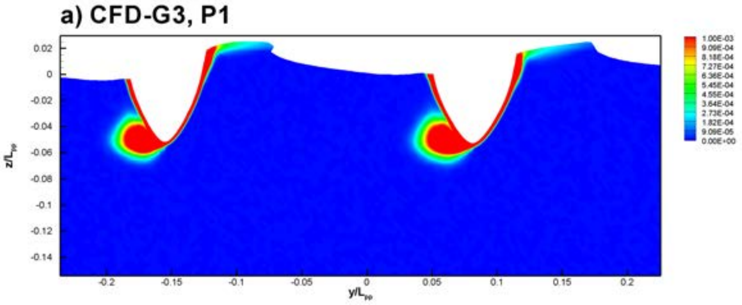

Figure 5.27: CFD TKE at $Fr = 0.5$ and $\beta = 9^0$

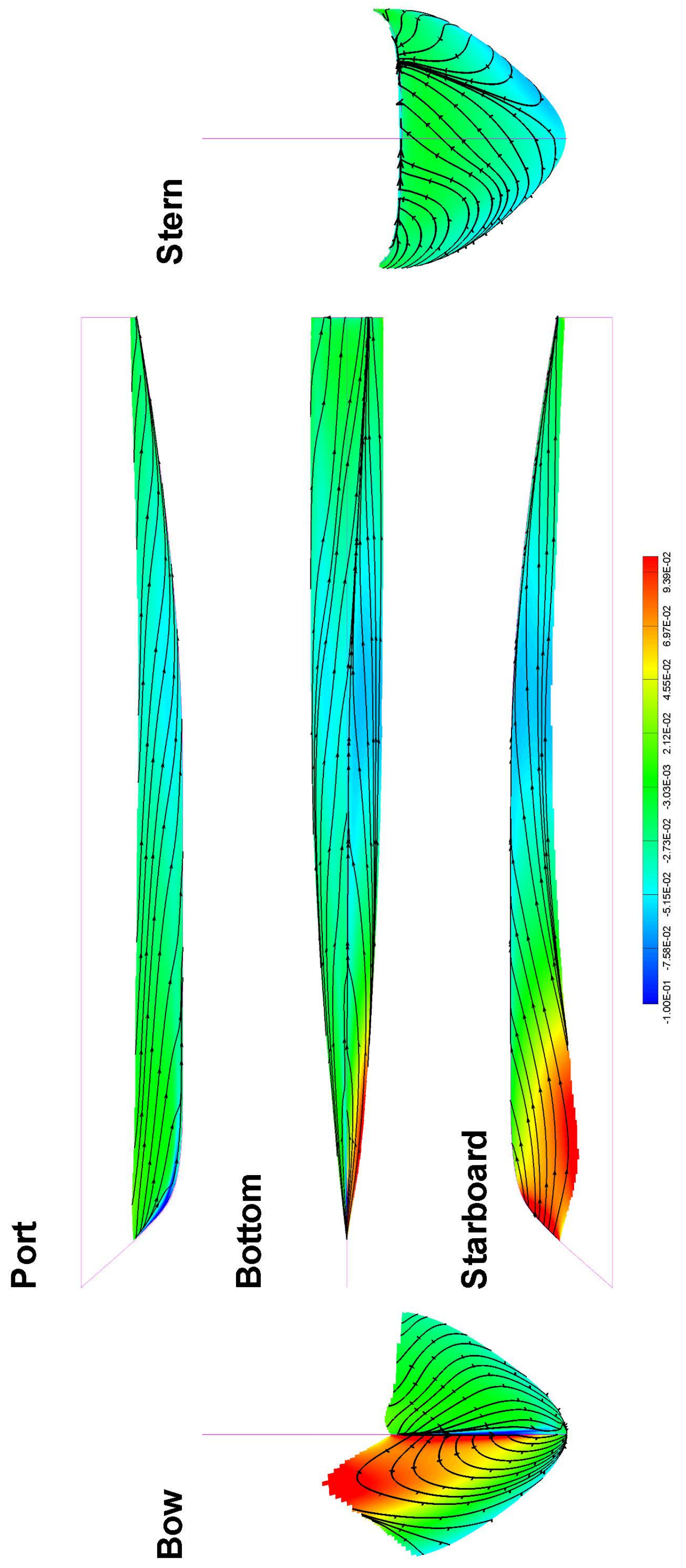

Figure 5.28: Port hull pressure contour and surface streamlines below free surface at fixed dynamic sink and trim with $\beta = 6^0$, and $Fr = 0.4$

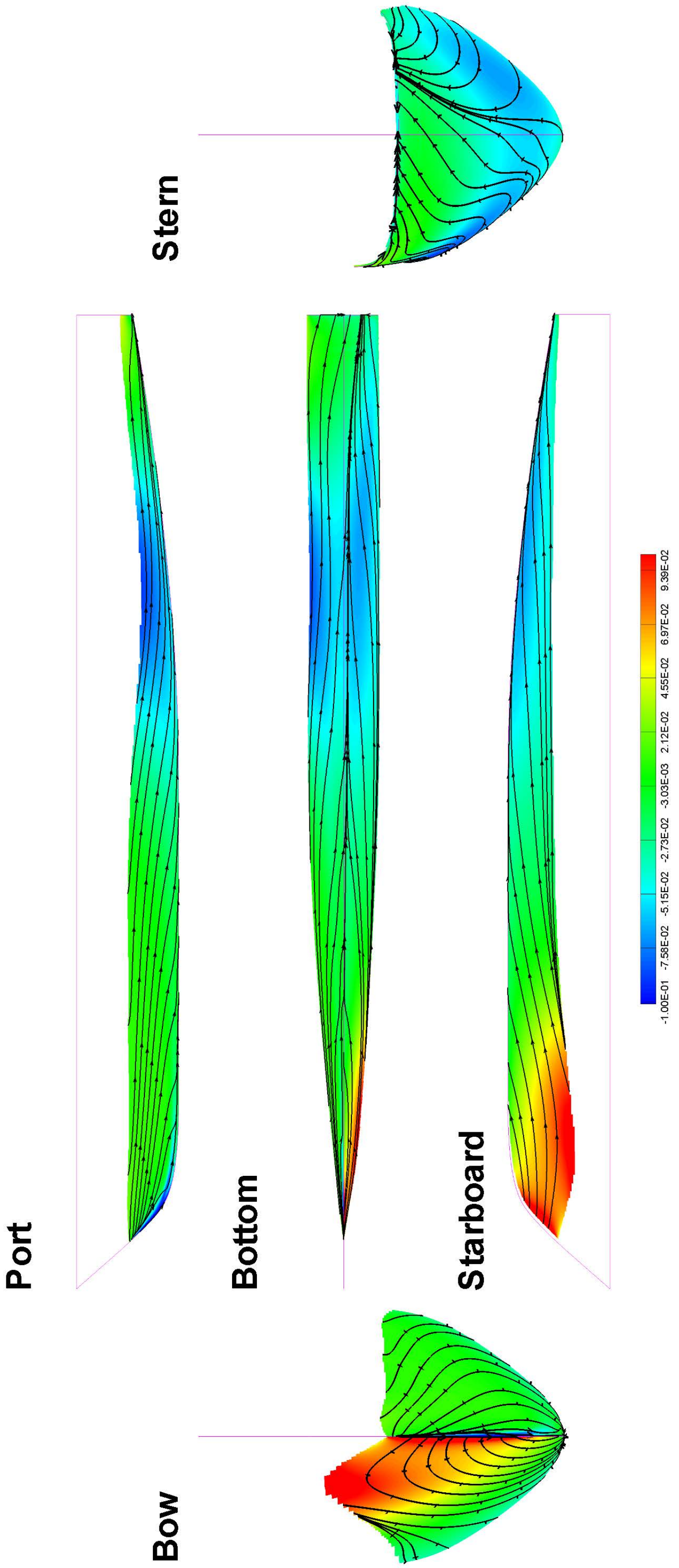

Figure 5.29: Starboard hull pressure contour and surface streamlines below free surface at fixed dynamic sink and trim with $\beta = 6^0$, and $Fr = 0.4$

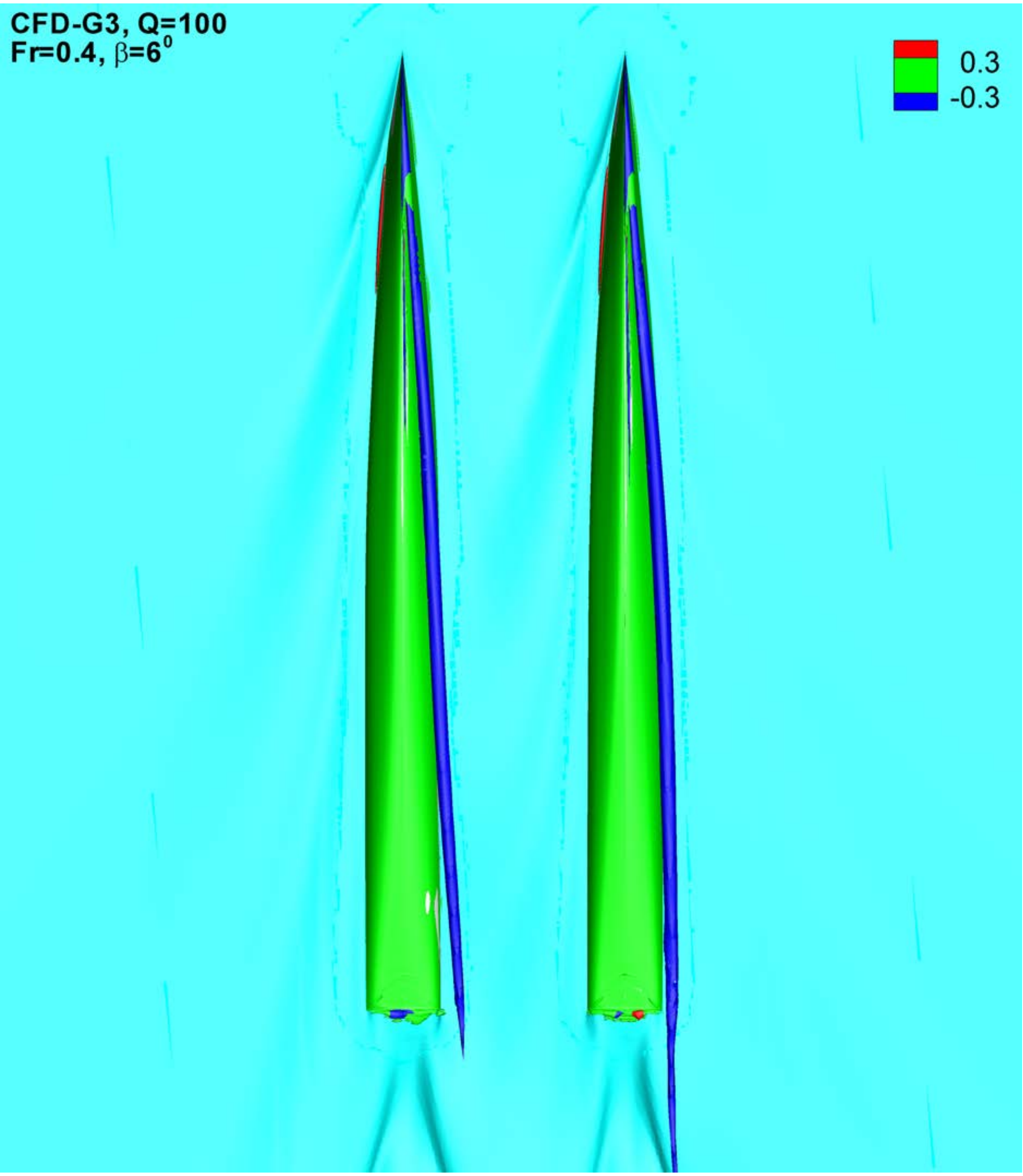

Figure 5.30: Vortex structure for CFD fixed at dynamic sink and trim with $\beta = 6^0$, and $Fr = 0.4$

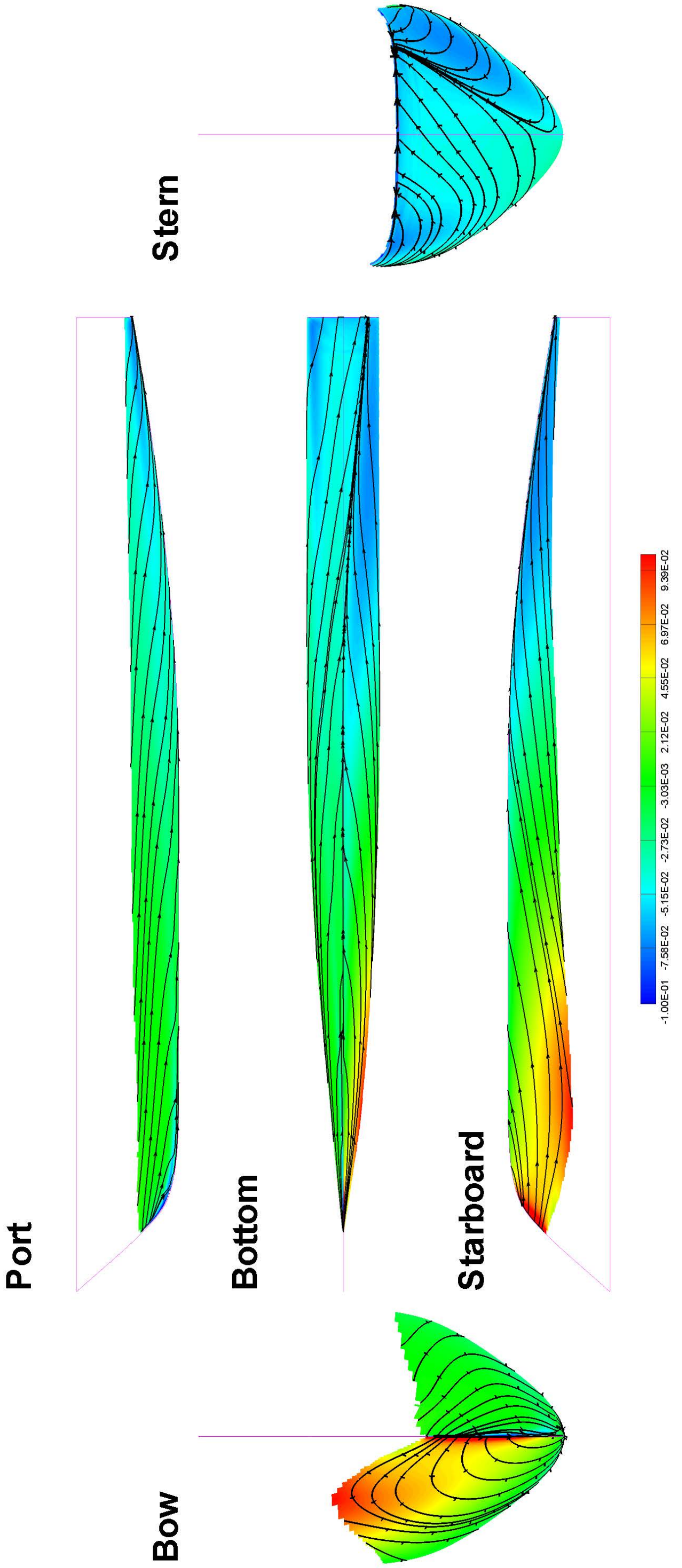

Figure 5.31: Port hull pressure contour and surface streamlines below free surface at fixed dynamic sink and trim with $\beta = 6^0$, and $Fr = 0.5$

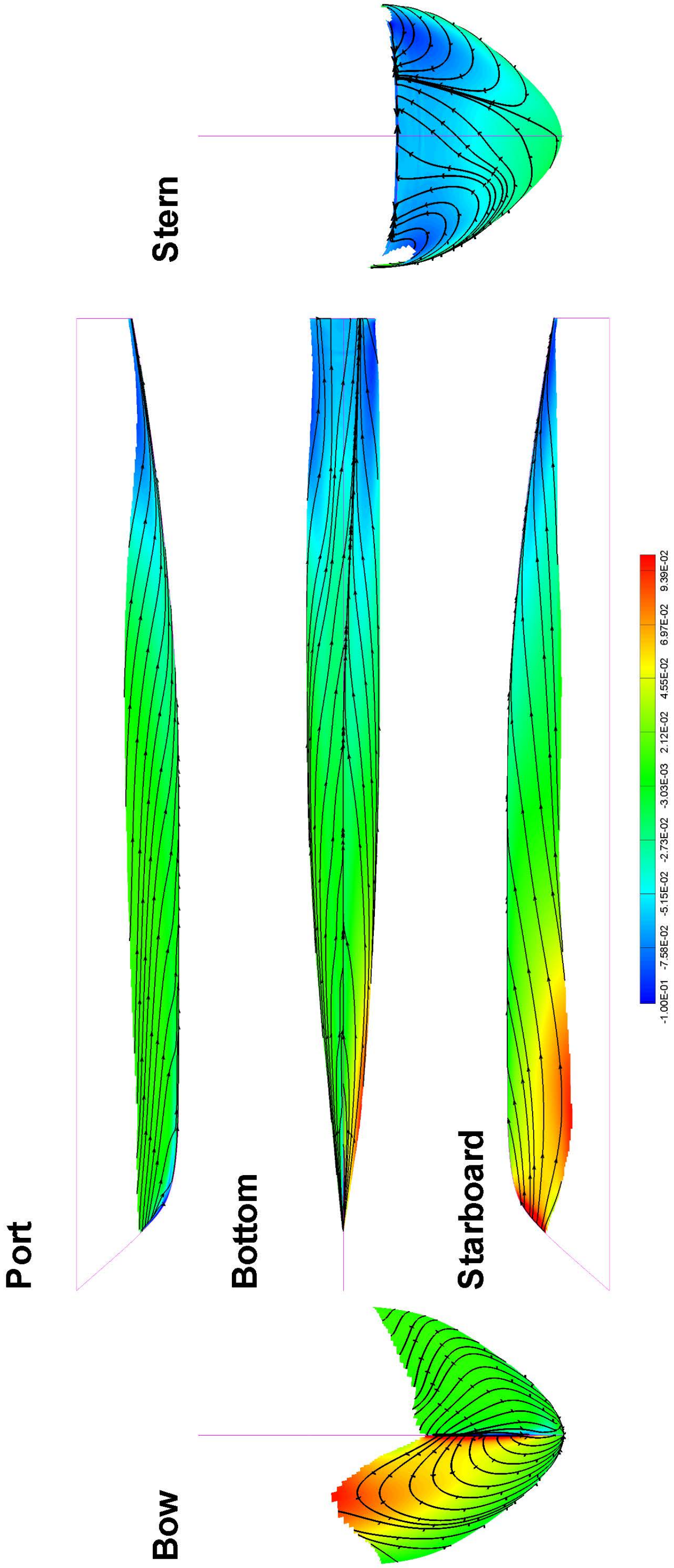

Figure 5.32: Starboard hull pressure contour and surface streamlines below free surface at fixed dynamic sink and trim with $\beta = 6^0$, and $Fr = 0.5$

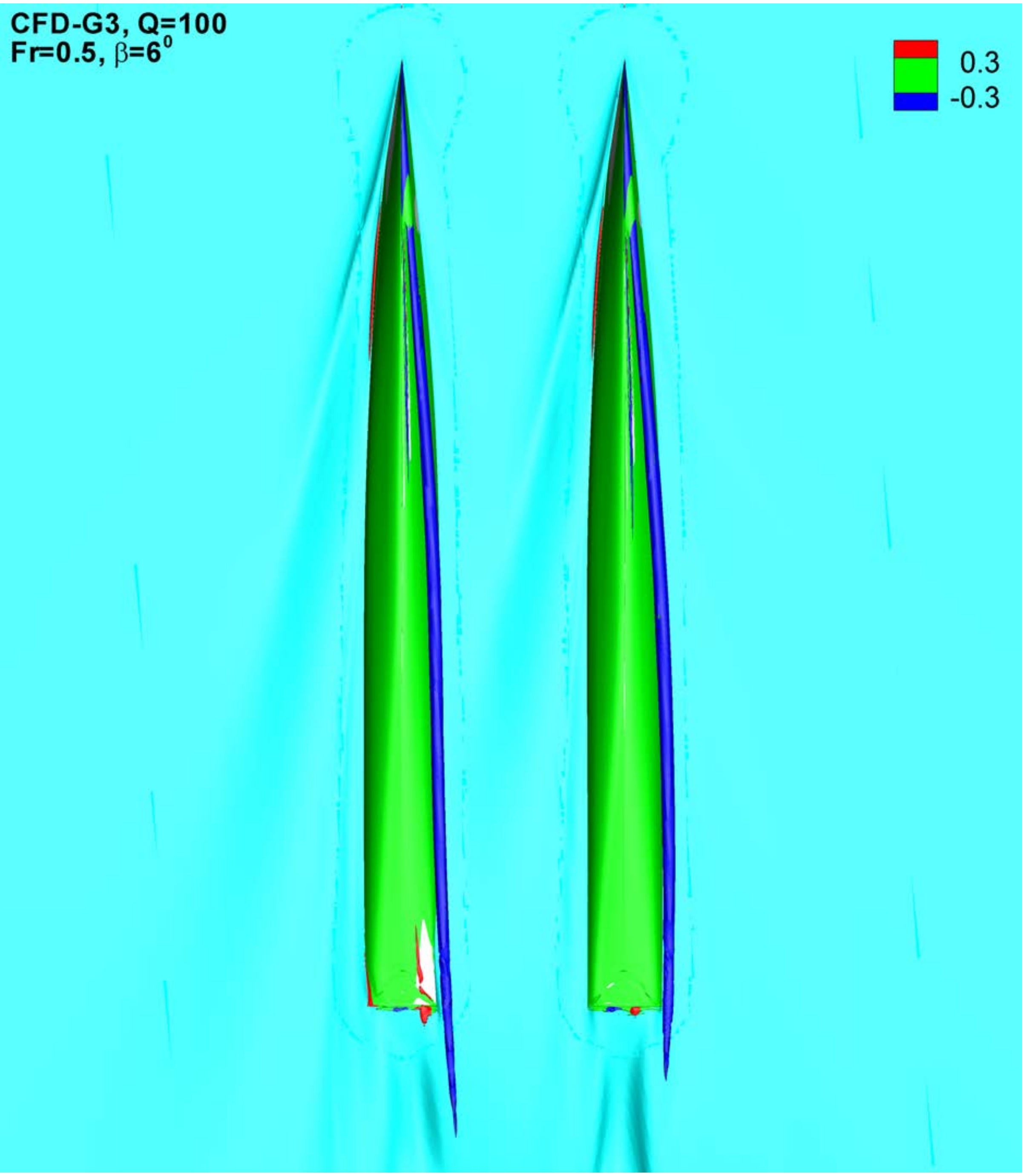

Figure 5.33: Vortex structure for CFD fixed at dynamic sink and trim with $\beta = 6^0$, and $Fr = 0.5$

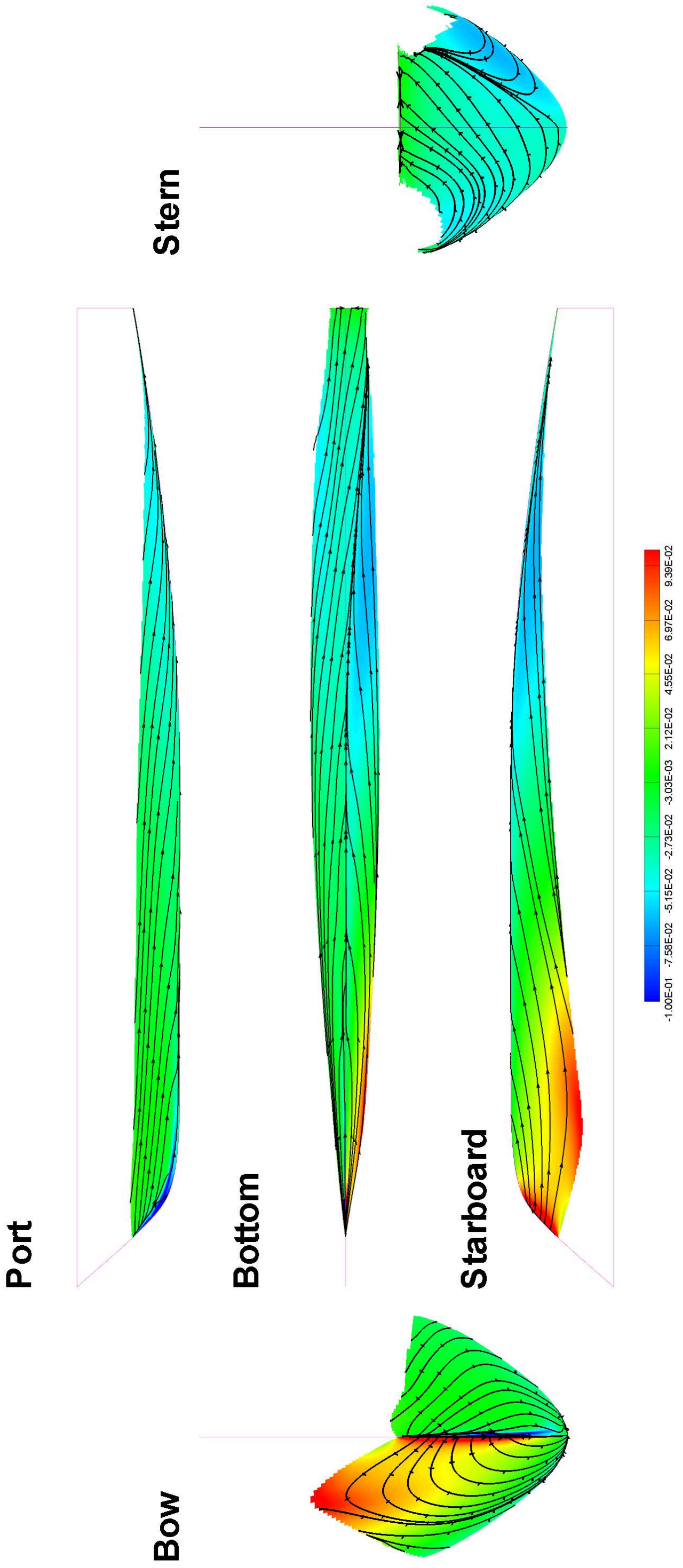

Figure 5.34: Port hull pressure contour and surface streamlines below free surface at even keel with $\beta = 6^0$, and $Fr = 0.5$

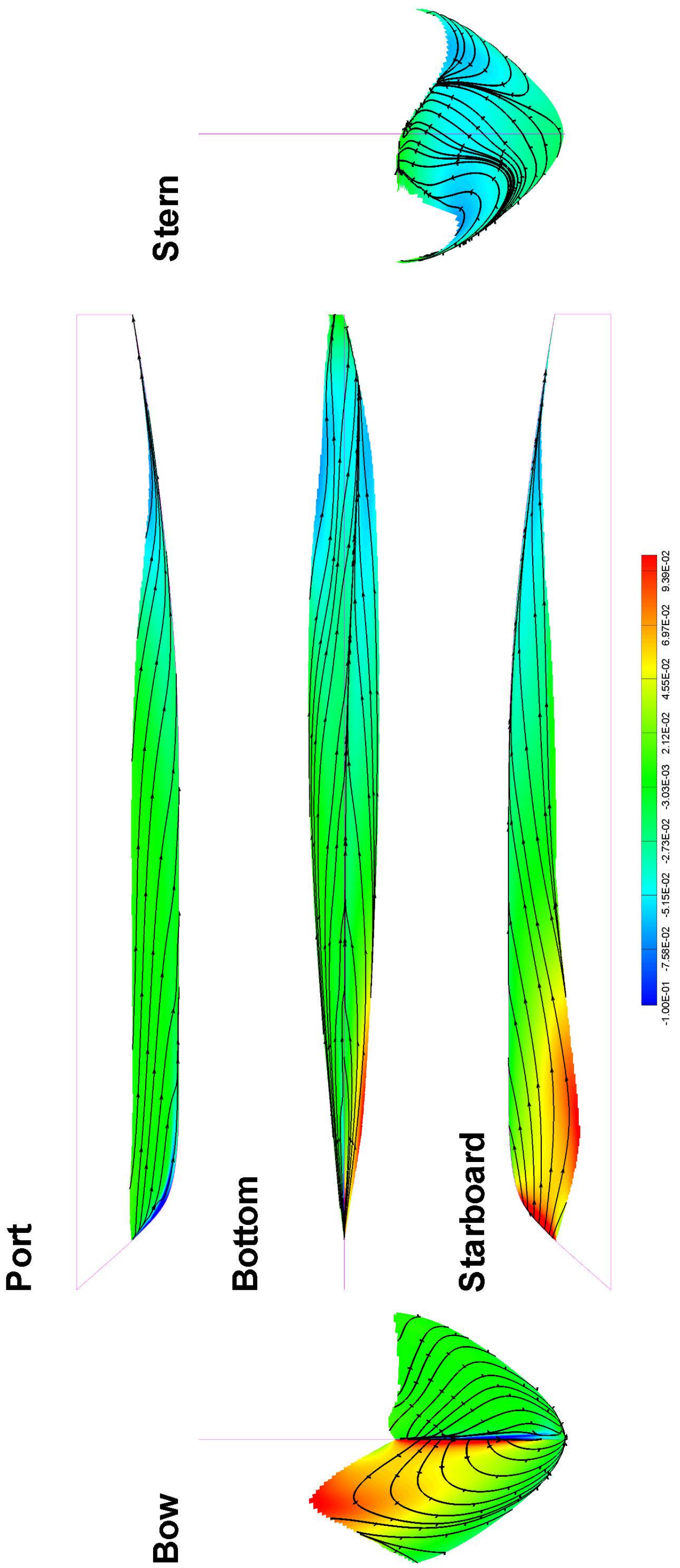

Figure 5.35: Starboard hull pressure contour and surface streamlines below free surface at even keel with $\beta = 6^0$, and $Fr = 0.5$

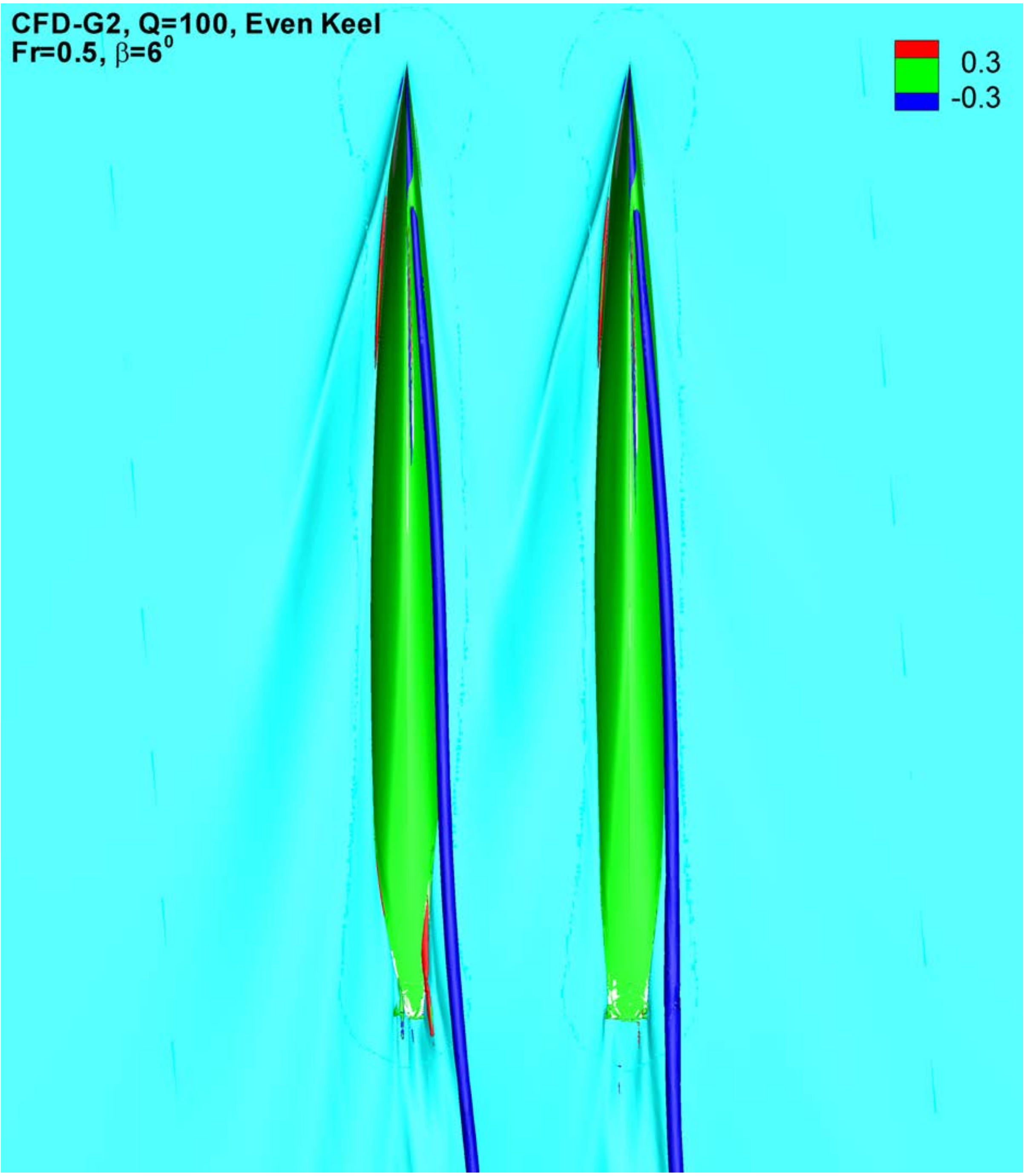

Figure 5.36: Vortex structure for CFD fixed at even keel with $\beta = 6^0$, and $Fr = 0.5$

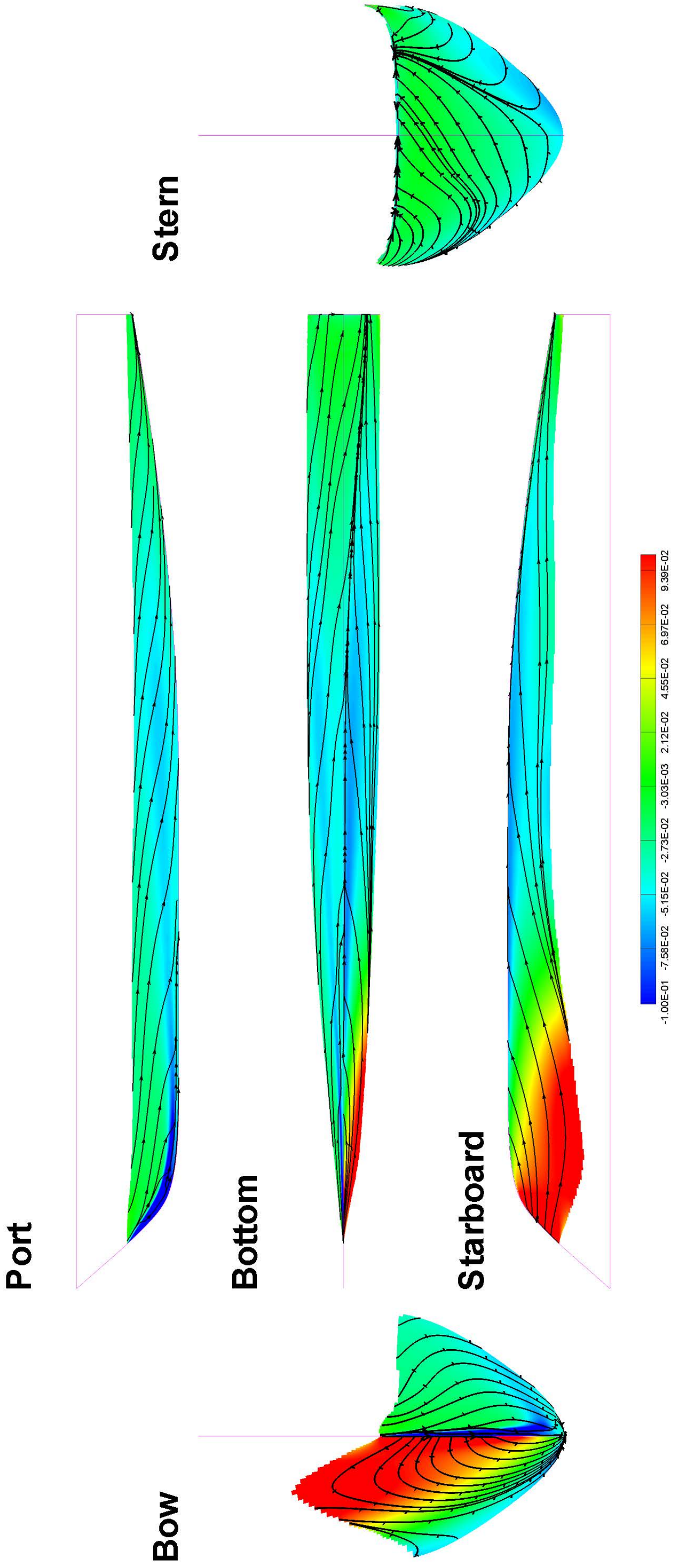

Figure 5.37: Port hull pressure contour and streamlines below free surface at $Fr = 0.4$ and $\beta = 9^0$

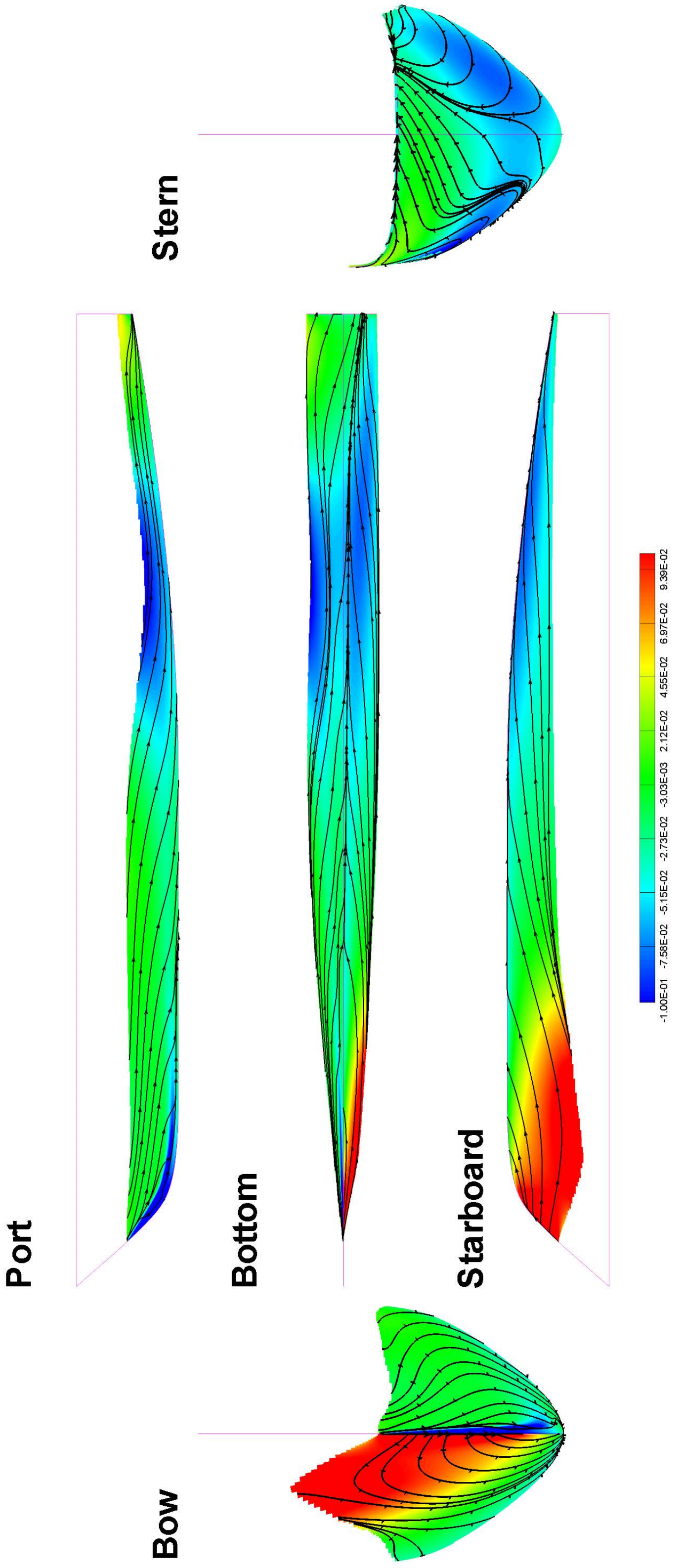

Figure 5.38: Starboard hull pressure contour and streamlines below free surface at $Fr = 0.4$ and $\beta = 9^0$

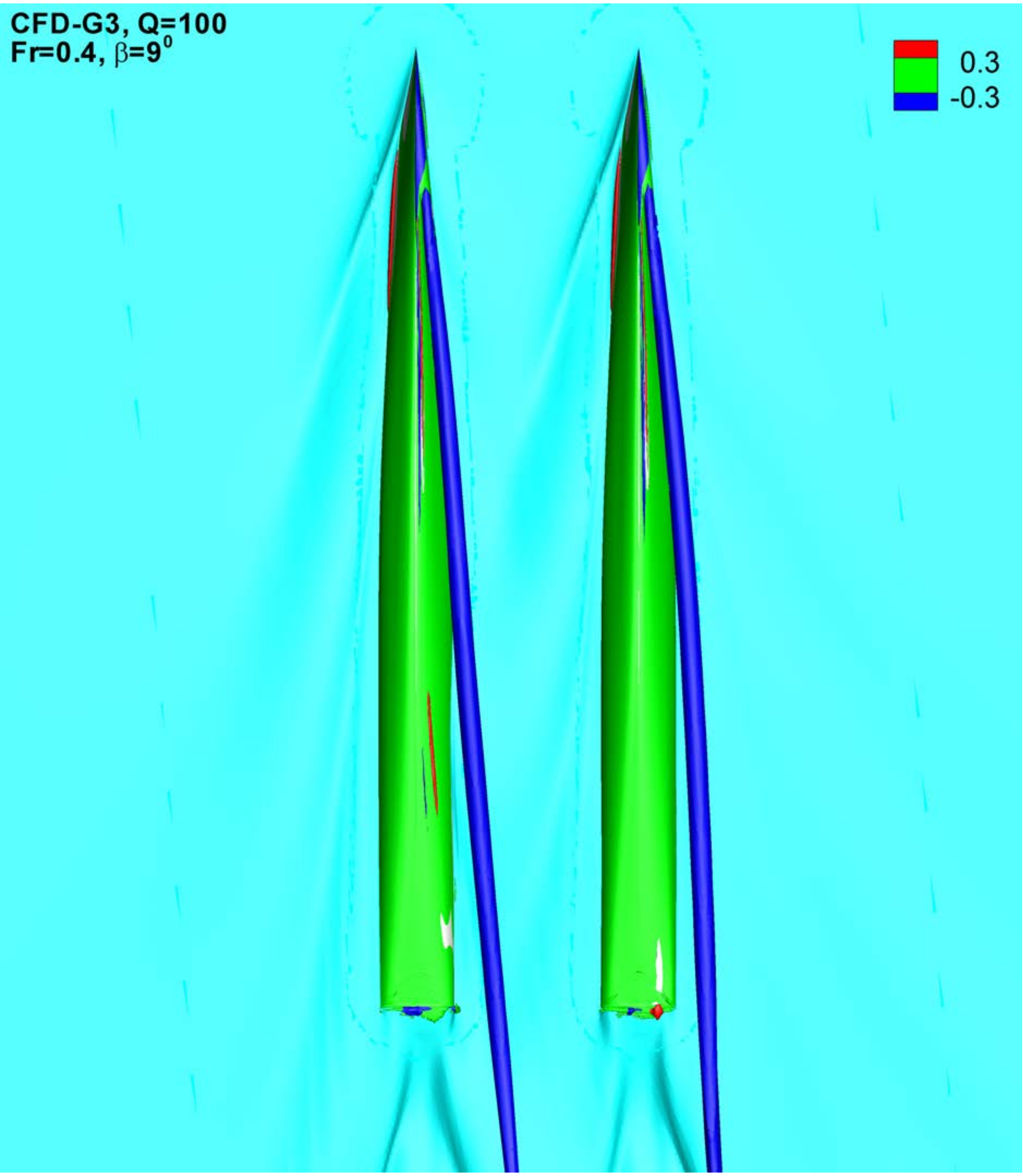

Figure 5.39: Vortex structure for CFD fixed at dynamic sink and trim with $\beta = 9^0$, and $Fr = 0.4$

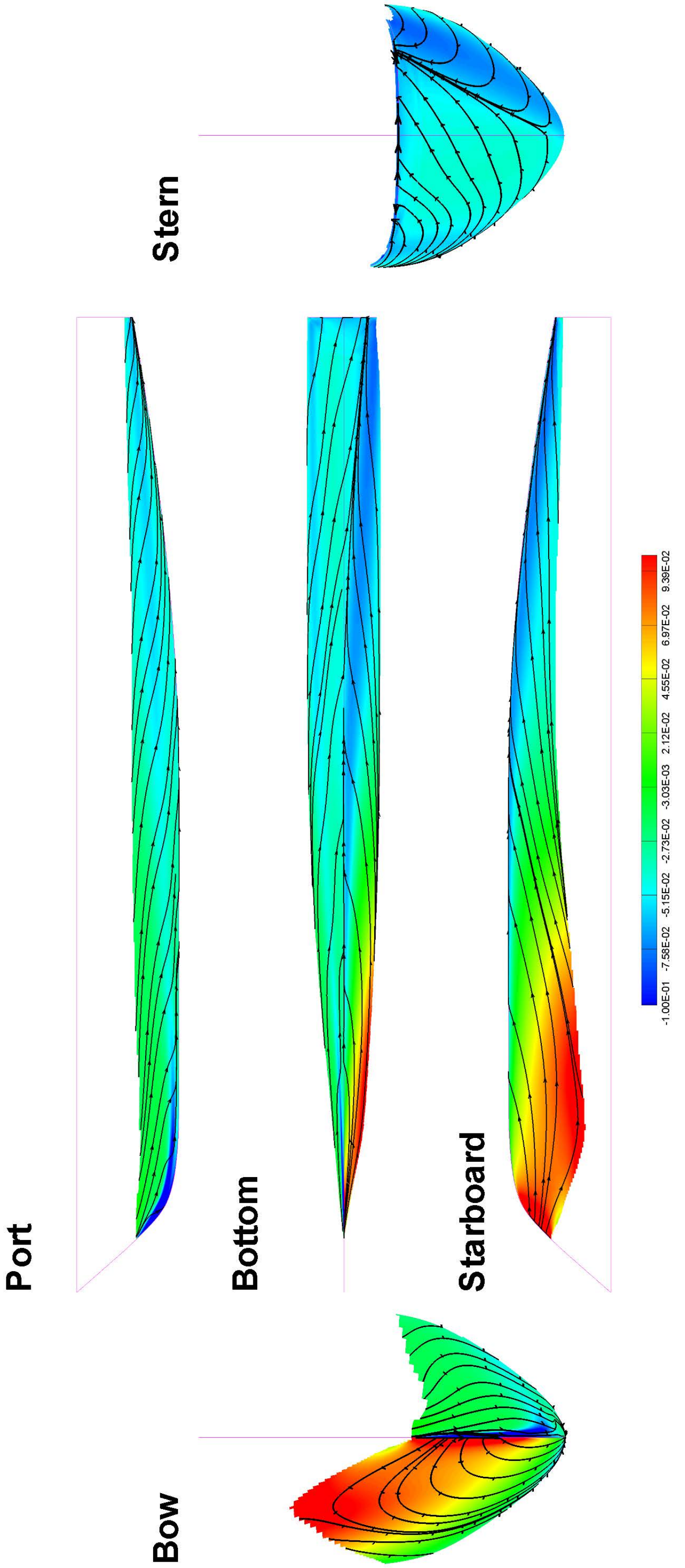

Figure 5.40: Port hull pressure contour and streamlines below free surface at $Fr = 0.5$ and $\beta = 9^0$

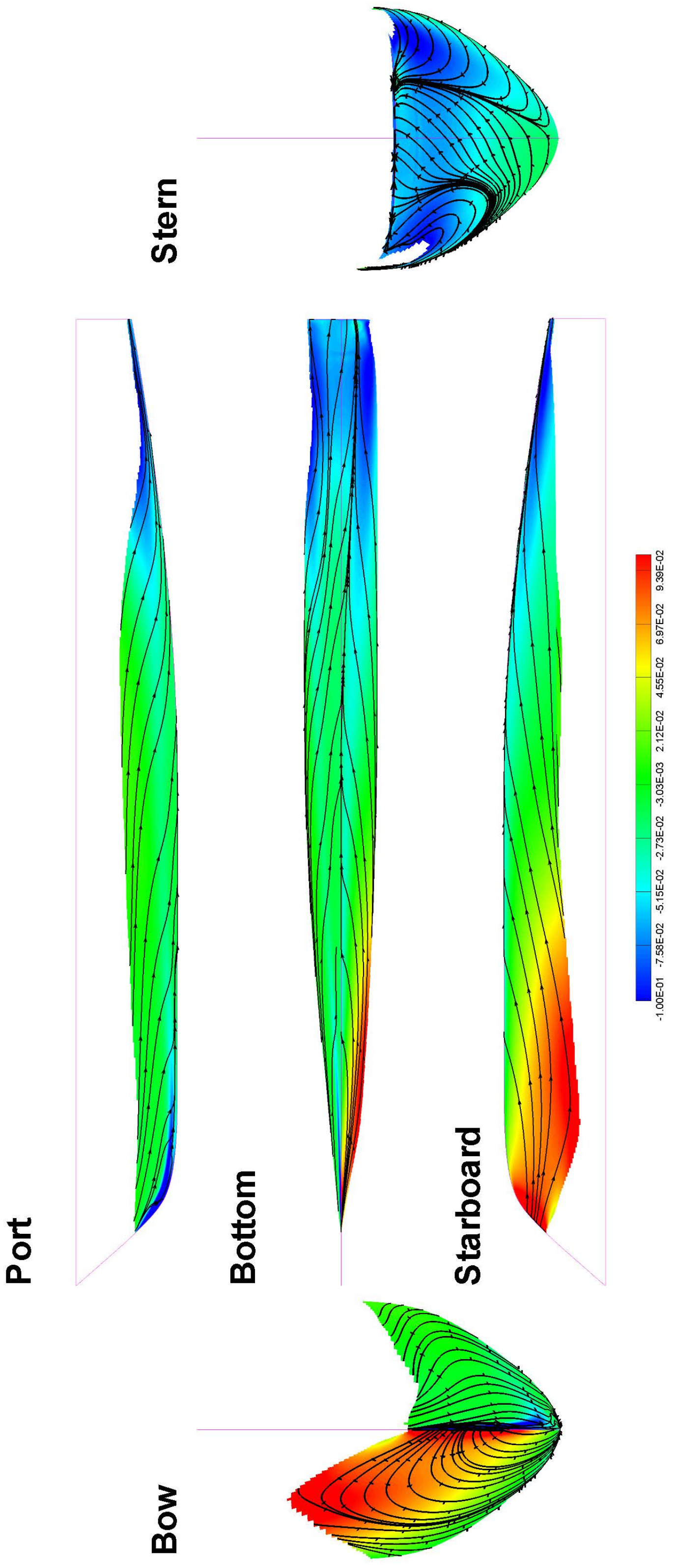

Figure 5.41: Starboard hull pressure contour and streamlines below free surface at $Fr = 0.5$ and $\beta = 9^0$

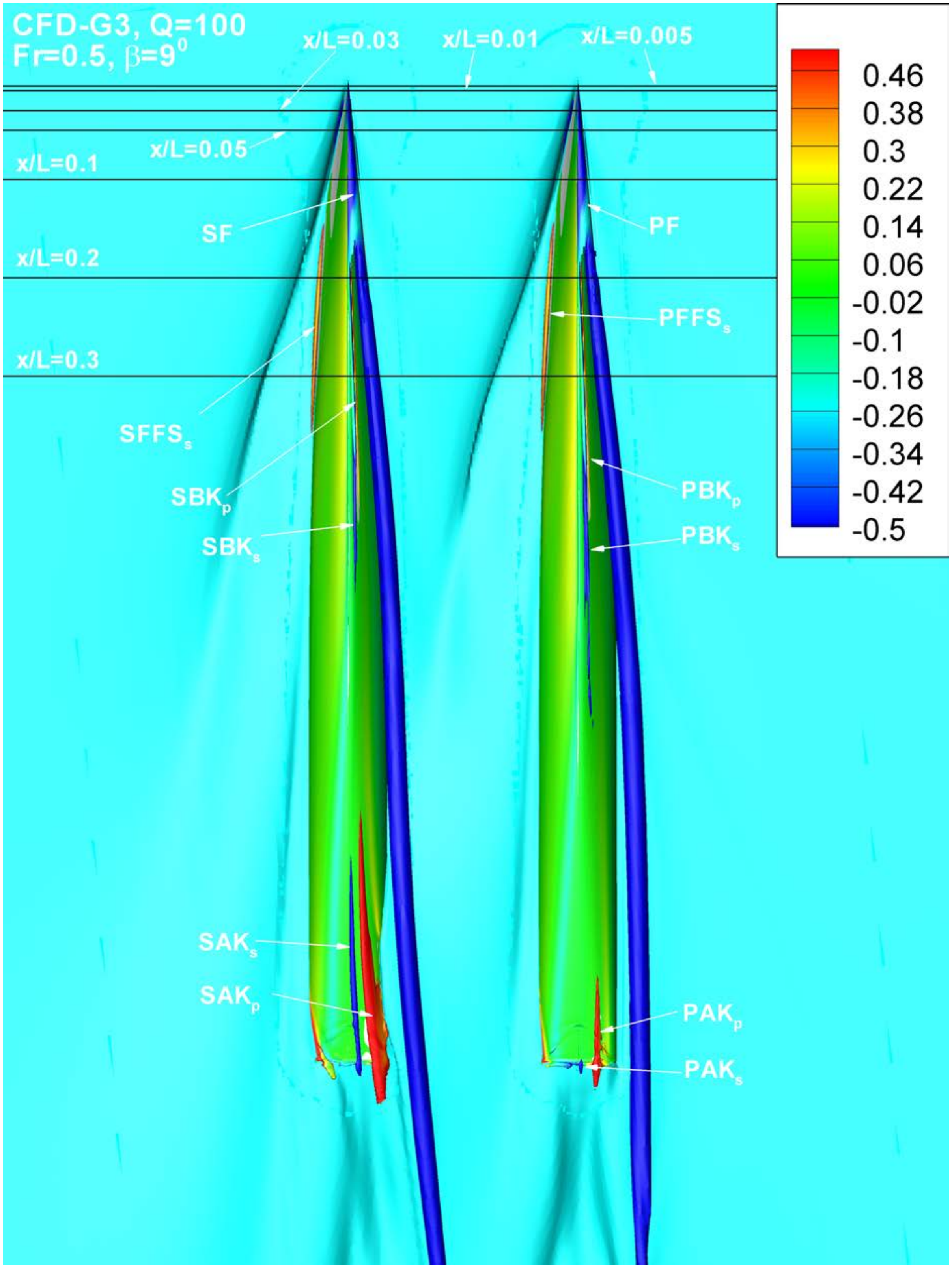

Figure 5.42: Vortex structure for CFD fixed at dynamic sink and trim with $\beta = 9^0$, and $Fr = 0.5$

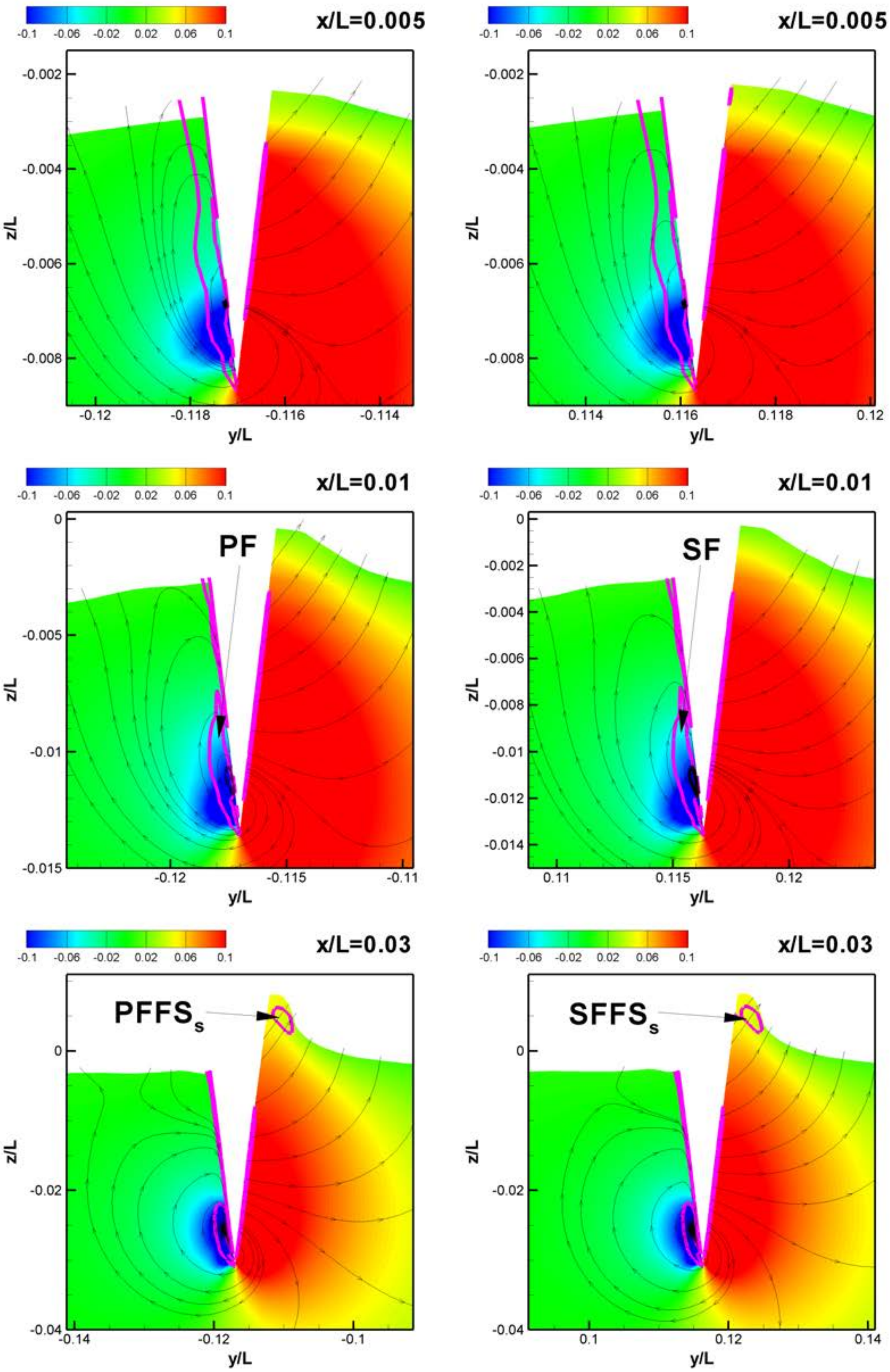

Figure 5.43: Pressure contour, streamlines and $Q = 100$ line (pink colored) at $x/L = 0.005, 0.01, 0.03$ for $Fr = 0.5$, $\beta = 9^0$ (right starboard hull and left port hull)

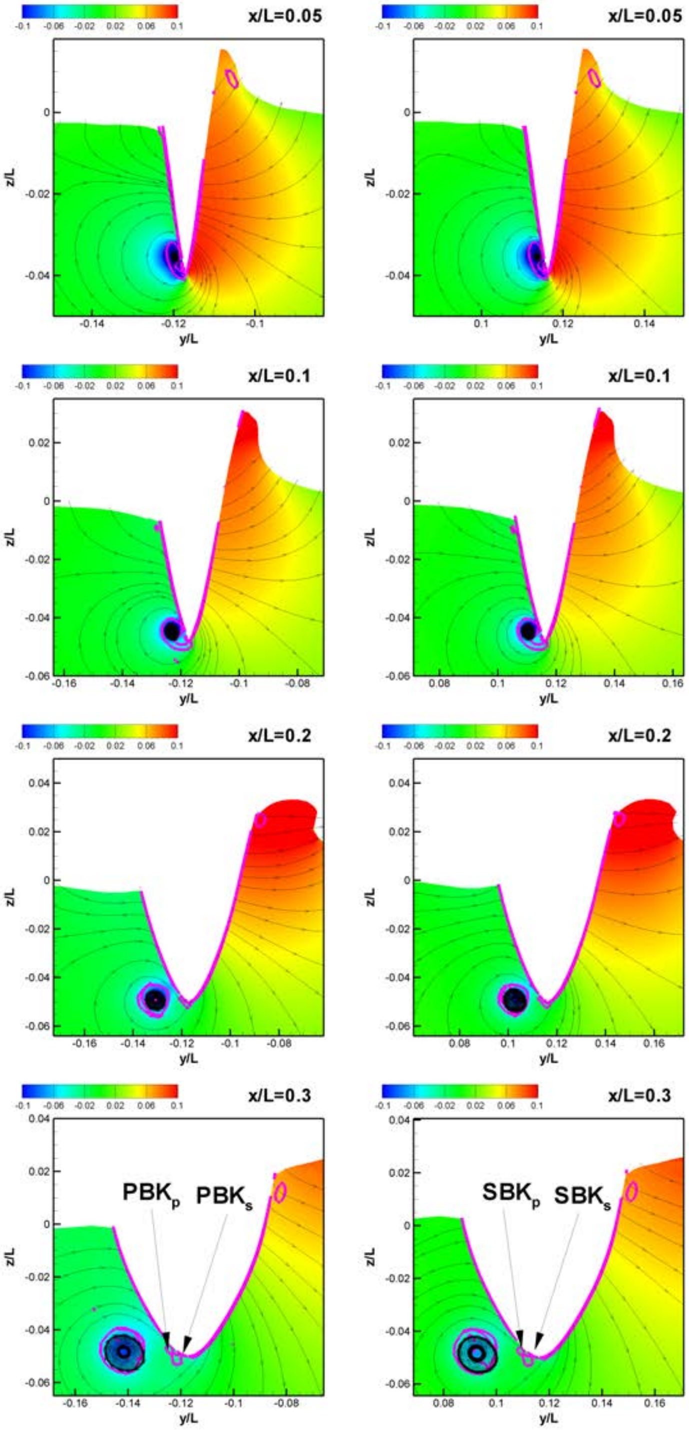

Figure 5.44: Pressure contour, streamlines and $Q = 100$ line (pink colored) at $x/L = 0.05, 0.1, 0.2, 0.3$ for $Fr = 0.5$, $\beta = 9^0$ (right starboard hull and left port hull)

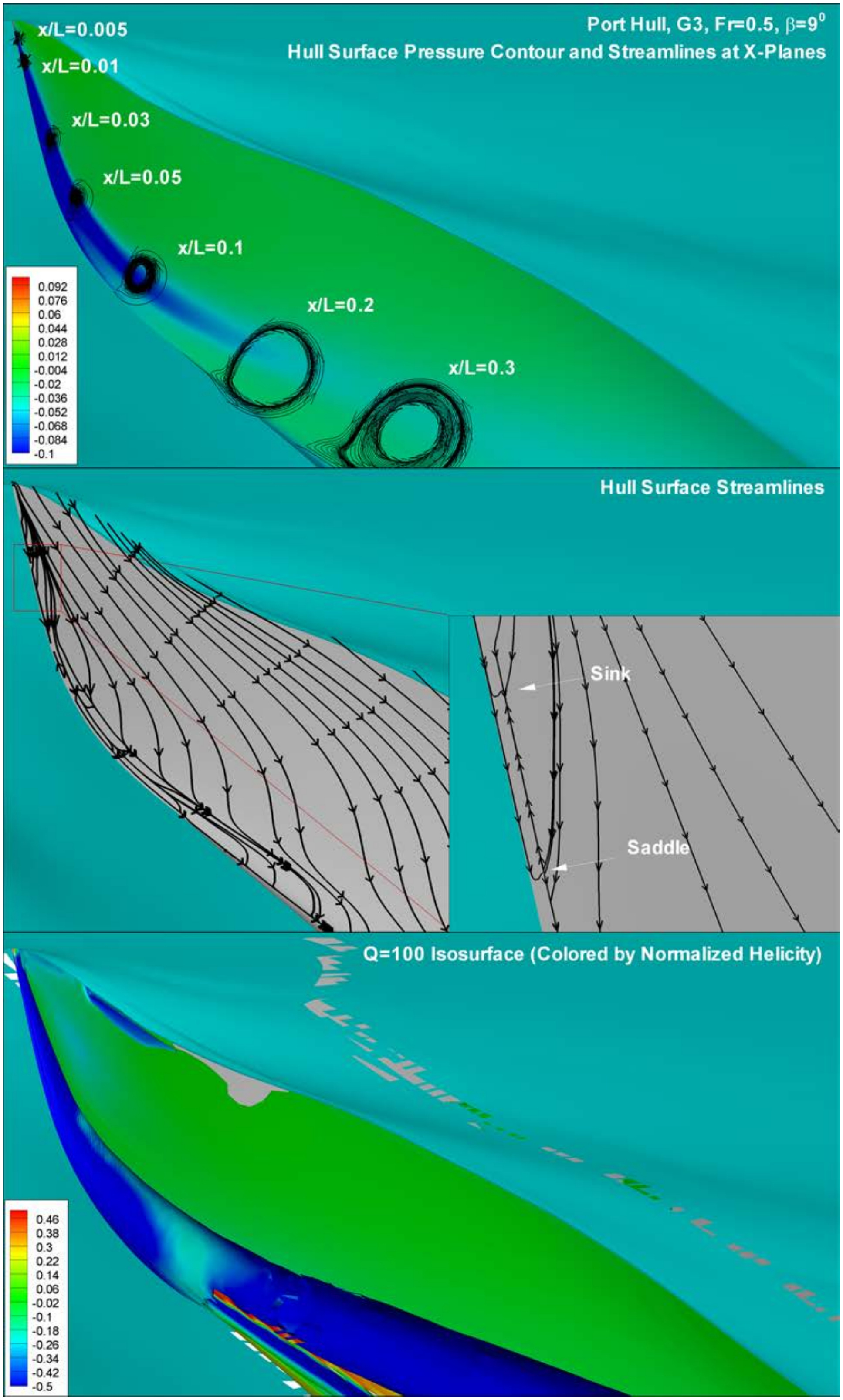

Figure 5.45: Port hull streamlines, $Q = 100$ isosurface, and x-plane streamlines at $Fr = 0.5$, $\beta = 9^0$

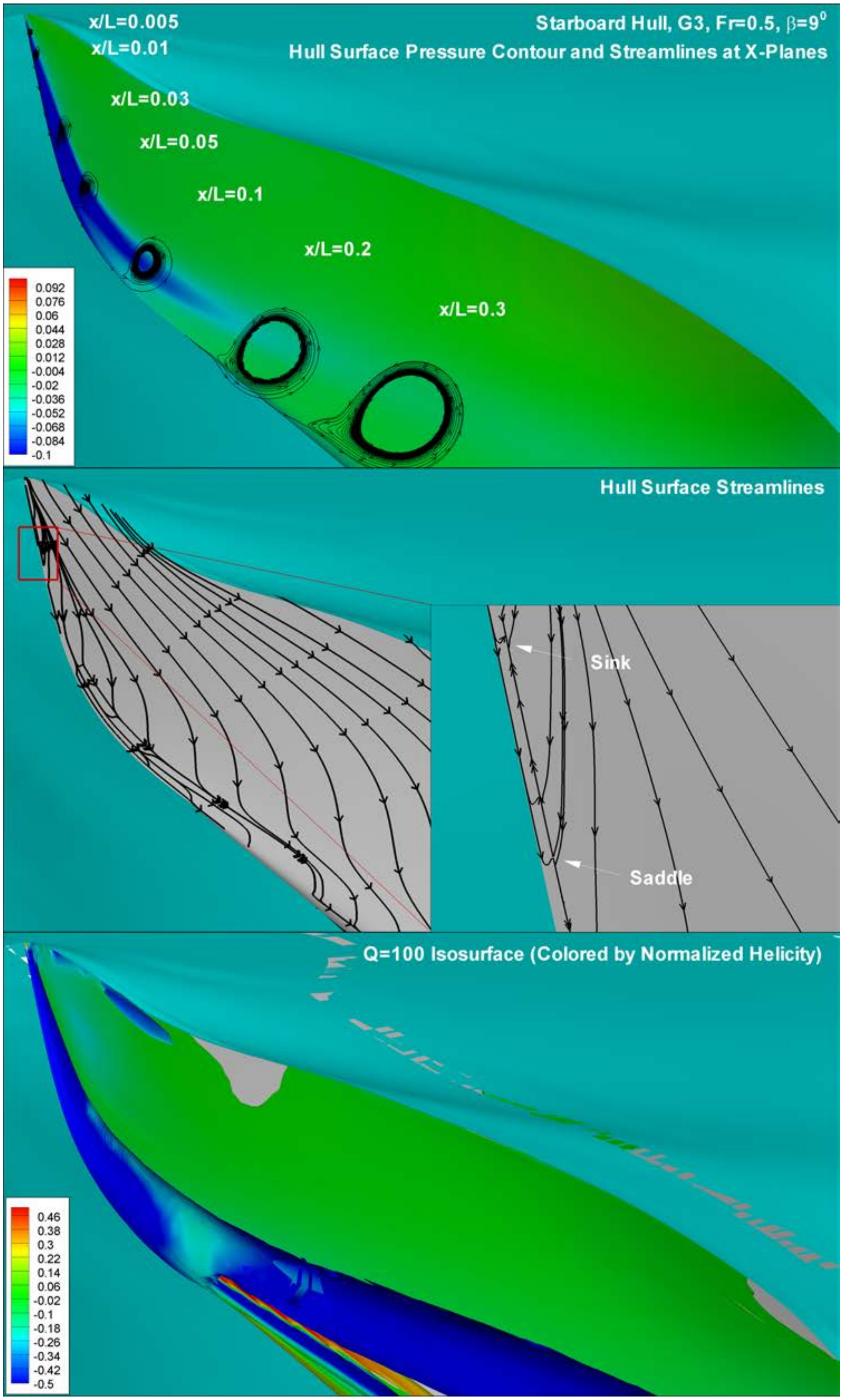

Figure 5.46: Starboard hull streamlines, $Q = 100$ isosurface, and x-plane streamlines at $Fr = 0.5$, $\beta = 9^0$

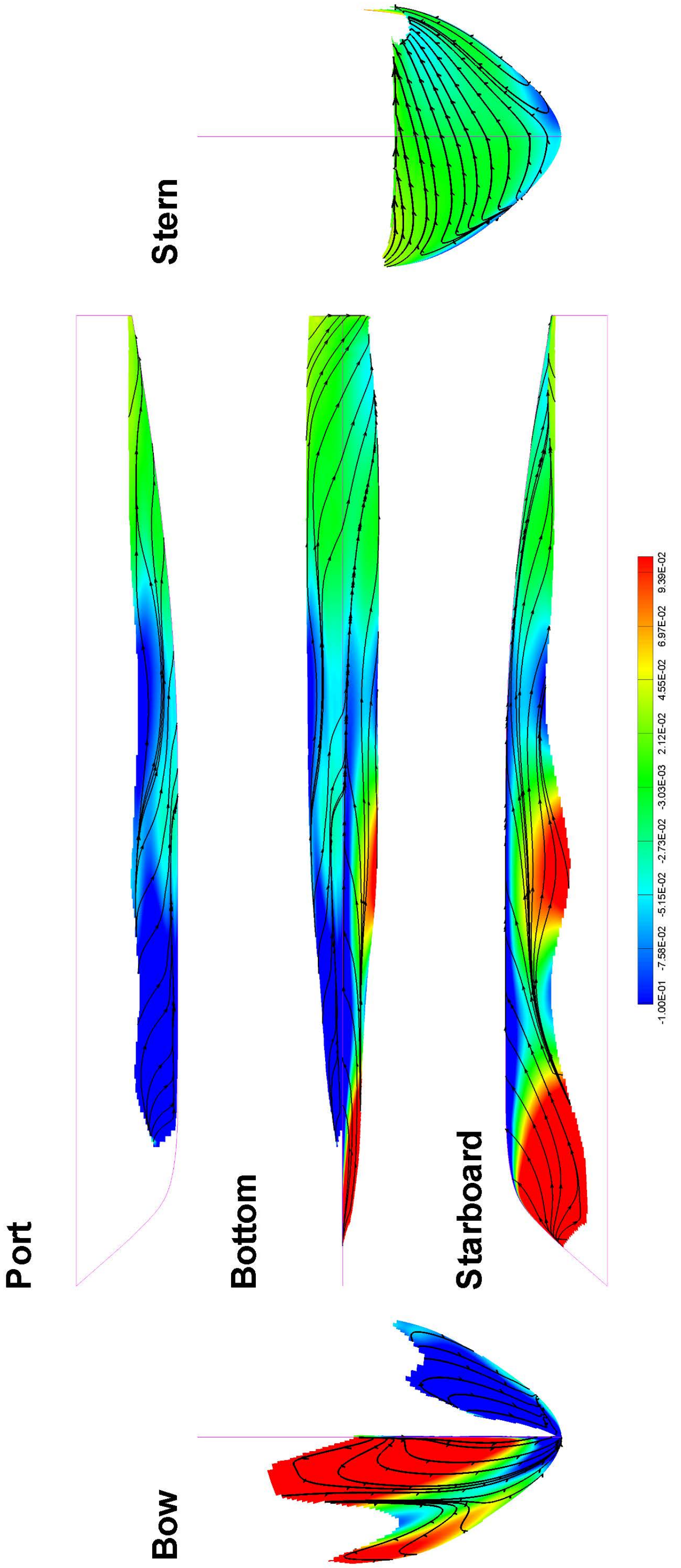

Figure 5.47: Port hull pressure contour and streamlines below free surface at $Fr = 0.3$ and $\beta = 24^0$

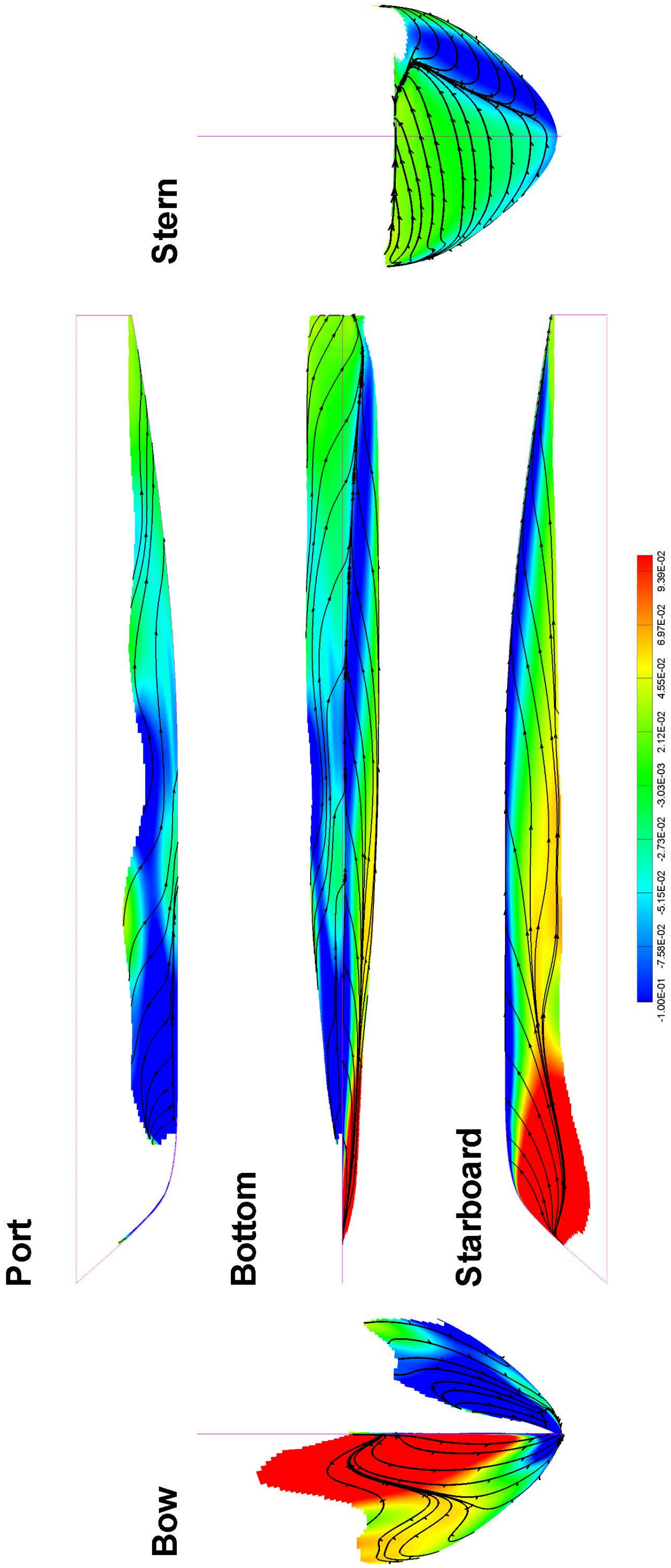

Figure 5.48: Starboard hull pressure contour and streamlines below free surface at $Fr = 0.3$ and $\beta = 24^0$

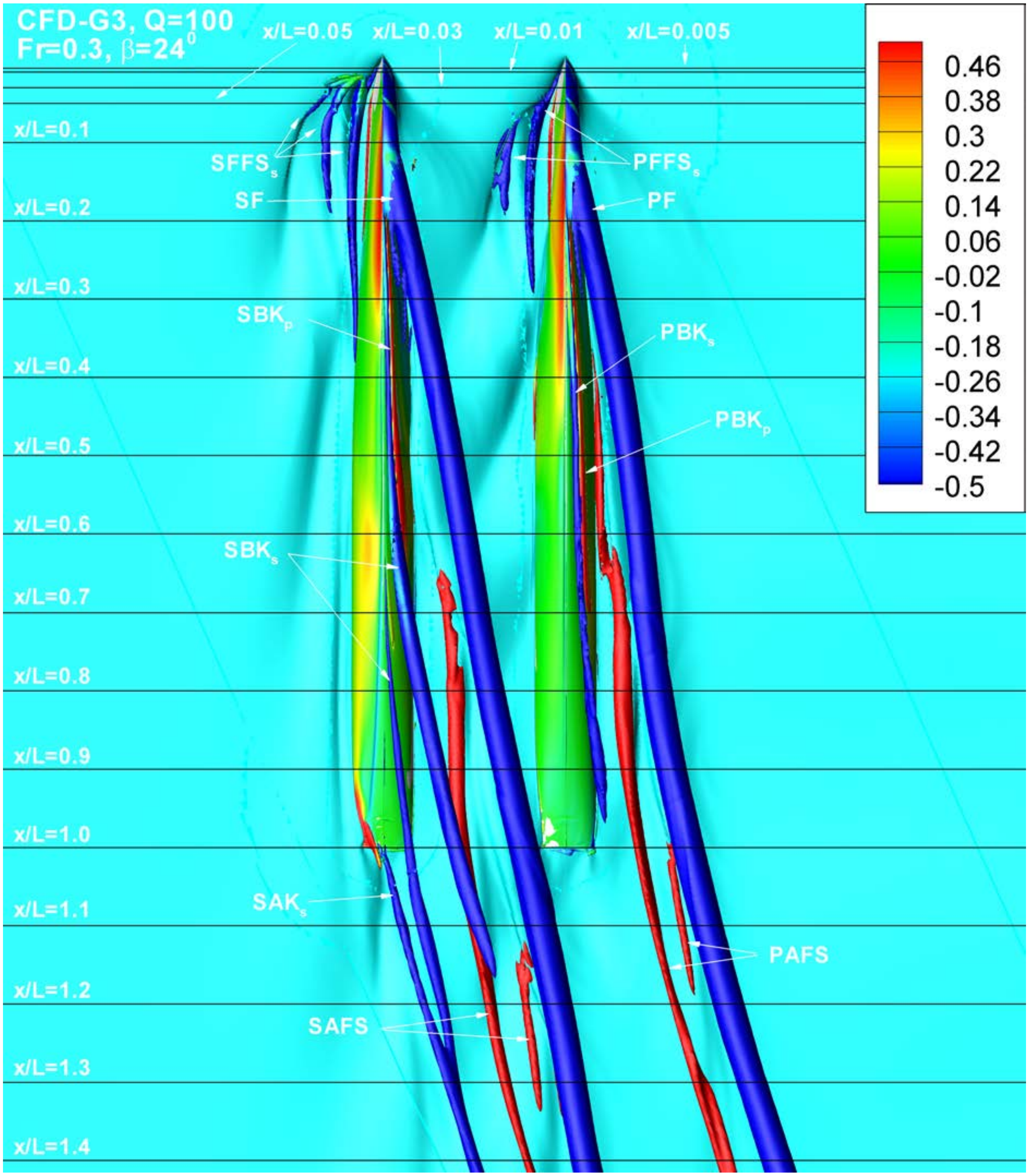

Figure 5.49: Vortical structures for CFD using DES at $\beta = 24^0$, and $Fr = 0.3$

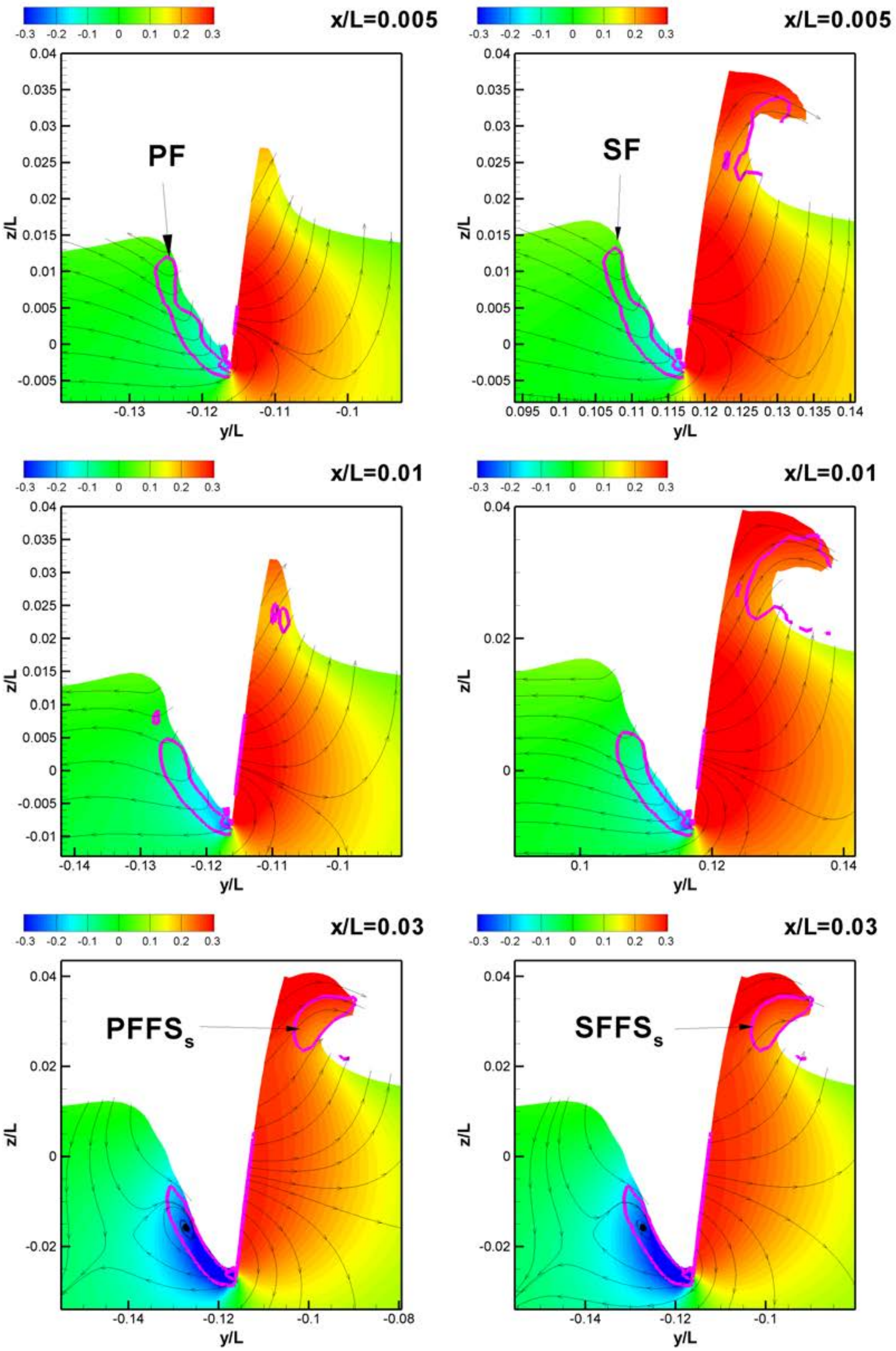

Figure 5.50: Pressure contour, streamlines and $Q = 100$ line (pink colored) at $x/L = 0.005, 0.01, 0.03$ for $Fr = 0.3$, $\beta = 24^0$ (right starboard hull and left port hull)

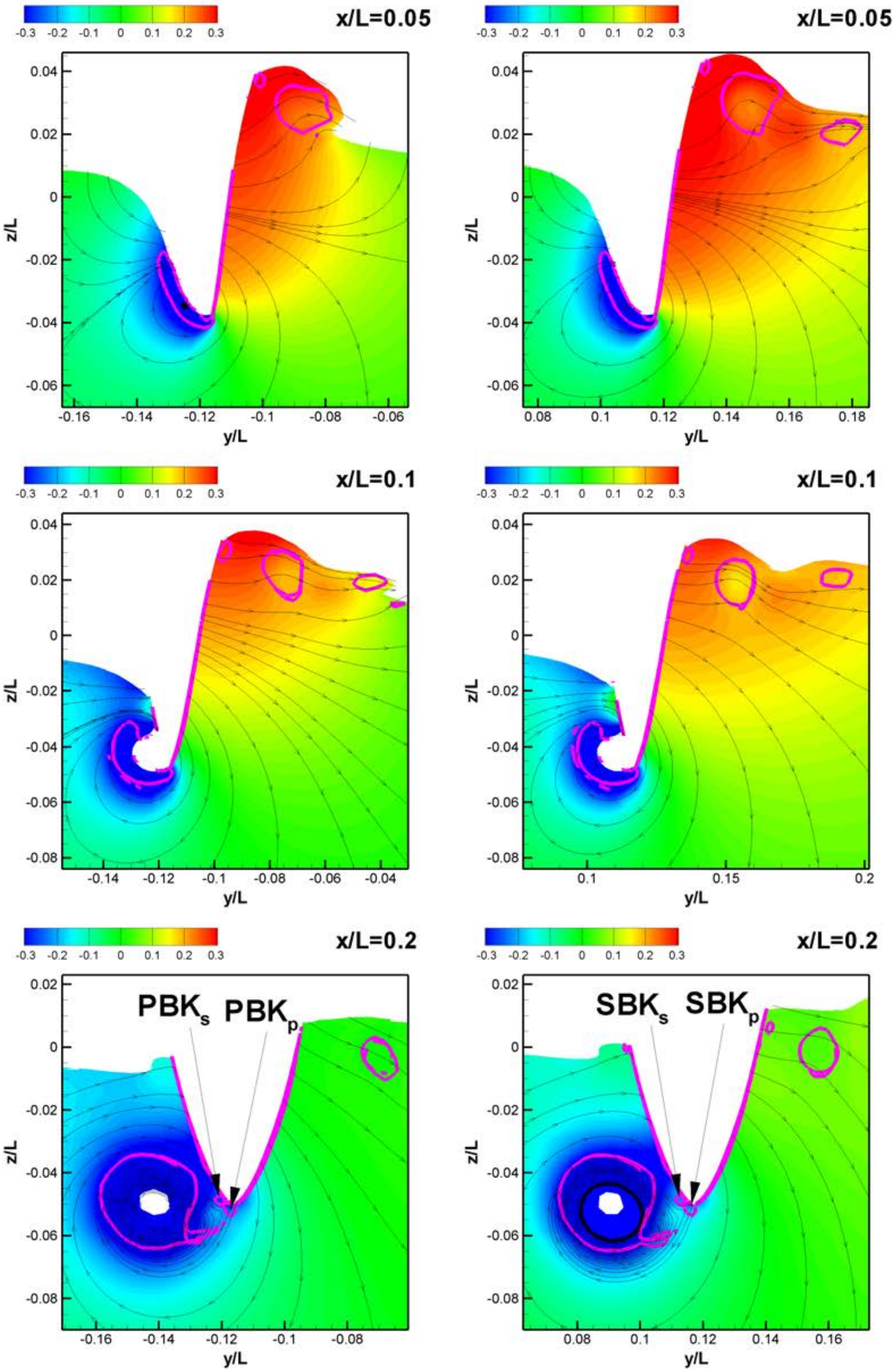

Figure 5.51: Pressure contour, streamlines and $Q = 100$ line (pink colored) at $x/L = 0.05, 0.01, 0.2$ for $Fr = 0.3$, $\beta = 24^0$ (right starboard hull and left port hull)

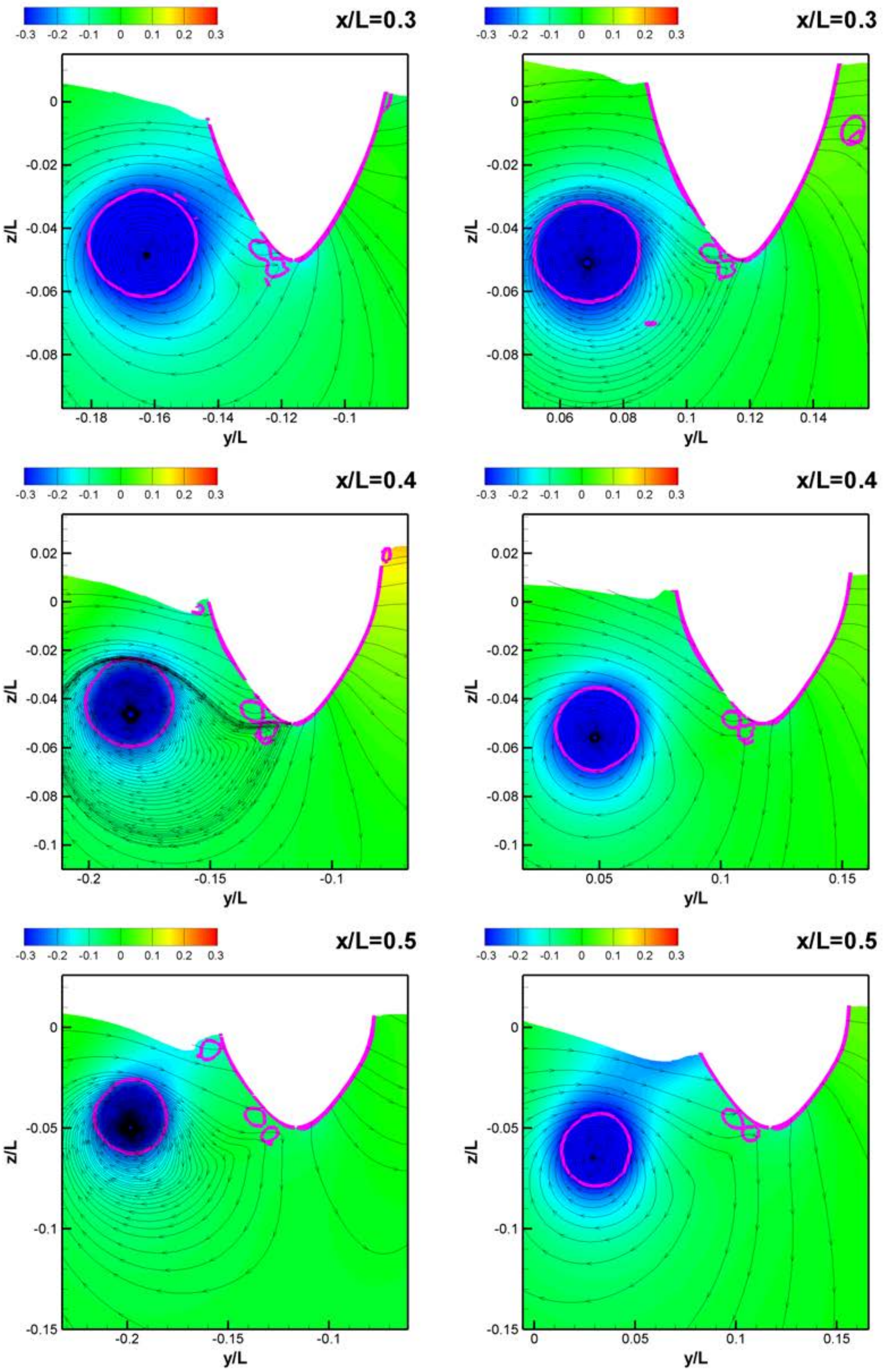

Figure 5.52: Pressure contour, streamlines and $Q = 100$ line (pink colored) at $x/L = 0.3, 0.4, 0.5$ for $Fr = 0.3$, $\beta = 24^0$ (right starboard hull and left port hull)

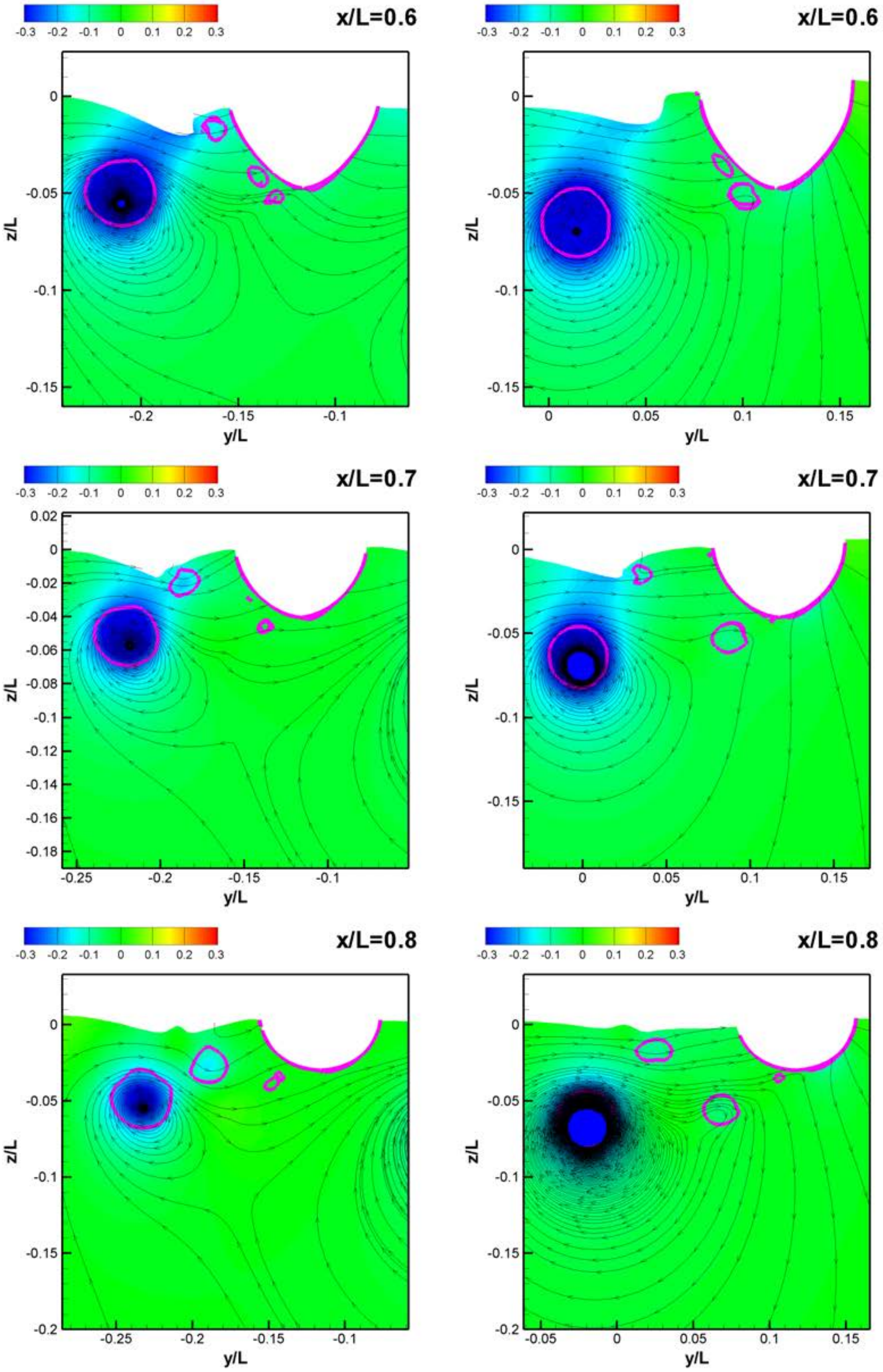

Figure 5.53: Pressure contour, streamlines and $Q = 100$ line (pink colored) at $x/L = 0.6, 0.7, 0.8$ for $Fr = 0.3$, $\beta = 24^0$ (right starboard hull and left port hull)

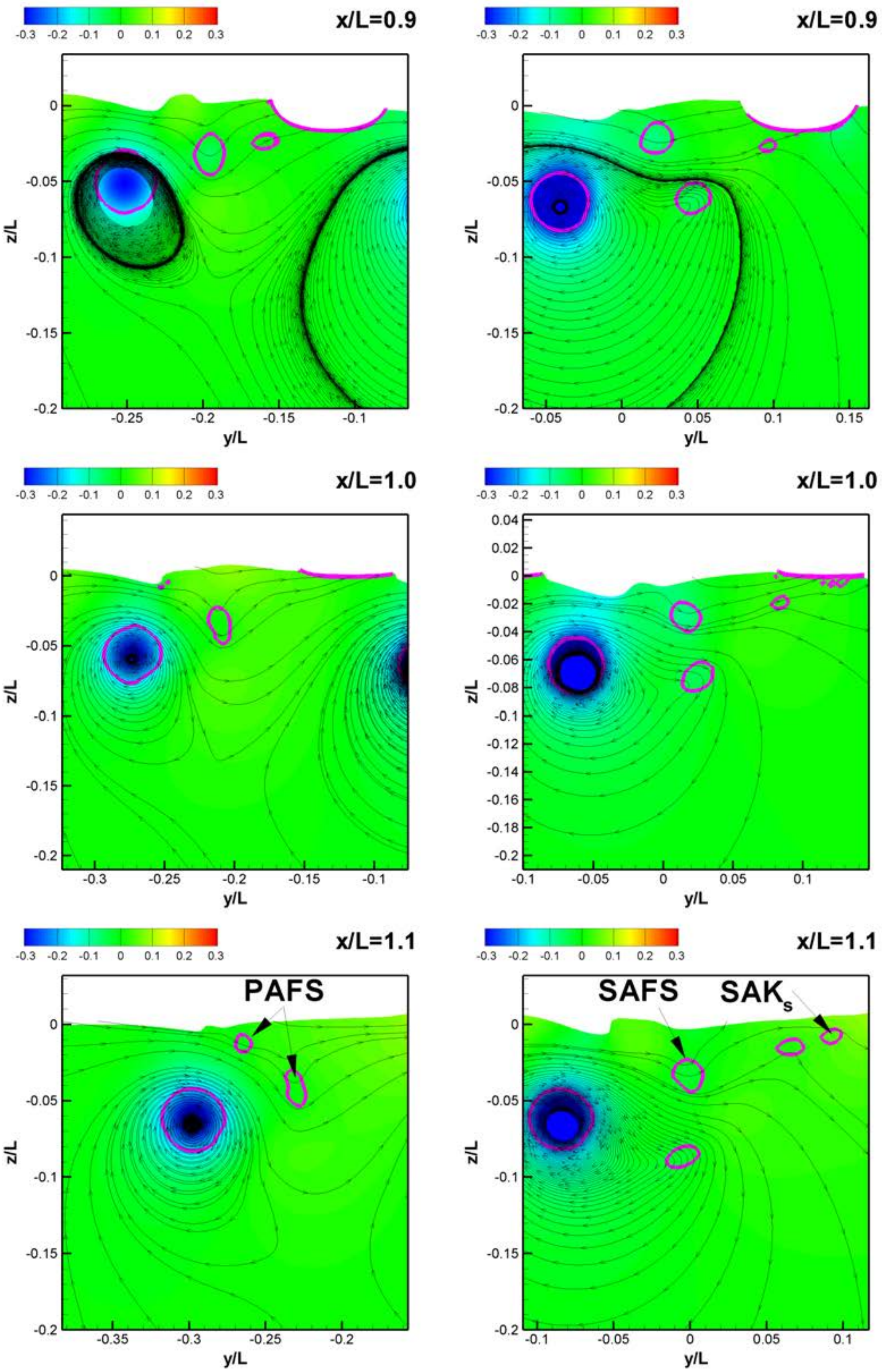

Figure 5.54: Pressure contour, streamlines and $Q = 100$ line (pink colored) at $x/L = 0.9, 1.0, 1.1$ for $Fr = 0.3$, $\beta = 24^0$ (right starboard hull and left port hull)

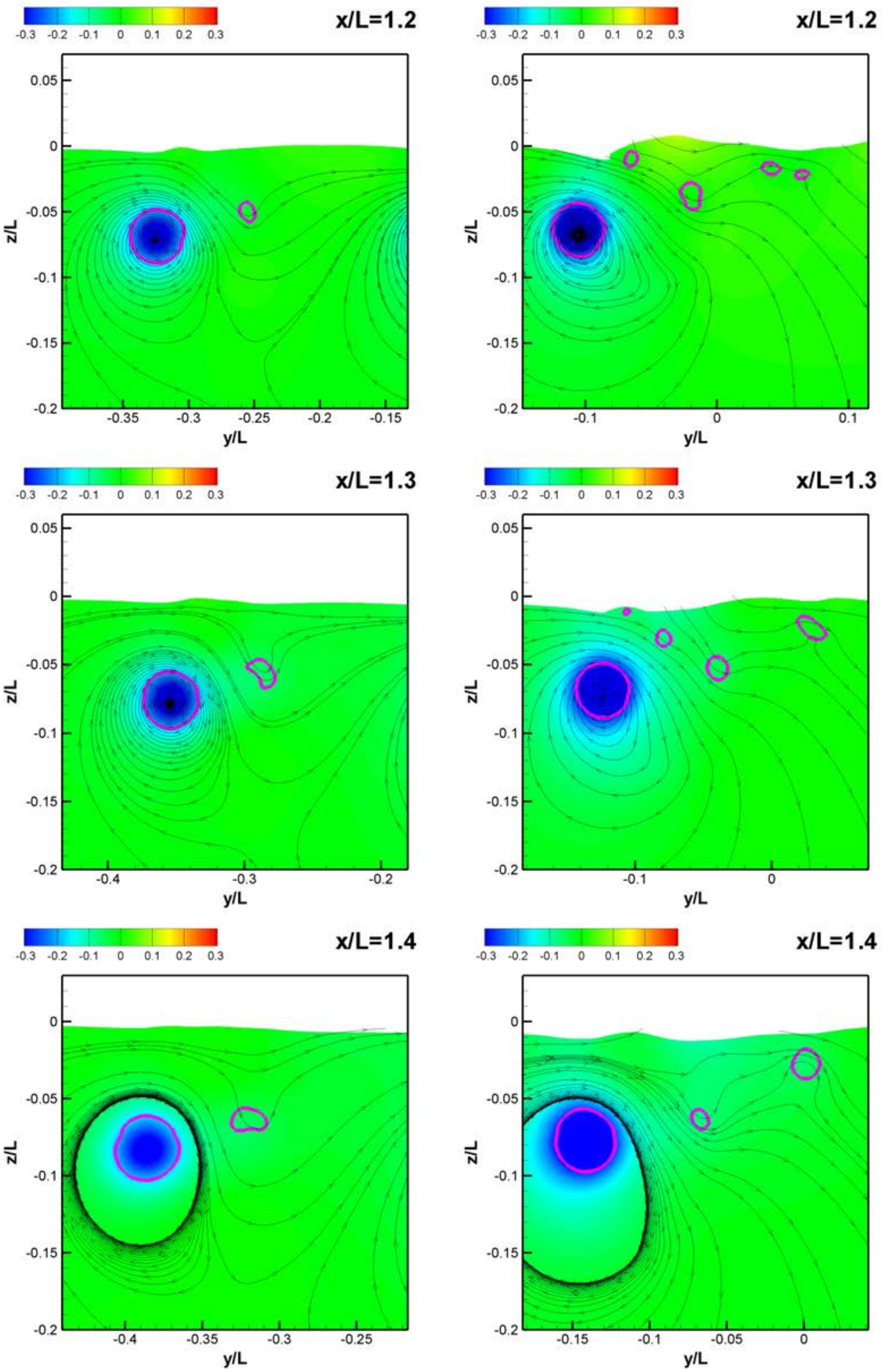

Figure 5.55: Pressure contour, streamlines and $Q = 100$ line (pink colored) at $x/L = 1.2, 1.3, 1.4$ for $Fr = 0.3$, $\beta = 24^0$ (right starboard hull and left port hull)

CHAPTER 6
CONCLUSIONS

Verfication and validation were performed for integral variables for a large range of Fr and β. In general, CFD showed excellent agreement with the EFD results for the integral variables with the exception of motions at large drift angles. Additionally, validation of the local velocity for CFD showed very good agreement with EFD. Large fore-body vortex observed in CFD was validated with the SPIV experiments. This study successfully shows that the new version of CFDShip-IOWA, version 4.5, could be used to reliably predict the integral variables, local velocity, vortex structures and wave patterns for catamaran Delft 372 at static drift and straight ahead conditions. In the future, vortex refinement block will be added to G3 for $Fr = 0.3$ and $\beta = 24^0$ case to improve the wave elevation predictions.

REFERENCES

[1] Z. Zlatev, E. Milanov, V. Chotukova, N. Sakamoto, F., and Stern. Combined model-scale efd-cfd investigation of the manevering characteristics of a high speed catamaran. In *10th International Conference on Fast Sea Transportation FAST 2009*, 2009.

[2] E. Milanov, Z. Zlatev, V. Chotukova, and Stern F. Numerical and experimental prediction of the inherent course stability of high speed catamaran in deep and shallow water. In *28th Symposium on Naval Hydrodynamics*, 2010.

[3] Teresa Castiglione, Frederick Stern, Sergio Bova, and Manivannan Kandasamy. Numerical investigation of the seakeeping behavior of a catamaran advancing in regular head waves. *Ocean Engineering*, 38(16):1806–1822, 11 2011.

[4] R. Broglia, B. Bouscasse, B. Jacob, A. Olivieri, S. Zaghi, and F. Stern. Calm water and seakeeping investigation for a fast catamaran. In *11th International Conference on Fast Sea Transportation, FAST*, 2011.

[5] Wei He, Teresa Castiglione, Mani Kandasamy, and Frederick Stern. Urans simulation of catamaran interference. *Supplemental materials-Report-04112011*, 2011.

[6] M. Falchi S. Grizzi S. Zaghi M. Felli M. Miozzi F. Pereira F. Di Felice F. Stern R. Broglia, G. Aloisio. Measurements of the velocity field around the delft 372 catamaran in steady drift. In *29th Symposium on Naval Hydrodynamics Gothenburg*, 2012.

[7] Shanti Bhushan, Pablo Carrica, Jianming Yang, and Frederick Stern. Scalability studies and large grid computations for surface combatant using cfdship-iowa. *International Journal of High Performance Computing Applications*, 25(4):466–487, November 01 2011.

[8] Tao Xing, Shanti Bhushan, and Frederick Stern. Vortical and turbulent structures for kvlcc2 at drift angle 0, 12, and 30 degrees. *Ocean Engineering*, 55(0):23–43, 12/1 2012.

[9] R. Vant Veer. Experimental results of motions and structural loads on the 372 catamran model in head and oblique waves. Technical Report N.1130, TU Delft, 1998.

[10] P. M. Carrica. An unsteady singlephase level set method for viscous free surface flows. *International Journal for Numerical Methods in Fluids*, 53(2):229, 2007.

[11] P. M. Carrica. Ship motions using single-phase level set with dynamic overset grids. *Computers fluids*, 36(9):1415, 2007.

[12] S. Wallin. An explicit algebraic reynolds stress model for incompressible and compressible turbulent flows. *Journal of Fluid Mechanics*, 403(1):89, 2000.

[13] Florian R. Menter. Two-equation eddy-viscosity turbulence models for engineering applications. *AIAA Journal*, 32(8):1598–1605, 1994.

[14] A. Travin, M. Shur, Mm Strelets, and PR Spalart. *Physical and numerical upgrades in the detached-eddy simulation of complex turbulent flows*, pages 239–254. Advances in LES of complex flows. Springer, 2004.

[15] D. Degani, A. Seginer, and Y. Levy. Graphical visualization of vortical flows by means of helicity. *AIAA Journal*, 28(8):1347–1352, 1990.